

Acta Universitatis
Lappeenrantaensis
832



Pavel Geydt

**ATOMIC FORCE MICROSCOPY OF ELECTRICAL,
MECHANICAL AND PIEZO PROPERTIES OF
NANOWIRES**



Pavel Geydt

ATOMIC FORCE MICROSCOPY OF ELECTRICAL, MECHANICAL AND PIEZO PROPERTIES OF NANOWIRES

Thesis for the degree of Doctor of Science (Technology) to be presented with due permission for public examination and criticism in the Auditorium of the Student Union House at Lappeenranta University of Technology, Lappeenranta, Finland on the 7th of December, 2018, at noon.

Acta Universitatis
Lappeenrantaensis 832

- Supervisors Professor Erkki Lähderanta
LUT School of Engineering Science
Lappeenranta University of Technology
Finland
- Dr. Prokhor Alekseev
Laboratory of Surface Optics
Ioffe Institute
Russia
- Reviewers Professor Anna Fontcuberta i Morral
Laboratory of Semiconductor Materials
Ecole Polytechnique Fédérale de Lausanne
Switzerland
- Dr. Maria Tchernycheva
Center of Nanosciences and Nanotechnologies
Université Paris-Sud
France
- Opponent Dr. Teemu Hakkarainen
Optoelectronics Research Centre
Tampere University of Technology
Finland
- Custos Professor Erkki Lähderanta
LUT School of Engineering Science
Lappeenranta University of Technology
Finland

ISBN 978-952-335-310-7

ISBN 978-952-335-311-4 (PDF)

ISSN-L 1456-4491

ISSN 1456-4491

Lappeenrannan teknillinen yliopisto

LUT Yliopistopaino 2018

Abstract

Pavel Geydt

Atomic Force Microscopy of electrical, mechanical and piezo properties of nanowires

Lappeenranta, 2018

104 pages

Acta Universitatis Lappeenrantaensis 832

Diss. Lappeenranta University of Technology

ISBN 978-952-335-310-7, ISBN 978-952-335-311-4 (PDF), ISSN-L 1456-4491, ISSN 1456-4491

Careful methodology of Atomic Force Microscopy (AFM) regimes was developed for advanced examination of electrical transport, mechanical strength and electro-mechanical (piezoelectric) features of as-grown III-V semiconductor quasi-one-dimensional nanostructures. The thesis is based on the experimental work with the standard commercial measuring station. The general idea was to focus on the protocol of data acquisition and interpretation in order to obtain characteristics of elaborated structures and materials. We demonstrated the feasibility to implement various experiments on a regular station without visualization of a direct contact established between the microscope probe and the measured nanowires (NWs). The novelty of this work is in the utilization of solely AFM device for advanced studies of the NWs in direct contact achieved with the modern PeakForce-based QNM™, KPFM and TUNA™ regimes.

Semiconductor NWs receive an increasing attention of the research community because they are promised to become indispensable building blocks of many modern electronic and mechanical devices. Atomic force microscopy is a highly versatile technique, which was effectively used for studies of many classes of nanostructures developed during the last three decades. At the same time, no adequate summary of the capabilities and prospects of AFM instrument for investigation of NWs was made. An attempt to formulate such a summary is shown in the present thesis and in the list of related publications.

Peculiarities of electrical measurements of NWs with a small sized conductive probe were formulated in the study of passivated GaAs NWs, where different charge transport mechanism and surface-induced phenomena were considered. Focus on real conical (tapered) shape of wurtzite InP NWs was done permitting to find the Young's modulus of wurtzite phase InP. Combining the advantageous material (GaAs), crystal composition (wurtzite), sized structure (NW) and method of study (conductive AFM) demonstrated the way to use GaAs NWs for combined piezo-phototronic electrical energy generators.

Keywords: atomic force microscopy, nanowire, PeakForce, I-V curve, flexibility profile, Young's modulus, piezoelectricity, piezo-phototronic effect, wurtzite, GaAs, InP

Acknowledgements

“Not only the Universe is stranger than we think, it is stranger than we can think.”
W. Heisenberg

This original work was performed in Lappeenranta University of Technology (LUT), with very active assistance from Ioffe Institute and samples support from Aalto University.

Foremost, I wish to express my gratitude to the supervisor Erkki Lähderanta for establishment of my position and more nuanced things such as trust and delegation of responsibility, which allowed me to grow as a researcher and a self-sufficient specialist. The brilliant atmosphere of cross-border cooperation with best Russian experts in physics provided me with opportunity to learn physics from outstanding scholars. Due to this environment in our lab, I recognized many fields of scientific practice and formulated my knowledge into a systematized education. Apart from the abovementioned, I am thankful to Erkki due to support of internships, organized by DATIS project and directing me to attendance in my first international conferences in physics, because these events shaped my professional interests and kept my mind open.

My deepest appreciation is to the group of late Aleksander Titkov[†] in Physical-Technical Institute (Ioffe Institute) in St. Petersburg, Russia. Firstly, to Prokhor Alekseev who very personally mentored all sides of my research in nanowires and AFM during all the Doctoral years. Moreover, he brought my research attention close to the applicable thinking about innovative technologies like piezo-phototronics. Secondly, to Mikhail Dunaevskiy who benefited me with brilliant clear explanations of non-trivial stuff related with mechanical and electronic effects in materials and enlightened me in the details of mechanical properties of solid matter. Both of these people supervised my work and were my closest peers, caring debaters and attentive co-authors. Finally, I learnt the foremost of details of SPM techniques thankfully to them during my preceding Master's period.

I am grateful to colleagues in Aalto University, Espoo, Finland – the group of Harri Lipsanen: Tuomas, Joonas-Pekko and Vladislav – for guiding me through real nano-scale fabrication, help in revision of the present thesis and for creation of almost all samples analyzed in this Doctoral book. Here I also would like to acknowledge Ilya Soshnikov with his colleagues and the lab of George Cirilin (Academic University, St. Petersburg, Russia) for fabrication of the samples for demonstration of piezoelectric phenomena, which I believe can catalyze big changes in wearable electronics.

I acknowledge the generous funding from LUT Doctoral School and Finnish Cultural Foundation, who supported writing of this dissertation and EU Commission with Moscow State University for visits to major conferences. I was so lucky to get paid for curiosity and ambitions to change the world through the novel research ideas! My mentors and grantors convinced me that prosperity of people is the true reason to make science.

Kiitos paljon to few people from LUT for a sense of great actions done here: Toni Väkiparta for enthusiastic support with SEM and our valuable discussions related with microscopy, Sari Damsten who cares about all the doctoral students including me, Anu Honkanen who brings in good HR practices to multicultural personnel, Heikki Haario for many years and arrangements for development of the old MaFy and Jari Hämäläinen for refreshing the attitude toward research, arranging interesting seminars and taking real care about wellbeing at work in our Faculty. Separate thanks to Kaj Backfolk and his team Katriina and Sami who became my colleagues and guides to industrial chemistry related with cellulose and paper materials. My thanks also goes to my closest lab colleagues Aleksander, Ivan, Ekaterina, Anton, Egor, Kristina and Bernardo for plenty of communication related and not related with work during the years of my doctoral study.

I would like to gratitude professors Boris Aronson, Aleksander Granovsky, Andrey Shelankov, Mikhail Shakhov, Igor Rozhansky, Nikita Averkiev, Nikolay Poklonski, Aleksander Okotrub and Lyubov Bulusheva for many long discussions about physics and life during these years. My compliments to Aleksandra Elbokyan for devoutful and crazy support of science, without whom neither this thesis nor zillions of other research papers would appear.

My friends made my professional mood operative and accelerated this research. Personal thanks to my best friends Sasha, Mitya and Egor. I'm grateful to comrades from Gorynin Art Metal Studio: Aleksander & Katya, Sergey and Mitya; to Golyanovo folks; to my dearest people: Masha, Ksenia, Yuri & Svetlana, Roma, Ayshat, Diana, Valentin, Grigoriy; plus Pavel and Evgeniya from LUT – for plenty of reasons left undeclared here.

I feel inexpressibly thankful to late Tatiana Makarova[†] for being a great friend and colleague. She provided me the wings for scientific research and insightful teaching, directed me to encouraging internships in UNSW Sydney and UniNOVA Lisbon with world-level research projects, exceptional people and experiences. Tatiana's personal charisma and her family members (Anna and three little blondes) have affected my views on life learning and travel, doing active sports and enjoying my scientific addiction. A person who enchanted me and the only one who believed in me even more than I did, a true soulmate that I miss very much.

I am thankful to Alina for many efforts on raising our children, introducing me to actual theater & circus and for earlier joyful moments. I also highly appreciate practical help from Dmitry and some earlier activity from Elena. My kids are, well, the best what I have in my life. Thanks to my dear sons Neil and Philipp for many-many smiles and pure delight of their existence that makes me a happier father. At last, the very special Thanks is to my adorable daughter Alisa for making me happy and being felt loved.

Алисе, Филиппу и Нилу

Contents

Abstract

Acknowledgements

Contents

List of publications	11
Abbreviations, terms and symbols	13
1. General introduction	15
2. Basic concepts	19
2.1 Semiconductors surfaces, defects and depletion layer.....	19
2.2 Nanowires: classification, size effects and nanomanipulation	21
2.3 Fabrication of nanowires	22
2.4 Crystal structure of semiconductor nanowires.....	23
2.5 Mechanical properties of materials in nanowires	25
2.6 Scanning Probe Microscopy: major regimes of operation.....	26
2.7 PeakForce mode: TUNA and QNM advanced regimes of AFM operation	29
2.8 Processing of microscopy data for the study of nanowires	32
3. Methodology of AFM-based experiments with NWs	33
3.1 Electrical measurements of GaAs NWs.....	33
3.1.1 Mapping of electrical current flowing through the scan area with NWs under applied bias.....	33
3.1.2 Parametrization of the I-V curve spectral recording and data analysis.....	34
3.1.3 Studying various vertical highly p-doped GaAs NWs on GaAs substrates .	38
3.1.4 Microscopy of surface potential for visualization of charge accumulation in horizontal NWs	41
3.2 Mechanical measurements of InP NWs.....	43
3.2.1 Preliminary visualization of a sample and allocation of the inclined NWs on the substrate.....	45
3.2.2 Classical Force-Load curves method	48
3.2.3 Detailed PeakForce QNM protocol of acquisition of the flexibility profiles for separately standing individual NWs.....	49
3.2.4 Processing of the experimental QNM-based bending data for NWs	55
3.2.5 Assumptions of the applied theory and limitations of our model	56
3.2.6 Core-shell model for semiconductor NWs.....	56

3.2.7 Proposed methodical development with a sickle-shaped AFM probe for bending of NWs	57
3.3 Piezoelectric measurements of GaAs NWs	58
3.3.1 Mapping of piezo-electric current from a sample with NWs.....	58
3.3.2 Piezo-induced current measurements of vertical wurtzite NWs	59
4 Results.....	63
4.1 Analysis of experimental I-V curves for vertical nanowires	63
4.2 Simulation of charge accumulation in nanowires and influence of native oxide shell.....	69
4.3 Numerical modeling of elasticity based on bending experiment with individual tapered NWs	73
4.4 Calculation of the elastic coefficients and elastic moduli of various crystal structures by the R.M.Martin’s matrix transformation method	84
4.5 Analysis of piezo-phototronic effect with evaluation of inputs from direct piezoelectric effect coupled with photovoltaic effect	89
5. Conclusions	93
6. Summary	95
References.....	99
Publications	

List of publications

The present thesis is based on the following papers I – VII, where Pavel Geydt was the principal author and AFM investigator. The rights have been granted by publishers to include the papers in present dissertation.

- I. **Geydt, P.**, Alekseev, P.A., Dunaevskiy, M.S., Lähderanta, E., Haggrén, T., Kakko, J.-P., and Lipsanen, H. (2015). Observation of linear I-V curves on vertical GaAs nanowires with Atomic Force Microscope. *Journal of Physics: Conference Series*, 661(1), pp. 012031-1-6.
- II. **Geydt, P.**, Alekseev, P.A., Dunaevskiy, M.S., Haggrén, T., Kakko, J.-P., Lähderanta, E., and Lipsanen, H. (2016). Influence of surface passivation on electric properties of individual GaAs nanowires studied by current–voltage AFM measurements. *Lithuanian Journal of Physics*, 56(2), pp. 92-101.
- III. **Geydt, P.**, Dunaevskiy, M., Alekseev, P., Kakko, J.-P., Haggrén, T., Lähderanta, E., and Lipsanen, H. (2016). Direct measurement of elastic modulus of InP nanowires with Scanning Probe Microscopy in PeakForce QNM mode. *Journal of Physics: Conference Series*, 769(1), pp. 012029-1-8.
- IV. Dunaevskiy, M., **Geydt, P.**, Lähderanta, E., Alekseev, P., Haggrén, T., Kakko, J.-P., Jiang, H., and Lipsanen, H. (2017). Young’s modulus of wurtzite and zinc blende InP nanowires. *Nano Letters*, 17(6), pp. 3441-3446.
- V. **Geydt, P.**, Dunaevskiy, M.S., and Lähderanta, E. (2017). Opportunities of Scanning Probe Microscopy for electrical, mechanical and electromechanical research of semiconductor nanowires. *Nanowires - New Insights*, Book chapter 8, pp. 155-188. ISBN 978-953-51-3284-4.
- VI. Alekseev, P.A., **Geydt, P.**, Dunaevskiy, M.S., Lähderanta, E., Haggrén, T., Kakko, J.-P., and Lipsanen, H. (2017). I-V curve hysteresis induced by gate-free charging of GaAs nanowires' surface oxide. *Applied Physics Letters*, 111(13), pp. 132104-1-6.
- VII. Alekseev, P.A., Sharov, V.A., **Geydt, P.**, Dunaevskiy, M.S., Lysak, V.V., Cirilin, G.E., Reznik, R.R., Khrebtov, A.I., Soshnikov, I.P., and Lähderanta, E. (2018). Piezoelectric current generation in wurtzite GaAs nanowires. *Physica Status Solidi - Rapid Research Letters*, 12(1), pp. 1700358-1-5.

Author's contribution in individual publications

- I. Planning the experimental protocol of PeakForce TUNA measurements, testing of the as-grown vertical doped GaAs NWs, interpretation of the results, writing of the manuscript with co-authors. Corresponding author.
- II. Planning the samples for desired experiment and development of the experimental protocol, testing of the as-grown vertical NWs covered by different passivation

- layers, interpretation of the results, writing of the manuscript with co-authors. Corresponding author.
- III. Planning the experiment (desired samples and experimental protocol), testing of the as-grown inclined InP NWs with different phase compositions, interpretation of the results, writing of the manuscript with co-authors. Corresponding author.
 - IV. Planning the experiment (desired samples and experimental protocol), testing of the as-grown inclined InP NWs with different phase composition, interpretation of the results, writing of the manuscript with co-authors.
 - V. Testing and interpretation of the experimental results for the piezoelectric study of as-grown vertical wurtzite GaAs NWs and their stumps. Writing of the manuscript based on previously recognized results. Corresponding author.
 - VI. Testing of the horizontally fixed and as-grown vertical GaAs NWs, writing of the manuscript with co-authors. Corresponding author.
 - VII. Testing of the as-grown vertical wurtzite GaAs NWs verifying the phenomena of piezo-generation, interpretation of the results, writing of the manuscript with co-authors. Corresponding author.

In paper IV, M.Dunaevskiy was the corresponding author, performed the literature survey and numerical modeling with computer script writing for evaluation of the flexibility coefficient for NWs. In paper VI, P.Alekseev assembled the literature data and performed computer modeling of transport properties in simulating software. In paper VII, V.Sharov performed the final serial measurements of the piezo-current in NWs with switching of the illuminating laser resulting into presented values of current.

Supporting Publications

- SI. **Geydt, P.**, Alekseev, P.A., Dunaevskiy, M.S., Khayrudinov, V., Bespalova, K., Kirilenko, D.A, Haggrén, T., Lähderanta, E., and Lipsanen, H. (n.d.) Young's modulus of non-nitride III-V nanowires. *Nanotechnology*. Submitted for publication 2018.
- SII. Alekseev, P.A., Sharov, V.A., **Geydt, P.**, Dunaevskiy, M.S., Soshnikov, I.P., Reznik, R.R., Lysak, V.V., Lähderanta, E., and Cirlin, G.E. (2018). GaAs wurtzite nanowires for hybrid piezoelectric Solar cells. *Semiconductors*, 52(5), pp. 609-611.

Abbreviations, terms and symbols

AFM	Atomic Force Microscopy
C-AFM	Conductive Atomic Force Microscopy
SPM	Scanning Probe Microscopy
STM	Scanning Tunneling Microscopy
KPFM	Kelvin Probe Force Microscopy
I-V	current-voltage characteristic, i.e. spectroscopy of current by applied bias
PeakForce™	regime where the maximum force of probe-sample interaction is controlled
QNM™	Quantitative Nanomechanical Mapping regime based on the PeakForce™
TUNA™	TUNneling current measurement regime based on the PeakForce™ regime
CPD	Contact Potential Difference
DFL	DeFLection signal of photodetector in control of scanning probe position
SEM	Scanning Electron Microscopy
TEM	Transmission Electron Microscopy
edX	Energy-Dispersive X-ray spectroscopy
NW	nanowire
SOG	spin on glass (process of coating)
FIB	Focused Ion Beam
MOVPE	Metalorganic Vapor-Phase Epitaxy
VLS	Vapor-Liquid-Solid (mechanism of crystal growth)
MBE	Molecular Beam Epitaxy
GaAs	gallium arsenide
InP	indium phosphide
WZ	wurtzite (crystal structure)
ZB	zinblende (crystal structure)
q	elementary electric charge, $1.6 \cdot 10^{-19}$ [C]
k_B	the Boltzmann constant, $1.38 \cdot 10^{-23}$ [J/K]
R [nm]	radius of a nanowire
R_{NW} [Ω]	electrical resistance of a nanowire

I_d [A]	electric current flowing through a diode in forward bias
I_0 [A]	leakage current flowing through a diode in reverse bias
U [V]	applied bias
T [K]	absolute temperature
n_A [cm ⁻³]	net p-type dopant concentration in a semiconductor
μ [cm ² /V·s]	major carrier's mobility
x [nm]	coordinate
E_{mat} [GPa]	elastic (Young's) modulus of a material comprising a nanowire
F [N]	force acting toward a beam // setpoint force in PeakForce™ measurements
δ [m]	linear displacement, i.e. deformation, in the direction of applied force
ω [nm]	deflection of a beam or a nanowire
h_F [nm]	height of a local area registered by AFM for setpoint force F
h_0 [nm]	height of a local area registered by AFM for negligible setpoint force $F \approx 0$
I [m ⁴]	second moment of inertia of a beam
Q [N/m]	distributed mechanical load
L [nm]	length of a nanowire
γ [degree]	taper angle of tapered or conical nanowire
R_{mid} [nm]	average radius of a nanowire (measured from the nanowire contact with the substrate to the free end of the nanowire)
u [degree/m]	geometrical coefficient for each specific nanowire found as $u = \gamma / R_{mid}$
R_m [nm]	effective average radius of <i>deflected part</i> of a nanowire (measured from the nanowire contact with the substrate to the point of contact with the probe)
k [N/m]	linear stiffness coefficient, i.e. spring constant, of a structure
f [nm/nN]	flexibility coefficient for a nanowire
E_{core} [GPa]	elastic modulus of a core material in a core-shell nanowire
E_{shell} [GPa]	elastic modulus of a shell material in a core-shell nanowire
R_{shell} [nm]	radius of a shell for a core-shell nanowire structure
S, z, y, ρ, φ	parameters of the geometrical model of a nanowire in spherical coordinates
A, B, C, D	constants arising from solving the 4 th order Euler-Bernoulli differential equation with case-specified boundary conditions
π, exp	$\pi=3.1416..$ and exponent= $2.7183..$ (mathematical constants)

1. General introduction

Spectacular advances in materials science are visible nowadays. New materials, structures and their functions are speculated and approved in the current of scientific newsfeed and rapidly support the subsequent technological progress. The major example is how intriguing breakthroughs in electronics are supported by development of knowledge about semiconductors and nanoscale effects. At the same time, new challenges appear with new materials. For example, methods of study of nanoscale materials are quite different from approaches allowing characterization of macro-scale materials (Zhai, 2013). Complications in imaging emerge because of the need in high spatial and temporal resolution, in geometry of experimental probing, specific signal-to-noise features, inability of direct optical visualization of structures with the size below the wavelength of light (Rayleigh criterion) etc.

The object of study in this dissertation is quasi one-dimensional (i.e. resembling a thin line of material or even a thin wire) nanostructure that is called a nanowire (NW) (Lieber, 1998). NWs are tiny rod-like structures, whose development brings novel applications in optoelectronics (Haggrén, 2016), while optoelectronics was identified among key enabling technologies by EU Commission 2020 (Shahid, 2015). Importance of NW-oriented research is justified among technological goals that are supposed to improve well-being of people via novel technological solutions and markets in coming decades.

While presently NW is a "hot topic" in science with thousands of articles annually published (Kakko, 2017), with new businesses and rapidly developing novel fabrication methods, the story started from first technological works in 1960s. Wagner and Ellis published their report introducing the vapor-liquid-solid (VLS) technique allowing controlled growth of crystal whiskers in 1964 (Wagner, 1964). Later on, the solid-state community became interested in quantum well wires permitting quantization of electrical conductivity in the end of 1980s (Xia, 2003). This was followed by pioneering reports about successful growth of first NWs in beginning of 1990s (Yazawa, 1992). Further, primary groups of P.Yang (Huang, 2001), Ch.M.Lieber (Morales, 1998) and L.Samuelsen (Björk, 2002) etc. ignited the era by establishing routine ways of controlled NW growth, characterization and proposals for applications near end of 1990. Decade of 2000s was showing sustainable establishment of regular growth and versatile studies with first applications of NWs. Last decade already shown ready prototypes (Kakko, 2017) for efficient detectors, power generators, lasers etc. Nowadays, NWs represent one the most popular and studied classes of all nanostructures (Zhai, 2013) and major publication already describe ready devices based on NWs. For example, Solar cells with efficiency ~18% were shown (van Dam, 2016) (with theoretically possible >40% efficiency), development in generation of electrical power is regularly demonstrated by Wang (Zhou, 2012) and efficiencies of lasers and sensors are also continuously increasing.

Fabrication of nanostructures including NWs is known to be directed in two ways: bottom-up (assembly from molecules to nanostructures) and top-down (dismantling of typically solid-phase material from large pieces to nanoscale-sized). At the same time,

the most widespread bottom-up approaches in solid-state physics and in connection to nanoelectronics can be distinguished into Chemical Vapor Deposition, Metalorganic Vapor Phase Epitaxy (MOVPE) and Molecular Beam Epitaxy (MBE). The NW samples in present work were fabricated using “fast” MOVPE and “precise” MBE techniques.

Considering the methods of nanomaterials characterization, few prominent modern techniques can be named. Already exist a series of reviews (Giessibl, 2000; Zhang, 2007; Chen, 2017) summarizing versatile methods in nanometrology, including approaches allowing the detailed study of an array (i.e. group) or single individual nanostructures and NWs (Yu, 2013). In fact, research community indicate clear interest in study of individual NWs, because it can reveal new material- or position-related phenomena in an array and help to predict performance of the NW-based devices. Journal papers and research dissertations describing the studies of NWs with SEM (Banerjee, 2015), TEM (Karlsson, 2007), micro-photoluminescence (Gulla, 2013), Raman (Filippov, 2016), photo-acoustic spectroscopy (Leahu, 2017), cathodoluminescence (Lähnemann, 2013), X-ray Diffraction (Bolinsson, 2010), tomography (Lubk, 2014) and other techniques appeared recently. Unfortunately, one of the major experimental methods widely used to study the nanomaterials and structures is not yet presented in details of its capabilities for study of NWs. Atomic Force Microscopy (AFM) was applied in the study of NW properties in few prominent works (Wong, 1997; Dunaevskiy, 2009; Alvarez, 2011; Beinik, 2011; Halpern, 2012; Alekseev, 2013). However, all these achievements were not specified in details of the experimental measurements and we not summarized.

AFM uses a physical probe to touch and interact with the surface of a sample, while such a contact is established by a very sharp tip mounted on a physical probe as shown in Figure 1.1. AFM was brought into the topic of NWs by pioneering works of Charles M. Lieber (Wong, 1997) and Z.L.Wang (Wang, 2001) around two decades ago. However, relating of AFM to the study of NWs had strong complications due to the force control limitations as a drawback of AFM technique in the past decades. NWs were easily broken when significant physical force was applied to them due to their thinness. Previous AFM studies were executed only in Contact regime, where the force is quite large. Later on AFM was used in freshly invented Tapping regime, which leads to significant oscillations and disturbances of the NWs. Visualization of individual NWs or their array by AFM is a tricky task leading to convoluted views and artefacts in pictures, so size/shape imaging of NWs is anyhow still preferable with SEM and TEM setups. The reason for imaging of NWs by basic AFM topographic method is that recognizing the location of a NW can be combined with fabrication data about how such a structure was built and later on can be supported by the advanced AFM research. This thesis discusses the advanced AFM methods and corresponding results, which appeared due to the introduction of modern force control regimes of AFM (Kaemmer, 2011). They allow controlling the force of direct physical interaction with any sample in the level as small as 10^{-12} newtons. Remarkably, the development of this force control method was reinforced partly due to the dissertation by O.Sahin (Sahin, 2005).

PeakForce mode was introduced by Bruker company in 2008 in connection to Sahin's PhD thesis. It included software module realized as ScanAsyst feature performing

automatic regulation the AFM scanning parameters in semicontact tapping regime. More advanced modes, which will be described in this thesis, were published just few years ago: QNM™ in 2010, followed by TUNA™ in 2011 and PeakForce KPFM in 2012.

Apart from advanced AFM techniques introduced in 2008 - 2012, special attention in the present thesis is paid to critical outlook for utilization of AFM in study of NWs. Latest AFM-based experimental developments for study of NWs appeared possible based on prominent works by Stan (Stan, 2007, 2012), Wang (Wang, 2006) Alekseev (Alekseev, 2013) and Calahorra (Calahorra, 2015).

The major **motivation** of this dissertation was that ability to perform electrical measurements, mechanical strength studies, piezo-induced current measurements of individual NWs by AFM seem very attractive. This is because such studies provide a plenty of data about fabrication quality and performance of future NW-based devices. AFM-based approaches were successfully applied to NWs and AFM stations are very wide-spread. This can ignite their active use for fast and informative characterization of NWs. Thus, the **aim** of this dissertation was to recognize possibilities of versatile scanning probe microscopy methods to measure different properties of NWs: from technological characterizing quality for industrial growth to specific materials science features, allowing study of fundamental physical properties of the samples and materials, developing the methodology for study of 1D-nanostructures.

It was interesting to consider the study possible without an expensive and rare in-situ SEM visualization of AFM probe (see Figure 1.1), without protective coating of NWs for their fixation during electrical measurements or detachment/breakage of NWs for mechanical strength studies. It was important to recognize the possibility to study as-grown structures by standard device.

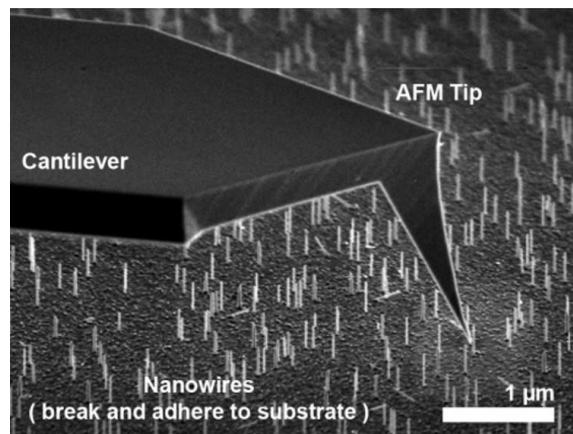


Figure 1.1 How AFM is studying the NWs? AFM probe consisting of flat flexible cantilever and sharp tip is shown above an array of vertical NWs. Adapted from (Christiansen, 2007).

The key hypotheses of the work were related with anticipations of low applicability of AFM for such object as NW due to its (1) shape and fragility, (2) poor contact with high electrical resistance that would spoil the result of electrical study and (3) independence of elastic properties from size of the nanostructure and type/linearity of such possible dependence. It was unclear if the accuracy of AFM study will be enough considering noise, instability and leakages. It will be discussed in the later sections and conclusion that major negative expectations were refuted, while part of the hypothesis left unsolved.

The task was formulated from the recent state of knowledge about NWs, AFM and problems of the NWs research performed on AFM with corresponding limitations of old modes (regimes) and capabilities of modern modes.

To explicate the AFM-based study of semiconductor NWs, one have to answer few following questions:

- Which physical phenomena can be studied in NWs by AFM?
- What basic and complicated experiments can be carried out with NWs by AFM?
- How to establish routine measurements of useful parameters of NWs with a standard AFM device, which is not quite supposed for this purpose?

In addition, it is essential to outline adequacy of this research approach (considering duration of measurements, time for learning, cost of operation and spare parts), with its principal limitations and to define the accuracy and precision of the technique.

This article-based doctoral thesis tries to address these questions. The manuscript is structured by chapters of preliminary background of the topic, detailed methodology of research, discussion of experimental/modelled results and summary with critical outlook for further research. While the current dissertation presents an article-based summary of seven peer-reviewed research Publications, the complete description of carried out works can be accessed in these seven refereed papers.

2. Basic concepts

The novelty of this dissertational study was anticipated in development of experimental AFM-based methods to study semiconductor NWs, but not in description of details of the band theory of semiconductors or crystallography aspects. Therefore, only general definitions of solid-state physics, mechanical engineering and overall principle of measuring nanometrological technique will be presented in this chapter in order to clarify the methodology (Chapter 3) and results (Chapter 4) of this work. Further details on related topics can be accessed from the refereed works.

2.1 Semiconductors surfaces, defects and depletion layer

Modern gadgets present a clear strive for miniaturization of electronic devices. However, smaller size of their elements brings new challenges related with changes in properties of utilized materials. This is valid also for semiconductor materials that became a basis for all modern calculating devices with integrated circuits based on transistors and of the most part of electronic devices like sensors, lasers, diodes, photovoltaic cells etc. Therefore, studying of the properties of semiconductor materials constituting these devices is an important task.

Among the major semiconductor materials, e.g. silicon, GaN, GaAs, InP, the latter two provide significant advantages for Solar panel technology due to their optimal bandgap (Krogstrup, 2013; Wallentin, 2013). At the same time, the surface of GaAs semiconductor material is known to be full of sites functioning as charge traps, i.e. so-called "surface states" (Calarco, 2005; Dageyte, 2018), which is a major complication for GaAs NW-based devices. Passivation of surface is a major solution to decrease the amount of surface states on the NWs, but passivation need to be chosen in such a way that these crystal lattices of semiconductor material and passivation layer would be fitting each other. Determination of such a passivation type/thickness and route/parameters of reliable coating technique are challenging. We will provide the comparison of various types of passivation coatings for GaAs NWs in Section 4.1.

Apart from only the energetic traps, the bending of conduction and valence bands also occur near the surface. Nanomaterials are known to have significant value of surface-to-volume ratio, which means that consideration of surface phenomena is essential for them.

Crystal lattices of semiconductors are periodical positions of atoms comprising the material in far range. Any disturbance of the periodicity is considered to be a defect for semiconductor crystal (Sze, 1981). The defects can be detrimental for the optical performance of the NW-based devices. These defects can be classified into 0D "point defects" (e.g. vacancy), 1D defects (e.g. dislocation), 2D surface defects (e.g. stacking fault, twin plane, grain boundary) and 3D defects (e.g. precipitate, void). For bulk semiconductors, the 0D defects are typically considered to be most important and determining the properties of the ready devices. However, exactly 2D defects such as surface states are considered dominating (Dageyte, 2018) the properties of NWs, e.g.

intensifying the recombination of carriers in the surface of NWs. Reason for this is mentioned high surface-to-volume ratio in NWs.

Real bulk semiconductors contain a plenty of lattice or crystal defects. The entire surface of a 3D crystal can be considered as a 2D defect because it limits the regularity of the lattice and consists of terminated bonds. This termination leads to a formation of electronic states (surface states) in a bandgap. Note, that the nature of the surface states for different semiconductors is highly debatable and can be caused not only by introducing a border to ideal infinite crystal, but also by formation of native oxide at the surface or by reconstruction of the surface atoms. Emergence of the surface states leads to surface Fermi level “pinning”. This leads to rises of electrostatic potential at the surface resulting in a built-in potential that is illustrated by the bending of the bands in a n-doped structure. The area with the band bending is called “depleted” of the electrons. Positively charged ions are left behind, forming a space charge region. This process continues until thermal equilibrium is reached, which is depicted by a constant Fermi level from bulk to surface (Dagyte, 2018) as seen in Figure 2.1.

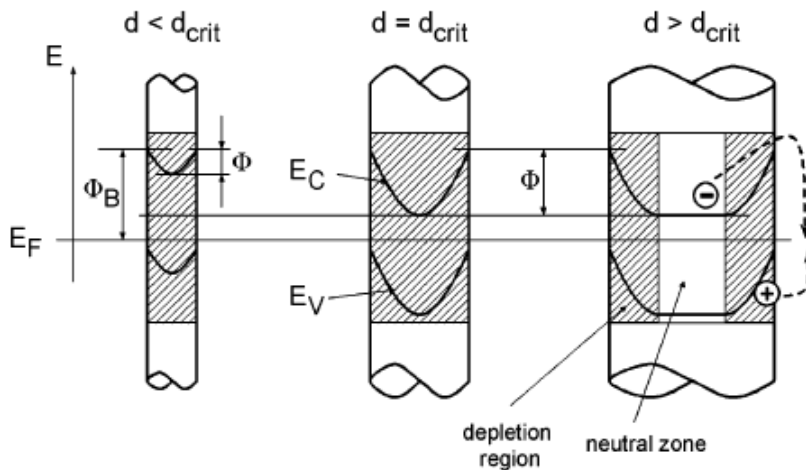


Figure 2.1 Schematics showing the dependence of depletion region (shaded), shape of conduction (EC) and valence band edges (EV), and recombination barrier Φ on the nanowire with diameter d . The arrow shows the surface recombination mechanism of the photo-excited carriers (Calarco, 2005).

Most of semiconductor NWs exhibit a depletion space charge layer with an extension of the order of the NW's diameter. NWs can appear completely depleted or with a slim conducting channels, which depends on a NW's thickness and level of doping (Chia, 2013, 2015). The behavior of size-dependent photocurrent in NWs can be described in terms of the model of electron-hole pair recombination at semiconductor surface, which

shows the strong influence of the surface toward the transport mechanisms in NWs (Calarco, 2005). Figure 2.1 presents the schematics of how the electronic conduction band (EC) and valence band (EV) are bent upward at the surface of a small-size n-doped semiconductor rod. Under light illumination, electrons are mainly localized in the inner part of the rod while holes are reaching the surface. Their spatial separation reduces the recombination of non-equilibrium carriers. Volume recombination may even be terminated, if recombination via surface traps in the forbidden band becomes the prevailing mechanism of recombination. This is because electrons would have to overcome the conduction band barrier at the surface. Reduction of rod diameter leads to complete depletion at a critical diameter and to dramatic decreasing of the rod's conductivity. Further shrinking of the dimensions causes less band curvature and following reduction of the energy barrier for the electron-hole pair recombination at the surface. With decreasing of rod's thickness, the surface recombination process is strongly enhanced. Consequently, the photocurrent decays strongly with decreasing of the energy barrier height, i.e. with decreasing the rod's thickness. The reported dependence of space charge from diameter of a NW can appear importance in many optoelectronic applications (Rigutti, 2013).

Discussion about the semiconductors in modern applications and routes for their characterization and improvements requires consideration of basic principles of scaling (Section 2.2), nanotechnology (Section 2.3) and crystallography (Section 2.3).

2.2 Nanowires: classification, size effects and nanomanipulation

Discussion about nanomaterials and size effects requires understanding of what is considered by nanomaterials itself. Many types of classification can be proposed (e.g. by chemical composition, by shape or size). Perhaps, in any way the distinction of nano- is based on nanoscale size properties of materials and effects arising from such small size (Zhai, 2013). Quasi-one-dimensionality of a structure (e.g. NW) means that it resembles a very thin object, which can be considered so thin, that its geometrical thickness can be neglected. However, this thinness is limited in real world and the real small size of material brings new properties and challenges to the structure.

NWs are quasi-one-dimensional nanoobjects with width-to-length ratio exceeding 10. Nowadays, NWs represent a group of nanoobjects from quantum wires with width typically smaller than 10 nm and related quantum confinement of the electrons to microrods where almost no size-related phenomena takes place. The names and shapes that can be found in the literature (Zhai, 2013) are the following: wire, rod, whisker, pillar, needle, column, comb, cone, belt, cable etc. However, all of the mentioned structures represent small size and quasi-one-dimensionality, which imposes certain effect toward all of these structures.

The shapes of the related nanostructures are e.g. nanosaw, nanoflag, nanoboomerang, nanocross, 1D membrane, dendrimer hairbrush, bamboo, nanosail etc. Moreover, the NWs can have completely different variants of cross-sections from hollow NWs to

triangle, rectangle, pentagonal, hexagonal, round, boomerang-like, membrane-like and oval (Zhai, 2013). All this brings new difficulties in their characterization because of the new electrical, mechanical and other models needed to be used.

Semiconductor NWs are typically fabricated as doped cylinders and have a metal cap on their top. As-grown structures are fixed on the substrates like Si or crystal material from which they initiated their growth. NWs can be arranged in core-shell structures, where the exterior is combined from atoms of another chemical element. The similar situation happens with radial p-i-n/n-i-p structures, where the doping level (n-type, p-type or insulator, correspondingly) changes through the diameter. Doping regime is controlled during the growth, while passivation can be introduced after the fabrication stage is completed.

Methods of modification like assembly and welding, after-growth, bending, milling and transporting are used to perform nanomanipulation with NWs. For example, it is typically needed to consider the substrate and NW shape/cross-section in order to fix it for mechanical bending experiment (similar to the discussed in Section 3). Shape and size of the NW can affect its electrical, mechanical, piezo and other properties. In the present thesis, we will discuss the cylindrical NWs and tapered NWs (truncated cone shape with circular cross-section).

The geometrical characteristics of NWs (length, thickness and geometrical shape of their cross-section) and doping are established during the growth procedure.

2.3 Fabrication of nanowires

The parameters of the NWs (geometrical shape and internal structure) are dependent from few major fabrication parameters. The following technological parameters have paramount influence toward the resultant nanostructures: duration of thermal regime, maximal applied temperatures; pureness of the reactive environment (level of vacuum), type of precursor flow, concentration of precursors (ratio between the precursors); material used for metal caps, material used for doping, material used for passivation and protective cover etc. This means that appropriate understanding of fabrication techniques is challenging, but attainable (REF) within the frames of modern NW fabrication methods.

As many other classes of nanostructures, NWs can be produced via top-down approach through etching of the channels in the substrate, which is inept due to low regularity and quality of nano-objects. The main method is bottom-up growth. Exist two major methods for bottom-up fabrication of NWs. First one is Molecular beam epitaxy (MBE), the method of growth on a heated substrate in ultra-high vacuum environment typically using elemental sources. It is slow, but allows thermodynamically forbidden structures to be grown. The second approach is Metalorganic Vapor-Phase Epitaxy (MOVPE). Simplified MOVPE fabrication scheme for growing the NWs is presented in Figure 2.2. (A) Different phases of the semiconductor material (e.g., Si) during the NW growth. (B)

Nucleation at the three phase boundary. (C) Ledge propagation after nucleation. (D) Complete formation of one new layer after which the process is then repeated. (E) Possible deposition pathways in a VLS system. Depending on the growth parameters, VLS growth via catalyst alloy, radial over-coating on the existing NW sidewalls and thin film deposition on substrate may occur (Chen, 2015). The radial growth regime is desirable when passivation shell layer is grown on the NW. Substrate growth is undesirable and can lead to parasitic islands of material in close proximity with the NW where parasitic electric charges can be accumulated and affect the electrical output of NW-based devices.

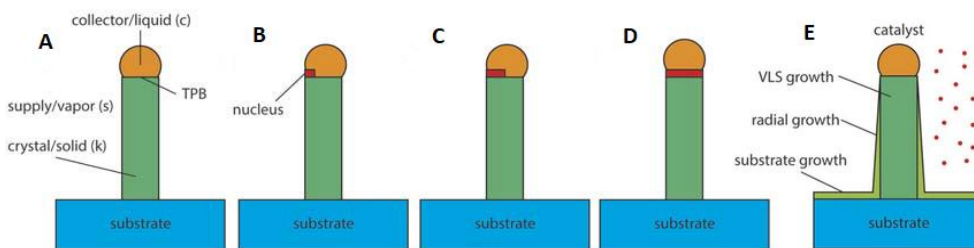


Figure 2.2 Schematic of VLS growth dynamics of NWs. Adapted from (Chen, 2015).

Doping regime is chosen during the VLS growth, so that the major dopants for GaAs NWs: are Be, Te, C, Zn, B, Mg etc. Attention is paid on details of the growth: V/III ratio, temperature, pressure, substrate, type of metal (and its coverage with nanothin film or colloid nanoparticles), doping level and type of material, precursor type – all these factors affect the size, shape, crystal structure and other parameters of the final NW.

Observation of growth can be done with in-situ TEM in atom-by-atom, i.e. disc by disc, manner. Appropriate usage of technological parameters after the growth is controlled with post-growth methods (1) by measuring the size/composition and their distribution in the array of NWs or inside individual structures by SEM, photoluminescence etc. and (2) by registering the crystal structure and its quality by TEM, edX and other methods.

2.4 Crystal structure of semiconductor nanowires

Major crystal arrangements for III-V semiconductor NWs are zincblende (ZB) and wurtzite (WZ) crystal structures. They have different mass densities causing different stability in variable temperature range. Many characteristics, including optical, conductive, chemical reactivity are different for these two distinct phases. WZ is a metastable phase in normal conditions and near room temperature. Doping, annealing/pressure, applied mechanical stress can affect the crystal structure arrangement, so that a metastable phase would result into the stable structure. Specific properties like non-centrosymmetric arrangement of atoms in the WZ hexagonal lattice lead to phenomena, which can be utilized in applied physics and by industry/technology

like piezo- and pyro- electric effects for power generation or precise positioning, chemical reactivity of surface for detectors. Similarly, specific features of band structure like in WZ GaP can bring advantages for optoelectronic devices and transistors.

Few principle crystallographic concepts should be introduced. Polymorphism means that a single chemical composition can exist with two or more different crystal structures. In general, as pressure increases the volume of a crystal will decrease and a point may be reached where a more compact crystal structure is more stable. Polytypism is a type of polymorphism wherein different polymorphs exist in different domains of the same crystal. Crystal twinning reflects the possibility to have two phases of the similar composition, but in different symmetries in one complex piece of crystal. Twin laws are expressed as either form symbols to define twin planes (i.e. $\{hkl\}$) or zone symbols to define the direction of twin axes (i.e. $[hkl]$). It can appear that both WZ and ZB structures can be found in one nanostructure, e.g. NW, so that such structure would be called a mixed phase (Jacobsson, 2015).

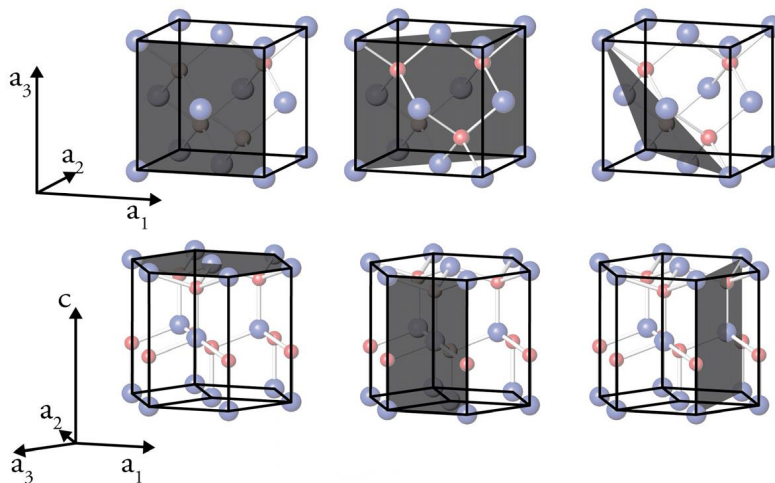


Figure 2.3 WZ and ZB crystal structures. The top row shows a ZB unit cell with (010), ($\bar{1}$ 10) and (111) planes highlighted. The bottom row shows WZ with (1000), (0110) and ($\bar{1}$ 120) planes highlighted. Adapted from (Jacobsson, 2015).

In order to characterize the properties of material in our samples, it is initially needed to specify the direction where the property is being measured. The major [1000] direction for WZ and [$\bar{1}$ 11] for ZB phases are displayed in Figure 2.3.

Crystal composition directly influences the mechanical strength of the semiconductor NWs. Irregularities of crystal quality can lead to degradation of strength, which should be controlled for real NW-based devices. Mechanical characteristics of semiconductor NWs are studied and modelled by various methods including experimental AFM-based method of Force-Load curves (See later Section 3.2).

2.5 Mechanical properties of materials in nanowires

Mechanical properties of industrial elements and devices play crucial role in electronics, mechanics, transport and many fields of everyday life. Few terms in Mechanics are often used interchangeably, but they define different parameters related with external stress applied to constructional elements. Strength is capacity to withstand maximal stress. Elasticity characterizes the linear regime of stress, where the deformation vanishes if the external force is terminated. Rigidity is characterizing the extent to which an object resists to be deformed. Flexibility is the inversed value of rigidity. Plastic deformation, on the contrary from elastic one, means that the structure changes its shape irreversibly due to the force/stress applied. The hardness is a measure of resistance toward indentation. Significance of elastic and plastic moduli for practice is related with utilization of certain sizes of elementary elements in order to achieve the strength of the final object. This is valid for both macroscale object architecture and nanoscale technology and mechanics.

We will further describe elongated beams due to the interest in studies of the NWs. Figure 2.4 presents the case of a deformed rod-like beam, where the lower part experiences tension, upper part experiences compression and there is also a neutral axis where no elongation or shrinkage take place. The AFM probe is touching the stretched (under tension) side of a deformed NWs in the AFM-based methods described in later Section 3.2 of this thesis. It is needed to describe a beam by its geometrical features and material properties. The classical XVII century body compression law (Hooke's law) describes the properties of a structure by associating the applied force with the stiffness of a structure and observed geometrical deformation. However, it does not denote the elastic property of the material itself. Euler-Bernoulli beam theory introduced in XVIII century defines the relation between characteristic of material with structure's geometrical shape with applied impact for linear beam across its length.

Since the quasi-one-dimensional NWs are in reality three-dimensional objects, the volumetric theory need to be applied to characterize their elasticity. Three major theories are related to three-dimensional theory of elasticity: (1) Euler-Bernoulli, (2) Rayleigh (1894) and (3) Timoshenko (1921) (Labuschagne, 2009).

These three theories are different in the basic assumptions related with movement, stresses and deformation of material inside the beams. Timoshenko beam theory explains how the stresses are distributed in a structure where the free end of the beam experience rotation and causes shift of the planes located perpendicular to the beam's neutral axis. Timoshenko theory has the most difficult calculus because the inertia of the rotation is taken into account, which leads to a change in the expression for the kinetic energy of the beam. It is also assumed that the cross-sections remain flat, but not perpendicular to the deformed axis of the beam (Erofeev, 2011; Bepalova, 2018). Rayleigh beam theory is slightly less demanding in prerequisites, because it takes into account the rotational inertia of the cross-section, but omits the shear deformation. Euler-Bernoulli beam theory specifies the simple case when the cross-sections to the axis perpendicular to the force applied do not shift in positions (see Figure 2.4 with Timoshenko and Euler-Bernoulli beams).

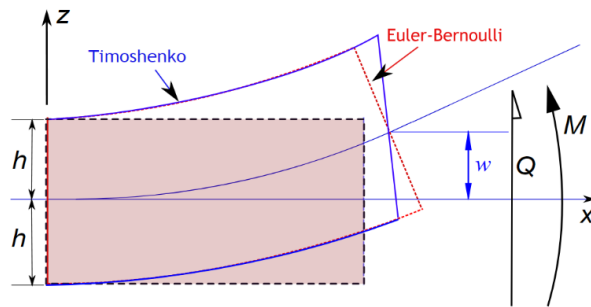


Figure 2.4 Deformation of a Timoshenko beam (blue) compared with that of an Euler-Bernoulli beam (red) (Erofeev, 2011).

In general, Euler-Bernoulli beam theory is applicable to stiffer beams with significant length-to-diameter ratio, which fits the description of such object as semiconductor crystal NW. Therefore, we considered exactly the Euler-Bernoulli beam theory as an adequate basis for description of the elastic properties of NWs. The validity of the proposed model is related with the model limitations (Section 3.2) and the major assumptions of the classical Euler-Bernoulli beam theory. There are the following four of them (Erofeev, 2011; Gere, 2012):

- 1) The cross-sections of the beam are flat and perpendicular to the axis of the non-deformed beam (in rest). They also remain flat and perpendicular to the deformed axis of the beam after the deformation (during the bending).
- 2) The normal stresses on areas parallel to the axis are negligible. The longitudinal sections resist bending independently, without influencing each other.
- 3) The inertia of rotation of the rod element is neglected.

Typical applications of Euler-Bernoulli beam theory consider the fourth order differential equation solved for the cylindrical beam. We will utilize the Euler-Bernoulli beam model in Section 3.2, where we specify the need to deduce an analytical solution form valid for a conical beam (model of tapered NWs), which will be presented in Section 4.3.

2.6 Scanning Probe Microscopy: major regimes of operation

Atomic force microscopy (AFM) (Binnig, 1986) is a part of Scanning probe microscopy (SPM) family of methods. They were established in 1982 from the first Scanning tunneling microscope (STM) (Binnig, 1982) being built and used to resolve individual atoms. The general scheme of the AFM and the entire setup are shown in Figure 2.5. The AFM consists of the sharp probe attached to the flexible cantilever, piezoscanner, optical detecting system (laser and photodetector), feedback system and computer control. The AFM probe touches the sample and moves laterally along its surface, while the

information about local heights (and multiple other local properties) is recorded by the computer.

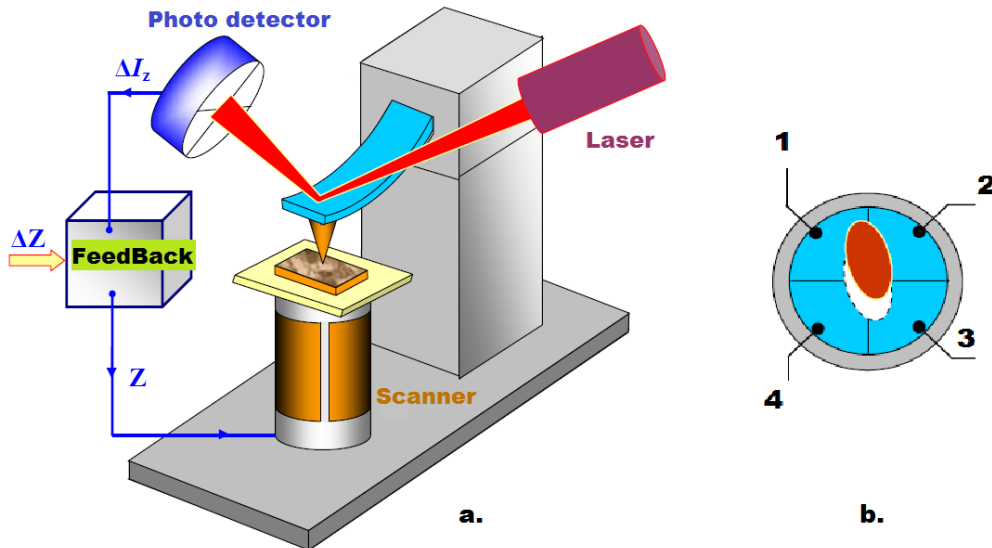


Figure 2.5 (a) Simplified scheme of the AFM and (b) photo detector with laser spot moving on the photodetector during the scanning (Mironov, 2004).

When the AFM probe touches the sample it is considered to be in direct mechanical contact with it. The atoms of the probe and the sample experience the influence of van der Waals attraction force (which is the dominating force for the large tip-sample distances $r > 5\text{nm}$) and Pauli repulsion (the major acting force for the small tip-sample distance $r < 0.5\text{nm}$). The balance of these forces is defined by the well-known Lennard-Jones potential. Different acting forces during the process of AFM tap are shown in Figure 2.6. When the probe is very far from the sample, almost no forces act between them. With decrease of the tip-surface distance the force become attractive (van der Waals force), although at some point (lowest point of the red curve) the repulsive Pauli interaction force is increased. It starts to dominate from the point (Figure 2.6) where the red curve intersects the zero-potential level, which is continued to the left with the repulsive force of interaction. Typically, AFM measurements are carried out in the area slightly to the left from the intersection point of zero-potential, thus balancing the Pauli repulsion with van der Waals interaction.

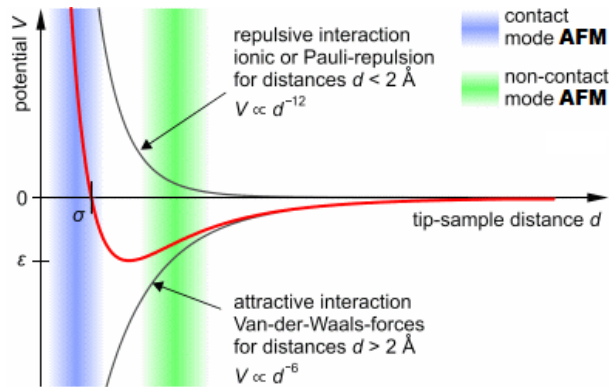


Figure 2.6 Lennard-Jones potential curve. Image Copyright of Soft Matter Physics Division, University of Leipzig, Germany.

One of the major components of the microscope is the probe. The scheme of the probe and SEM image of the AFM probe are shown in Figure 2.7. There are dozens of various types of probes, differentiating by their sharpness, conductivity, flexibility of the cantilever, size of the tip etc. The probe is mounted on millimeter sized chip that is placed in the probe holder of the AFM. The probe consists from the flexible long console called the cantilever and the $\sim 10 \mu\text{m}$ size pyramid at its end. This pyramid ends up with the sharp tip. The sharpness of the probe is defined by the pyramidal angle and the tip radius.

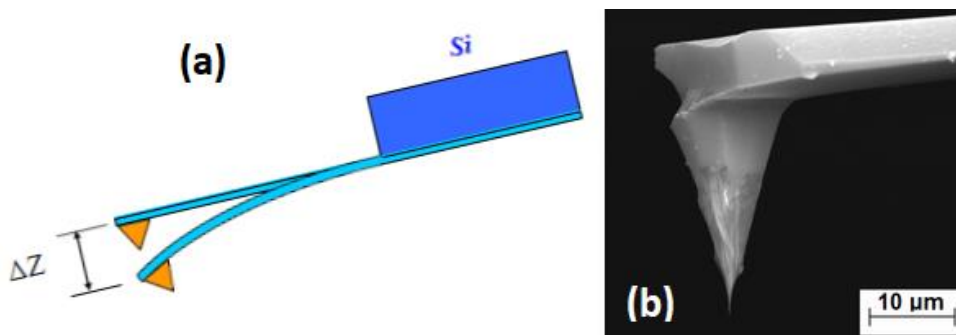


Figure 2.7 (a) Cantilever schematics. Adapted from (Mironov, 2004). (b) Exemplary SEM picture of a real AFM probe. Image Copyright of Carl Zeiss Inc.

The schematic diagram of scanning process (Mironov, 2004) is shown in Figure 2.8, where horizontal lines represent the movements of the AFM probe in fast scanning direction. Red lines with arrows are representing the straightway movement of AFM probe, while blue lines represent forward movement. Data recording is performed in straightway: j is number of pixel line, “ i ” is number of position. The number of “ i ” and “ j ” are typically between 32 and 1024. For the study of mechanical properties of the InP

NWs it was favorable to preset high value of “ i ” with small value of “ j ”. This allows very detailed scan profiles with high lateral resolution along the horizontally oriented structure and affordable duration of the scanning process. Excessive duration of the scanning lead to significantly pronounced sample drifts, which could decrease the quality of produced topological images and further processing of the deformation data.

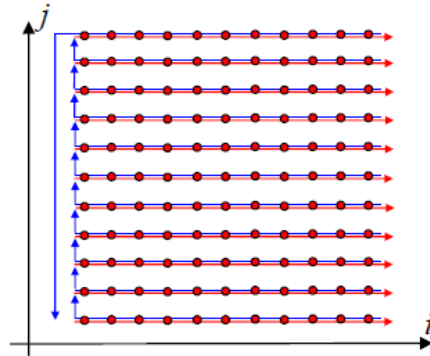


Figure 2.8 Trajectory of the AFM scanning points during the scanning. Red lines are in “Trace”, while blue lines are in “Retrace” direction. Typically, data from the Retrace is recorded/analyzed (Mironov, 2004).

2.7 PeakForce mode: TUNA and QNM advanced regimes of AFM operation

The PeakForce mode of AFM presents the idea that semicontact regime of scanning can be done in such a way that the force of interaction between the AFM probe and the sample is controlled all the time. This appeared possible due to the development of modern fast computers and fast electronics for signal processing. In 2009 Bruker company has introduced their PeakForce regime (Kaemmer, 2011) and further on supported it with Quantitative Nanomechanical Mapping regime (Pittenger, 2012), where it was possible to observe the values of elastic modulus, adhesion, deformation for the scanned areas of the sample simultaneously with the routine topography.

It must be said that amount of points acquired by the AFM controller is typically 500 per one cycle, while one cycle lasts as long as inversed PeakForce frequency. Typical PeakForce frequency is 2 kHz, which means that the probe taps onto the sample 2000 times per second. This also means that 1 million data points are processed by the hardware and software every second. The most impressive here is that it appeared possible to distinguish different areas of the force-time data in such a way that each cycle, i.e. tap, can be presented from repeatable segments (indicated as A-E in Figures 2.9 and 2.10).

“A” represents the approach with almost no interaction. “B” represents the moment when deformation of the sample begins. “C” represents the moment when the highest force during the tap occurs. “D” represents the adhesive attractive force existing due to

meniscus of liquid or van der Waals interaction between the probe and the sample. “E” represents the withdrawal moment when some oscillations still can take place due to detachment of the probe from the sample (Pittenger, 2012).

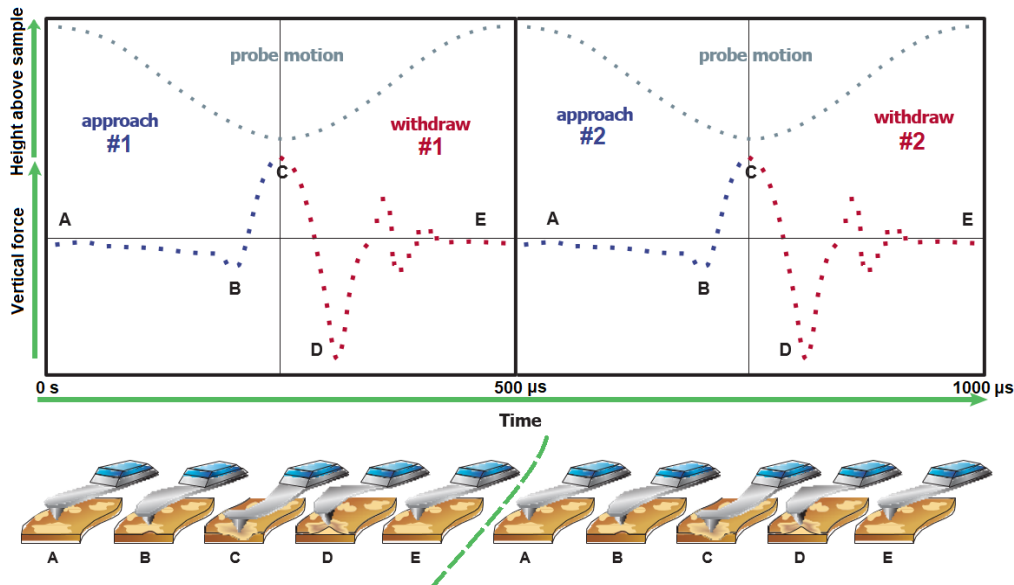


Figure 2.9 PeakForce regime. Adapted from (Pittenger, 2012).

These cycles are following each other, so that the scan goes along the fast scanning direction and registers the properties of the material with high resolution of AFM. The AFM probe is performing the oscillations above the sample with the amplitude typically around 150 nm. The probe is decelerated slightly before the moment of time when it is supposed to touch the sample in order to decrease the acting force and to enlarge amount of the data points in the closest proximity with the segment “C” (contact with the surface), which is done to monitor and control the value of PeakForce. Furthermore, it becomes possible even to scan the samples with negative force of interaction, because the system tracks the change of the force and recognize the position “C” even if attractive force is acting instead of repulsive. One practical moment here is that adhesion value is dependent on the state of the surface and material of the probe. In addition, it depends on the media where the scanning is done, as for example the studies in liquid would erase the adhesive interaction. Moreover, combination of these cycles has own dynamic curvature, which is filtered, but not in a perfect way, thus it can affect the values measured. Interestingly, the region between C and D is associated with stiffness of the sample, which can be used for the studies of elastic modulus of many materials. Unfortunately, this seems not valid for bendable objects, which will be discussed with the protocol of how to overcome this disadvantage in the Section 3.2. Should be noted that direct mechanical contact during the tap lasts only few microseconds.

The schematic images seen in the lower part of the Figure 2.9 show how the cantilever is being deformed during every time moment of the PeakForce tapping cycle. The actual deformation of the probe (also shown in Figure 2.7) is in the order of few nanometers.

PeakForce TUNA regime combines the data acquisition of topography in PeakForce mode, recording of the mechanical characteristics in every point of the scanned area and additionally it registers the current (See Figure 2.10). The left part of the Figure 2.10 represents the movement of the probe in vertical Z position in nm, force of probe-sample interaction in nN and the electrical current flowing through the probe-sample contact in nA. The current flows through the amplifier, sample and AFM probe when external bias is applied between the probe and the sample. Here it is possible to see that the current is flowing during the time of direct probe-sample mechanical contact between the probe and the sample. At the same time, current can flow when the adhesive moment D occurs, i.e. even without mechanical contact. This is leading to opportunity that the highest current can flow not only in the moment C. The current recorded in the moment C is called PeakForce current. While the map of highest values of current per every tap (pixel) is the map of Peak currents. The map of currents can be seen in Figures 3.1a and 3.4cd. Independently from that, it is possible to perform the spectroscopy of current in a way of taking the I-V curves, or current-voltage characteristics of the sample.

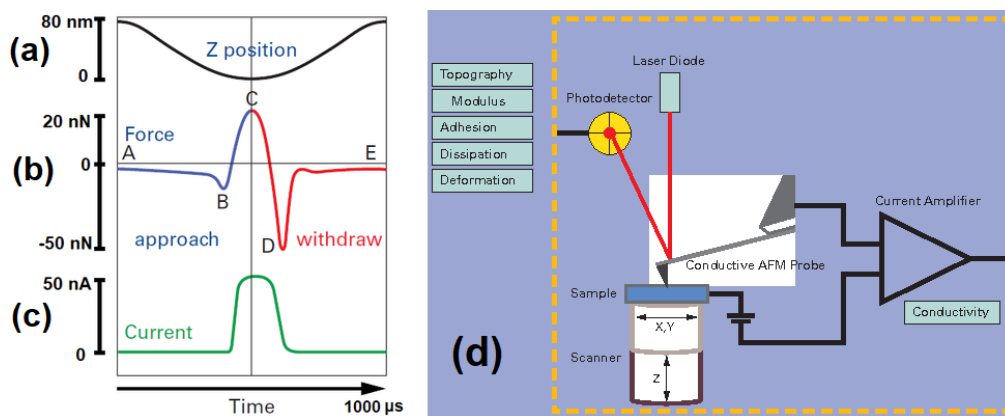


Figure 2.10 PeakForce TUNA regime with the mode schematics. Adapted from (Li, 2011).

As the PeakForce TUNA mode was realised in 2011 (Li, 2011), there was no significant amount of research with this method was existing in the beginning of studies described in this dissertation. Hence, recognizing the capabilities of these modern modes (PeakForce, QNM and TUNA) for study of versatile nanoscale objects was one of the main motivations of this work.

The range of electric currents allowed by the PeakForce TUNA module is $\sim 0.5 \mu\text{A}$ with the accuracy below 1 pA and the bias range is $\pm 10 \text{ V}$. The mode schematics with electric current amplifier is shown in Figure 2.10d. The PeakForce frequency used in

Tuna regime is 1 kHz, which doubles the typical duration of direct contact during one tap and corresponding current flow. This can be later increased by decreasing the PeakForce amplitude of tip oscillation.

2.8 Processing of microscopy data for the study of nanowires

Major difficulties with the data acquisition are related to scanner creeping (Mironov, 2004) and data processing issues. Other image artifacts result from the influence of the AFM tip shape. Tip sharpness is a combination of the tip radius with the tip angle (see Figure 2.11). Additional difficulty for the NWs emerges due to slipping from the surface of the studied structure and deformation of the conductive coating of the tip. Latter effects can disturb resulting topography, electrical conductivity and mechanical deformation data.

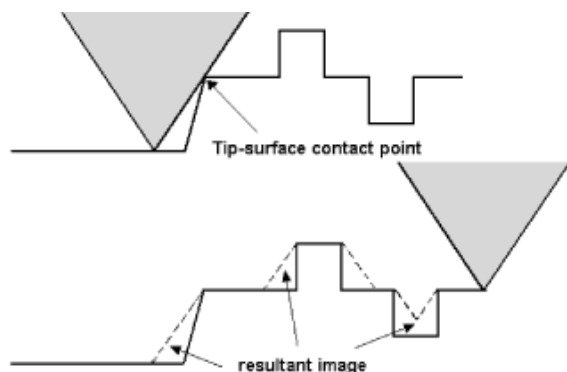


Figure 2.11 Schematics of the tip scanning the surface and corresponding tip convolution effect, which is the major artifact of the topology for vertical and inclined NWs. Adapted from (Bernardes-Filho, 2005).

The convolution of tip with high NWs results in the pyramidal shape objects to be found on the substrate at the locations of NWs. The highest point in the height data (the summit of the pyramid) directly indicates the location of the metal cap. The convolution of NW images is very significant and leads to necessity to use SEM or any other visualization tool to recognize the real shape of these objects. At the same time, the data about the highest points on the NWs can point out the location of the metal caps in order to perform the I-V curves spectroscopy. The spines of the inclined NWs can be easily determined and used to perform the bending experiment, because the spine represents the highest profile line on the NW. Mapping of piezo-current can bring the numerical values of current while the shape of the NWs would be determined by some other method.

3. Methodology of AFM-based experiments with NWs

The protocol of the experimental technique used in this dissertational study will be presented in this chapter. Section 3.1 presents some details of experimental procedure for acquisition of I-V curves from Publications I, II and V. The analysis and equations allow finding the mobility, influence of ramping velocity, surface states issues, threshold bias values, dependencies of polarity of applied bias and stability of contact (particularly reliant on the Setpoint force of push by a conductive AFM probe) that will be discussed in Sections 4.1 and 4.2. The most extended and detailed description is given for procedure of mechanical measurements in Section 3.2, because they were considered as most laborious, but prolific for future research with NWs. Part of the instrumental details with required experimental procedures were not previously specified in Help section of a commercial microscope or other related literature. The author sincerely tried to find the sufficient minimum of required parameters of the study and fetch out the methodical details allowing to avoid the reception of spurious phenomena in study of NWs. Most of the steps of feedback system and cantilever calibration, PeakForce parametrization and data analysis presented in Section 3.2 are valid also for electrical and piezoelectric experiments. However, the protocol of piezo-current observation in vertical NWs in Section 3.3 is provided for the station without the PeakForce control.

3.1 Electrical measurements of GaAs NWs

In order to perform the electrical measurements of the NWs the substrate, where they are located, must be highly conductive. A special conductive AFM probes need to be used. The contact resistivity is a major parasitic parameter that can spoil the measurement (Zhang, 2007; Talin, 2010). Instability of contact would lead to noise on the I-V curves. Therefore, special attention need to be paid to establishment of the stable contact between the AFM probe and the studied NW. We tried to gather experimental guidelines and discommends from essential works (Lin, 2006; Werner, 2009; Dunaevskiy, 2009; Talin, 2010; Alvarez, 2011; Beinik, 2011; Xu, 2012, 2015; Alekseev, 2013; Chia, 2013; Rigutti, 2013; Rojo, 2013; Lord, 2014, 2015) related with experimental probe-based electrical characterization of single NW-like structures and analysis of their transport mechanisms

3.1.1 Mapping of electrical current flowing through the scan area with NWs under applied bias

Lateral scanning is a variation of position x [nm] on the surface of the sample when some specific parameter is recorded into its data channel. If the registration of coordinate is accompanied by the recording of electrical current values under constantly applied bias, then such technique is called C-AFM regime, e.g. PeakForce TUNA™ (Li, 2011). Such mapping of electrical current in the scanned area can indicate the locations of the most conductive sites, i.e. NW caps, which accordingly allows finding the most conductive NWs from an array.

Figure 3.1a represents the 3D topography model of the NWs array with the electric current recorded by TUNA module being superimposed onto topography in real XYZ

dimensions. This makes it possible to determine the conducting regions on the studied surface (see yellow circles at Figure 3.1a). In addition, it is possible to analyze the histogram of current values (Figure 3.1b) along the mapped area. In the presented case there was no significant features of conductivity (absence of any peaks in the histogram).

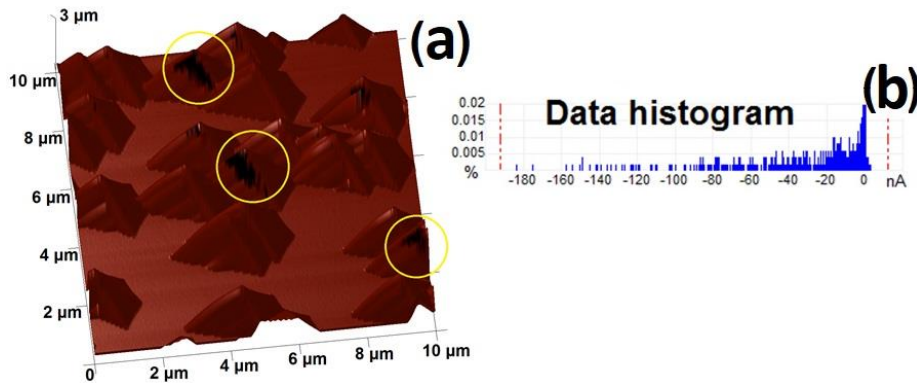


Figure 3.1 (a) 3D representation of topography of an array of vertical GaAs NWs, where NWs are seen as pyramids due to convolution of AFM tip's shape. Electric current map is superimposed onto 3D topography indicating regions with high current density near the NW tops as black spots marked with circles. (b) Distribution of values of electric currents in an array of NWs obtained by PeakForce TUNA module, where highest absolute values indicate stable electric contact.

The reason for variation of conductivity of the NWs in a seemingly regular fabricated array can be in a local variation of properties among the NWs. Few parameters focused toward fabrication of a perfect array of identical NWs can hardly be controlled in MOVPE and MBE techniques along the entire area of a treated substrate. As a result, few following NW's features can be responsible for variation of conductivity of nearby standing NWs: (1) distribution of doping material inside NW; (2) local internal defects with (3) associated concentration of surface states; (4) diameter of metal caps establishing the area of metal-semiconductor contact; (5) variation of forms of the metal caps etc. The latter parameter is directly influencing the geometry of contact in C-AFM experiment and the corresponding surface area of tip-cap contact, which defines the value of probe-NW contact electrical resistance.

3.1.2 Parametrization of the I-V curve spectral recording and data analysis

I-V curves (current-voltage characteristics) are plots presenting the data of scanning of electrical current under different voltages applied between the C-AFM probe and a studied conductive sample. I-V curves are taken in a single spot on the sample, allowing the lateral resolution in the order of the size of the C-AFM tip radius, i.e. ~20 nm. This

resolution is worse than for STM (Timm, 2013) previously applied for a similar task with NWs, but AFM stations are significantly more wide-spread and simpler in operation, so we focused our attention on C-AFM. Should be noted that SEM-coupled stations and multiprobe-SEM stations (Lord, 2014, 2015) allow visualization of established contact, but they are significantly more expensive and rare than C-AFM. Moreover, these exotic SEM-based stations are not required for separately standing NWs with diameters (and size of metal caps) in the order of 5 - 200 nm because NW locations can be easily reconstructed from (convoluted) AFM images. I-V curves are recorded to recognize the details of NW structural arrangement, e.g. quality of metal-semiconductor contact as height/width of the Schottky energy barrier, property of NW-substrate contact and influence of surface states and their passivation to NW's conductivity. The acquired I-V plot is considered together with anticipated carrier transport mechanism and fabrication parameters of the NWs. Further, the detailed parameters of the NW, i.e. its conductive arrangement, can be simulated so that a computer model can be compared with the results of the numerical model and experimental data.

We assume that the electrical contact resistance was negligible for all I-V curves in Publications I-III, V and results analyzed in Sections 4.1, 4.2 and 4.5 of this thesis. Conviction of negligibility of the contact electrical resistance can be argued based on: (1) low resistance of metal in NW caps and metal of AFM tip coating; (2) low resistance of typical metal-metal contact even in ambient environment with humidity leading to water layer surrounding the structures and (3) insignificant noise visible from repeatable I-V curves. Considering the latter issue of noise, any instability (e.g. dribbling or sliding) of mechanical contact should lead to change in surface area of established contact, thereby affecting the related electrical resistance of such contact. This should lead to noise in the I-V curves, which was not observed, so we conclude that the AFM-NW electrical contact was stable and highly conductive.

Combination of ramping (i.e. recording the spectroscopic data in direct contact between the probe and sample) with careful landing to the sample, when the force of probe-sample mechanical interaction during the approach is controlled by the AFM controller electronics module in PeakForce mode allowed repeatable I-V curves without damaging the conductive coating of C-AFM tips. In fact, intensive change in scan height of AFM due to high aspect ratio of scanned objects (i.e. NWs) can lead to wearing of 10-20 nm thick conductive coating of the tips or its deformation. We used the PFTUNA probes for all the I-V curve measurements.

Should be mentioned here that I-V curves in our experiments were recorded in such a way that initially applied bias was the highest negative, e.g. -4 V in later Figure 3.3a. The curves typically consisted of 512 separate datapoint measurements recorded during the sweeping duration selected for each I-V curve registration. Sweeping duration was selected in range 1 - 10 seconds, while typically it was 5 seconds (based on 0.2 Hz ramping frequency specified in AFM software). These parameters allow quantifying of both (1) critical voltage step and (2) time interval between the recorded datapoints (See points clearly visible in Figure 3.2).

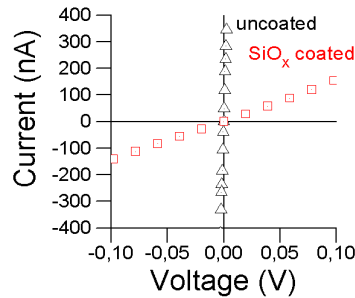


Figure 3.2 I-V curves of unpassivated GaAs NWs grown on p-GaAs substrate: uncoated (black) and coated by SiO_x layer (red). Separate datapoints indicate the voltage step of the measurements ~ 0.39 mV (black) and ~ 19.53 mV (red) with the current step of the measurements ~ 4.30 nA. The image is inset to later Figure 4.1b. Adapted from Publication I.

In relation to the voltage step, an entire range of bias for NanoScope software and Multimode 8 controller electronics provides bias from -10 V to +10 V, i.e. summarized variation of 20 V is available. The number of segments in the entire scale for this controller is 64000 according to the device Help. Recognizing the number of quantized digits allows calculating the minimal achievable bias step for this AFM device as $20 \text{ V} / 64000 = 0.3125 \text{ mV}$ per consequent bias steps. Such quantization can be considered rather detailed and typically leads to smooth I-V curves. Thus, the continuous combination of electrical current datapoints recorded for each different externally applied voltage between the substrate and an AFM probe is visualized as the I-V curve of an individual NW. The I-V curves presented in Publications I, II, V - VII were not filtered, which verifies the applicability of C-AFM based on (1) low noise and (2) current resolving ability to study the resistive behavior of individual vertical NWs.

Furthermore, recognizing the size of the digit (~ 0.3 mV) has paramount importance for highly conductive structures like the GaP-passivated pGaAs NWs without SOG coating shown in Figure 3.2 (and later Figure 4.1b). The critical digit size calculated above (0.3 mV) has paramount importance for the measurements of the most conductive samples, where the ultimate precision is required. For typical measurements of doped NWs, although, typical values of applied voltage step are calculated as the actual voltage range divided by the number of datapoints in the direction of voltage variation. For example, the entire voltage range seen from the horizontal axis in Figure 3.3a is calculated as $1.5 \text{ V} - (-4 \text{ V}) = 5.5 \text{ V}$. The number of datapoints in the direction of voltage variation is typically 512 (parameter "Number of counts" in the AFM software) divided by 2 because bias recording is typically done in two directions, i.e. both initial increasing and later decreasing of bias are consequently recorded. Such a voltage step ($5.5 \text{ V} / 256 = 21.5 \text{ mV}$) is significantly bigger than the critical size of one digit of bias change (~ 0.3 mV). This can appear important because the adequate characterization of the plot requires a number of datapoints being analyzed, while the current values are also limited. The amperemeter of our AFM station allows the range of approximately -550 nA to +550 nA being recorded, so that the entire range of our device is $\sim 1.1 \mu\text{A}$. This leads to a conclusion

that in accordance to the Ohms law, the smallest resistance of the element, e.g. NW, for 21.5 mV is found as $21.5 \text{ mV} / 1.1 \mu\text{A} \sim 20 \text{ k}\Omega$ can be registered, what is even worse, on the basis of only two experimental points. This is insufficient resolving ability, so the range of the voltage should be reduced or amount of datapoints should be increased. For example, the bias scale for the highly conductive GaP-passivated pGaAs NW without SOG coating shown in Figure 3.2 is from -0.1 V to 0.1 V, i.e. entire range is 0.2 V. The number of datapoints was 1024, which leads to bias digit size in direction of increasing voltage calculated as $0.2 \text{ V} / 512 = 0.39 \text{ mV}$ (see Figure 3.2). This value is close to the critical step size of the controller, so that a few datapoints can appear not well resolved. However, it was possible to calculate the inclination of the black curve and evaluate the resistance of the measured NW. In that case, the resistivity was very small, but two approaches can be proposed in order to develop the method of measurement. Firstly, the module for higher currents can be used, so that limits of current will become bigger than $1.1 \mu\text{A}$. Secondly, it can be possible to introduce a calibrated resistor into the electrical cycle to increase the resistance in a controlled way followed by recalculation of the R_{NW} .

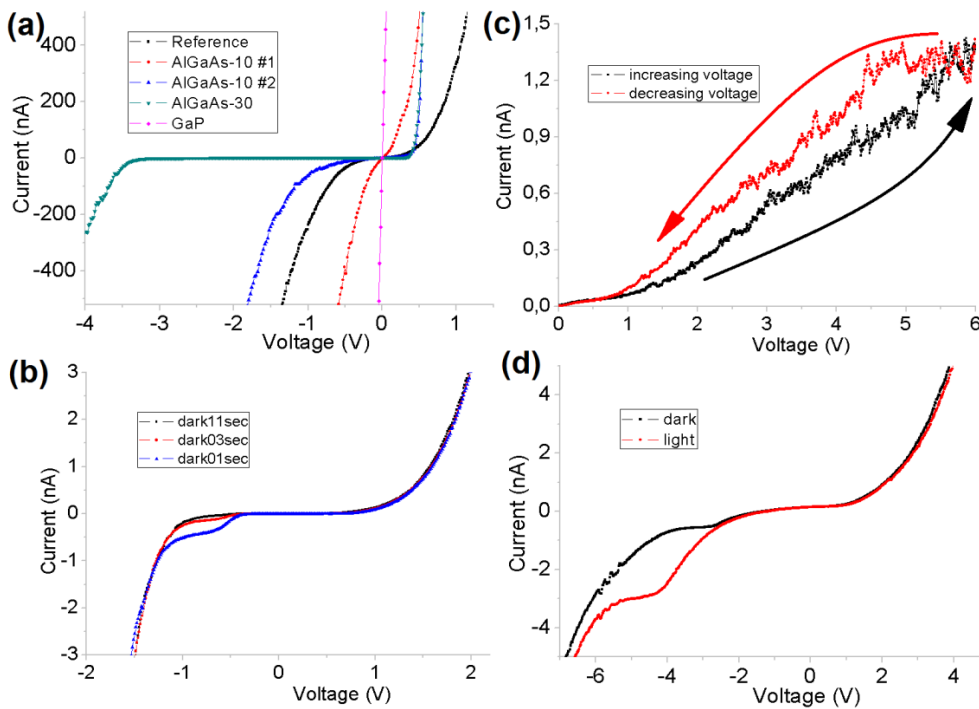


Figure 3.3 I-V curves for pGaAs NWs taken by SPM. (a) Comparison of passivation layer influence for conductivity of AlGaAs-passivated (two NWs with thickness 10 nm and one NW with thickness 30 nm) and GaP-passivated vertical NWs. (b) Indication of effects of sweeping duration onto accumulation of charges in vertical NWs for 1 s, 3 s and 11 s I-V curve recording time. (c) Hysteresis of electric current for horizontally fixed pGaAs NW (in geometry shown later in Figure 3.7a). (d) Comparison between electric output of a vertical NW standing on nGaAs substrate in light and dark conditions. Adapted from Publication V.

It can also appear that resistance of the studied element will be large or inclination of the rectifying curve will be very small. In such a way, the resolving ability (precision) of the amperemeter in "High current" mode (~ 35 pA) can be improved by utilization of "Low current" mode with precision ~ 375 fA. These two modes utilize two separate amplifiers.

In relation to the time interval between the recorded datapoints, not only the digitization of voltage and current, but the rate of variation of bias can have influence toward the registered values of current and shape of the I-V curves. This is highly possible when fast states are responsible for the accumulation of electric charge in the NW. It was mentioned earlier that time interval between the recorded datapoints can be also calculated to understand the influence of sweeping rate. By recognizing the sweeping duration and number of datapoints, we can calculate the time interval between the two consequent levels of voltage applied between the substrate and a C-AFM probe. If the duration of I-V recording is 5 s for scanning of current in both directions (increasing and decreasing of voltage) and number of datapoints is 512, then the time interval is calculated as $5 \text{ s} / 512 \sim 10$ ms. The effects of sweeping rate were initially tested for the pGaAs NWs on the pGaAs substrate as shown in Figure 3.3b.

Therefore, apart from the influence of length, diameter and passivation layer (See Figure 3.1a and later Section 4.1), we have observed the influence of the sweeping rate (Figure 3.3b and later Section 4.2). Later we observed the hysteresis emerging due to the carrier accumulation in the NWs resulting into the hysteresis of the I-V curves (Figure 3.3c and later Section 4.2) and influence of illumination toward the I-V characteristics of GaAs NWs (Figure 3.3d and later Section 4.5). These observations were used to understand the influence of the charge accumulation in native oxide of GaAs NWs (described in Publication VI and Section 4.2), and to model the photovoltaic power generation from GaAs NWs (described in Publication VII and Section 4.5), which seem useful for modern NW-based technologies.

3.1.3 Studying various vertical highly p-doped GaAs NWs on GaAs substrates

8 samples (See Table I and Publication I) were fabricated in order to test the capabilities of AFM by examination of vertical NWs and have a first glance on applicability of AFM for the NWs. Scanning topography is shown in Figure 3.4, capability to perform current-voltage measurements and general issues with resolution/repeatability/noise are discussed in the present Section of thesis. NWs were grown by VLS mechanism inside MOVPE chamber (described in Publication I) in the Nanoscience and Advanced Material research group in Aalto University (Micronova Research center) in Finland. Four parameters were different: height of NWs, existence of passivation, existence of SOG coating and type of substrate doping.

At first, we performed the preliminary observation of the NWs, or so-called large-scale survey scans. It is possible to compare the SEM images with AFM topography images accounting the tip convolution effect discussed previously. SEM images and 3D topography of ZB GaAs NWs from the first series discussed in Publication I are shown

in Figure 3.4. Here it should be noted that in Figures 3.4cd an electrical current channel image was superimposed on the topography image, which was used to highlight the areas with the property of interest (areas of high conductivity). White and red colors in Figures 3.4cd do not mean any relation with difference in conductivity, but results from the color scale overlaid. Red color in this case was indicating the areas with no current on the mapped area. Focusing on a certain region of values shifts the balance of white on the image. Since the color scale used in AFM data processing software shows color gradient, red appears between the white (positive current) and black (maximum negative current).

Table 1. Specification for the vertical ZB GaAs NWs with diameters ~ 150 nm from Publication I. Existence of passivation shell is shown in rows, while type of substrate doping is given in columns. The numbers are corresponding with curves are associated with the results shown in later Figures 4.1 and 4.2. The colors correspond with no SOG layer (**black**) and covered with ~ 0.5 μm thick SOG layer (**red**).

shell \ substrate	p-type doping level: $1.3 - 1.6 \cdot 10^{19} \text{ cm}^{-3}$	n-type doping level: $1.6 - 3.9 \cdot 10^{18} \text{ cm}^{-3}$
non-passivated height: $2.3 \mu\text{m}$ (growth time 120 s) doping: diethylzinc flow 1 sccm	1a 1a	2a 2a
GaP-passivated height: $1.1 \mu\text{m}$ (growth time 45 s) doping: diethylzinc flow 5 sccm	1b 1b	2b 2b

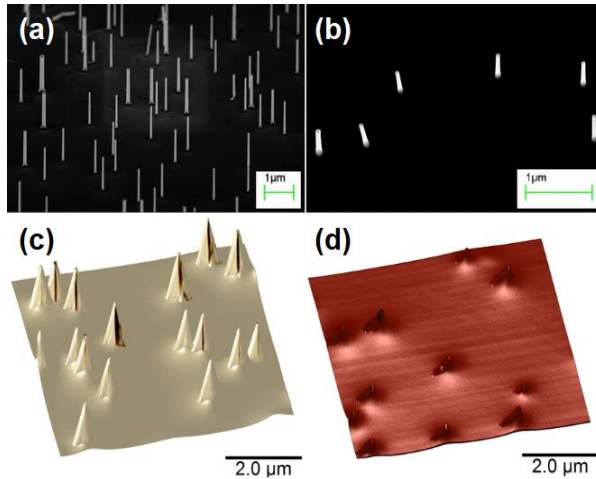


Figure 3.4 SEM (a), (b) and AFM 3D (c), (d) images of GaAs NWs array from the Publication I. (a), (c) uncoated; (b), (d) coated by $1 \mu\text{m}$ thick SiO_x layer. The conductivity image “skin” with black conductive spots is superimposed on AFM topography image. The conductivity map was recorded when bias $U = -2\text{V}$ was applied to the substrate.

In addition, small bright rectangle can be visible in Figure 3.4a for the area with central NWs. This indicates the effect of charge accumulation in the sample studied by SEM. Remarkably, we carried on specific experiments to investigate the charge accumulation of electric charge in surface of NWs by C-AFM and computer simulation, which are discussed later in Section 3.2 of this thesis.

The simplest schematics of the experimental AFM-based experimental setup used for studies of electrical conductivity is shown in Figure 3.5. It depicts the highly doped GaAs substrate, NW with the golden metal cap on its top and registration system of the AFM. The bias can be applied to the substrate or to the conductive layer AFM probe. The equivalent electrical scheme is shown later in Figure 4.4b. Here it must be noted that the scheme is valid both for spectroscopy regime (measurement of the I-V curves) and for the mapping of electric current by PeakForce TUNA mode. Both of these approaches can be successfully used for as-grown vertical NWs as shown in this thesis.

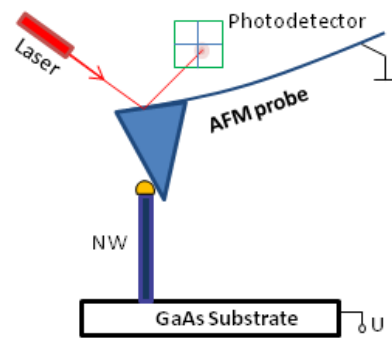


Figure 3.5 Experimental scheme for AFM measurement of NW I-V curves.

7 samples (Publication II) were fabricated in order to recognize the influence of material of passivation shell layer onto electrical properties of NWs (Table 2). This was supposed to be done through measurements of their I-V curves with highly sensitive TUNA application module and after recognizing the major challenges with C-AFM experimental protocol. NWs were grown by VLS mechanism inside MOVPE chamber (described in Publication II) also in Aalto University. Four passivating materials, i.e. GaP, InP, AlGaAs and GaN, were compared. The results of electrical measurements for both series are summarized later in Section 4.1.

Table 2. Summarized parameters of seven studied samples of passivated p-GaAs NWs from Publication II.

Sample #	Passivation material	Thickness of passivation layer	Doping level, cm ⁻³	Height of NW, μm	Color in later Figures 4.5 and 4.6
1	(unpassivated)	-	10 ¹⁹	1	black
2	GaP	~One monolayer	10 ¹⁹	1	red
3	InP	Few monolayers	10 ¹⁹	1	purple
4	GaN	One monolayer	10 ¹⁹	~0.4	green
5	AlGaAs	10 nm	10 ¹⁹	1	NW#1 blue NW#2 magenta
6	AlGaAs	30 nm	10 ¹⁹	1	orange
7	AlGaAs	~300 nm	0.5·(10 ¹⁹)	1	brown

One major methodical issue in the measurements of passivated NWs, especially with thick shells, is avoiding the direct contact between the C-AFM probe and the semiconductor shell. Otherwise, complete reconsideration of model of resistive element, i.e. equivalent scheme, is required. Moreover, charges can be accumulated during such parasitic contact. Another methodical finding was that it is necessary to access the quality of the fabricated array by the comparison of properties of both nearby standing and far standing NWs. Comparison of solely nearby NWs located in the center of the substrate can be used to compare different passivations. After it appeared possible to use the PeakForce mode to adequately visualize the NWs without the detachment of NWs (which was very common when working in Contact or Tapping modes) we decided to focus on more advanced experiments in NWs, e.g. KPFM and piezoelectrical research.

3.1.4 Microscopy of surface potential for visualization of charge accumulation in horizontal NWs

Studying the horizontally fixed NWs with the help of lithography mask (Figure 3.6) is more typical geometry of experiment (described in Publication V). Contact Potential Difference (CPD) parameter can be scanned along the single NW as the difference between the work function of probe coating material (constant) and the potential distributed along the NW (variable) (Halpern, 2012, 2015). This method is called Kelvin probe force microscopy (KPFM). It routinely allows studying the distribution of surface electric potentials. Significant advantages of this lithography-based approach is capability to utilize the macro-scale electrodes to apply electric potentials.

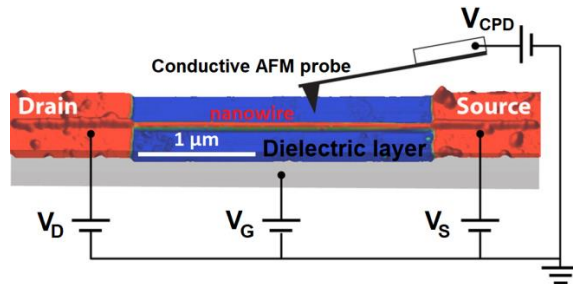


Figure 3.6 Schematics of a KPFM experimental setup with individual horizontally fixed GaAs NW. Contact Potential Difference (V_{CPD}) is measured by C-AFM probe along the horizontally lying pGaAs NW, while external bias is applied to one of the Zn/Au electrodes connected to the NW. Adapted from (Halpern, 2015).

Nevertheless, lithography approach is invasive and requires separation of the NWs from the growth substrate and further deposition onto a new substrate, which may affect some of NW properties. Moreover, electrical resistance of the lower contact NW-substrate cannot be examined because of the separation of NWs exactly at this location.

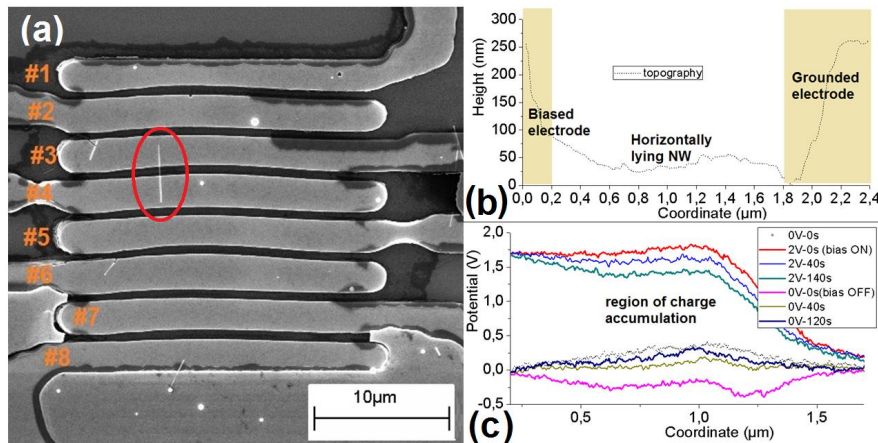


Figure 3.7 (a) SEM image of a microchip with pGaAs NW covered by Zn-Au micropads grown by optical lithography. Red mark indicates a NW circuiting the pads #3 and #4, which were used for biasing and grounding. (b) Topography profile of the horizontal pGaAs NW. (c) Surface electric potential profiles measured with different time interval for bias 2 V applied followed by 0 V applied to the left electrode, i.e. to electric micropad #3. Image taken from Publication V.

8 conductive pads produced by the photolithography are shown in Figure 3.7a, where the NW (in red oval) is connecting the pads #3 and #4. This means that application of bias between these two pads should lead to electric current flowing between them. The

experimental scheme for horizontally fixed NW is schematically shown in Figure 3.6. Figure 3.7b shows the topography height profile of the lying NW, where the golden electrodes (as they have thickness ~ 300 nm) are seen on the sides of the NW the horizontally lying on the substrate. The NW's diameter in this case was ~ 100 nm, which is not visible because topography profile indicates the relative difference in height between the NW and two nearby electrodes. Kelvin probe force microscopy of the surface electric potential can be measured for the horizontally fixed NWs as shown in Figure 3.7c. It is possible to regulate the value external bias, duration of its application and polarity, leading to recognition of position of Schottky barrier and to observe the process of charge accumulation in native oxide layer. The analysis of KPFM experiment and comparison with I-V curve data is given in Publication VI. The results of experiments related with charge accumulation in NWs are discussed in Section 4.2.

3.2 Mechanical measurements of InP NWs

Recognizing the strength and elasticity of NWs is important for manufacturing of NW-based devices, because these structures can be easily broken due to their small size. A number of works report the changes in elastic modulus for nanoscale materials (Chen, 2006; Stan, 2007; Barth, 2009; Guo, 2014; Moon, 2015), while part of their assumptions contradict to another in interpretation of experimental results. On the basis of major publications related with bending of individual NWs (Xu, 2010; Alekseev, 2012; Stan, 2012; Calahorra, 2015) and discussion about size-related elastic parameters in NWs, we wanted to clarify the situation with elastic modulus of nanomaterials by studying them in the form of NWs by the AFM method.

3 samples were fabricated in order to test the capabilities of modern QNM regime of AFM for bending of NWs (see Table 3). NWs were grown by VLS mechanism inside MOVPE chamber (described in Publications III - V) in Aalto University. Two versatile crystal phases of InP, i.e. WZ and ZB (mixed WZ/ZB), were compared in NWs with cap diameters of 10 nm and 20 nm. The analysis of the results is given in Sections 4.3 and 4.4.

Table 3. Geometrical parameters and crystal structure of tapered inclined WZ and mixed WZ/ZB InP NWs.

Sample number	Length L , μm	Middle radius R_{mid} , nm	Taper angle γ , deg	Crystal structure based on photoluminescence and TEM edX data
S1	2 - 3	15 - 25	$\sim 1^\circ$	wurtzite
S2	2 - 3	25 - 30	$\sim 1.5^\circ$	zinblende/wurtzite
S3	2 - 3	35 - 45	$\sim 1.5^\circ$	zinblende

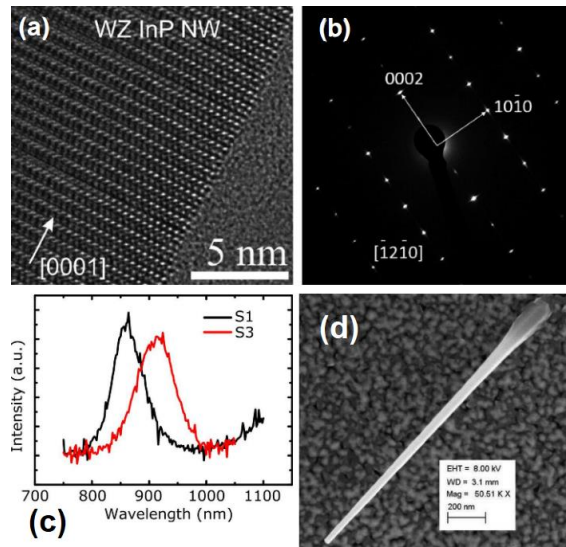


Figure 3.8 (a) HRTEM image of the end of an InP NW (S1 sample). (b) The indexed electron diffraction pattern for WZ phase InP observed in sample S3 indicating WZ structure of InP NWs. (c) Photoluminescence graphs for the samples S1 and S3. The “red” 910 nm (1.35 eV) peak corresponds to ZB InP (ZB InP band gap should be 1.344 eV), and the “black” 855 nm peak (1.45 eV) is what is expected from WZ InP. (d) High resolution SEM scans were done after the standard SEM imaging. They approved both diameters of the NWs calculated from our model and verified the cone angles.

The WZ phase of InP was verified on the basis of TEM and photoluminescence data (Figure 3.8). It appeared that the NWs had slight tapering (Figure 3.8d) instead of the ideal cylindrical shape, which was associated with the growth conditions, i.e. regime of temperature treatment, precursor flow and timing of the NW growth. Tapering of the NWs puts additional difficulty on modeling of these nano-objects, but already the successful growth of stable WZ phase InP NWs was a technological achievement in 2015. Therefore, we decided to perform the measurements on such complicated tapered WZ InP NWs in order to find the elastic modulus of the material in these NWs. Here it is worth noting that previously the Young's modulus of WZ InP has not been measured experimentally by anyone. Additionally, it was necessary to deduce the formula for characterization of mechanical properties of tapered NWs (derivation is given later in Section 4.3).

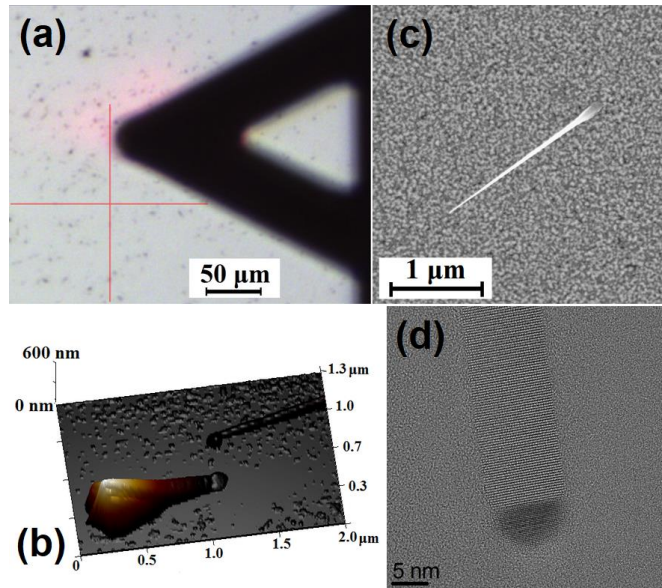


Figure 3.9 (a) Optical image of an array of InP NWs at magnification 200x with A-shaped SPM cantilever and reflection spot of scattered red laser beam. (b) 3D SPM image of inclined InP NW and a broken NW lying nearby on the substrate. (c) SEM image of inclined InP NW, where the conical shape and a lower “thick base” are distinguishable presenting the corresponding electron diffraction pattern for WZ InP phase. (d) HRTEM image of WZ InP NW near the Au cap.

3.2.1 Preliminary visualization of a sample and allocation of the inclined NWs on the substrate

The first step after the samples are grown is their visualization by SEM. SEM visualization is routinely done after the growth of NWs in order to control their quality. At the same time, we have found few practical features in SEM helping in the later mechanical property investigation of certain NWs with AFM. We have observed that the secondary electrons channel in SEM can be helpful in finding of the inclined NWs. This was achieved by finding the structures with fixed highly contrasted segment in SE followed by discovering the blurry triangular shapes of the oscillating free ends of inclined NWs in backscattered electrons channel. Capturing the SEM images with low magnification is beneficial in order to find the area with the NWs, which can later be accompanied with optical microscope images and large-scale AFM topography map of the sample.

Utilization of ordinary optical microscope is highly useful for visualization of the prepared samples, because it allows to recognize the positions of the scrapings, trenches and all other sub-millimeter scale features that can be used as reference points for further finding of the NWs. Making an image of the sample through 12.5 magnification lenses, with 1x and 4x oculars can be done in practically every laboratory.

Further, large-scale optical images for the sample can be associated with data from the video-optical visualization camera (Figures 3.9a) installed in almost all AFM devices. BRUKER Multimode 8 AFM station used in our work permits 200x magnification (depending on the size of the digital window) showing the optical images with the size of 500x375 μm . It can be highlighted that such visualization allows to observe the grey spots where the NWs are located. In fact, this methodical observation, even though not significantly interesting from the physical point of view, has significantly improved our experimental procedure. It does not seem obvious that a nanostructure with the thickness as small as 10 nm (much smaller than the wavelength of visible light) can be seen in standard optics. The reason for this noticeability lies in disturbance of light reflected from the surface of the sample. The surface of our samples was flat, represented by Si, GaAs or InP substrates. If the distance between the NWs is significantly higher than the characteristic size of the NW (which can be controlled during the growth), then the NWs will be separately standing on the substrate. Flat area of the substrate reflects the light in a regular manner, which results in a homogeneous color on the sensitive matrix of the camera. However, the NW plays the role of local disturbance for the falling/reflected light. This means that the locations where the NWs are situated will bring less amount of light to the sensitive matrix. Such areas will appear darker in the image. Moreover, considering the magnification capabilities of the video-optical camera and size of the NWs, it was partly possible to predict the size, orientation and inclination angle of the NWs based on the amount of pixels comprising the darker spots in the optical image (see Figures 3.9a). We tried to focus exactly on elongated objects, because they represented the NWs having the desired low inclination angle $\sim 20^\circ$ to the substrate. The NWs having $\sim 60^\circ$ angle to the substrate were looking shorter and were not appropriate for our mechanical study because of significant sliding of AFM probe from their upper surface and lower values of deformation for the same applied setpoint force. Further, the video-optical images could be easily correlated with the AFM topography survey images.

We were not interested in shape of NWs visualized by AFM (Figure 3.9b), because they are better presented by SEM (Figure 3.9c). AFM topography visualization of the vertical and inclined NWs makes no sense if one wants to represent the shape of the NW. Reason is that it is not possible to visualize anything below the object by AFM, while AFM tips typically have a shape of a pyramid, with symmetry axis along the long axis of the cantilever and different size of the front/back facets of the AFM tip pyramid. This is due to high influence of the tip convolution effect (see Figures 3.1a, 3.4cd, 3.9b) toward the obtained images (including 3D topography models). However, the prompt survey scans with AFM are supporting the detailed studies of electrical conductivity, I-V curves, mechanical bending experiment, observation of piezoelectric current etc. Comparison with post-growth TEM data (Figure 3.9d) of the NWs cannot assist in finding the NWs on optical image due to very high magnification. However, it helps to recognize quality and aging of the NWs, e.g. absence of the oxide shell on the surface of InP NWs presented in Figure 3.9d, which appears important later in Section 4.3.

It should be noted that very soft AFM probes should to be used for the survey scans in order to diminish the deformation in NWs. This reduces the probability of breakage of

the standing NWs and moving of the broken structures laterally along the substrate. The probes with spring constant $k < 1$ N/m, for example “ScanAsyst-Air” (BRUKER Inc., 2018), can be proposed for this purpose. It is advisable to land at the area in micrometer proximity to the desired NW. This can be done with the help of the optical microscope imaging, knowing the position of the tip end on the opposite side of the cantilever and procedure presented above. Later it is needed to make large survey scan of approximately $30 \times 30 \mu\text{m}$ with some flexible probe and low interaction force (setpoint force ~ 1 nN). Excessive setpoint force would break the NWs, while insignificant force of interaction would lead to losing of contact between the AFM probe and the areas straight after the highest points of the NWs. This so-called parachuting effect is a known artifact of AFM imaging, which can result into inability to locate the low-situated NWs near the NWs with the higher free ends. Realization of this AFM topography imaging by the entire above-mentioned protocol can allow finding of typically 3-10 NWs on the appropriate scan area of $30 \times 30 \mu\text{m}$ during 1 - 2 hours of measurement. We consider that such hour-long measurement can be recommended because it establishes the credibility of around 10 individual NWs for statistical verification of their properties.

Additional post-AFM visualization in SEM can require around 1 hour of time for fixation of the sample, establishment of the necessary numerical aperture, accelerating voltage, angle of inclination toward the detector, proper beam alignment, aperture-hole alignment, astigmatism correction etc. This would allow lateral resolution of around 5 nm in an ordinary SEM instrument, but it is necessary to consider the associated errors: methodical, instrumental, artefacts resulting from the roughness of the sample, charging etc. Such resolution is not suitable for NWs with diameters (upper parts of vertical NWs or free ends of inclined NWs) in the order of 10 - 20 nm. For the NWs with diameters bigger than 50 nm it can be appropriate to detach the NWs with the AFM probe after the AFM mechanical experiment (see lying NW in Figure 3.9b and experimental schematics in Figure 3.10). This is done in order to fix the NW horizontally on the substrate, but makes the experiment invasive and therefore not applicable for specific samples. Subtraction of the height of the NW from the surrounding area of the substrate designates the shape, i.e. height, diameters and the cone angle, for the NW with high accuracy. At the same time, local roughness of the substrate can interfere with the readings. In addition, there might be some parasitic growth on the substrate during the NW synthesis. These particles could appear under the studied horizontally fixed broken NW and lead to misinterpretation of the NW diameters. In fact, very accurate determination of diameters is essential for correct modeling of the properties of the studied NWs. Therefore, it seems favorable to use HR-SEM for the measurement of sizes of NWs (Figure 3.9d). This can produce the images with resolution around 1 - 2 nm for the inclined NWs, resulting into affordable error of the determined Young’s modulus (see the error bars for various NWs in Figure 4.13). Due to accumulated optical, video-optical, SEM and AFM topography data the localization of the desired NWs in HR-SEM seems to be rather effortless, quick and therefore inexpensive.

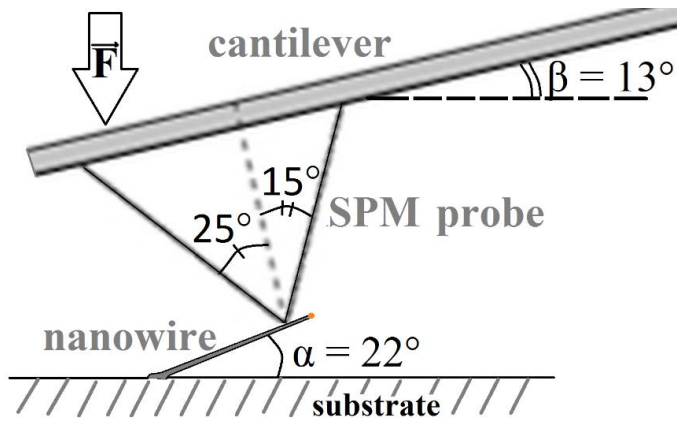


Figure 3.10 Experimental scheme reflects the realistic scale for SPM probe above inclined InP NW mounted on the wafer and corresponding angles of their contact interaction. The specified angles $\alpha \sim 22^\circ$ and $\beta = 13^\circ$ are being reduced upon increasing of the bending force F in our experiment.

3.2.2 Classical Force-Load curves method

The usual way of performing the bending of quasi-one-dimensional objects by AFM is called the method of Force-Load curves, which was presented for GaAs NWs (Alekseev, 2012). It consists of visualization of the NW topography (Figure 3.11a) and later application of definite setpoint force of push at certain coordinate on the NW (Figure 3.11b). First step is to know the distance from the base (fixation point to the substrate) to the point where the force is applied by AFM probe. Then by measuring the deformation of the NW downwards it becomes possible to calculate the stiffness of the NW knowing the force of push and own stiffness of the AFM cantilever (Röhlig, 2010; Alekseev, 2012). Increasing of the distance to fixation point would result in higher bends and lower local stiffness of the NW represented by Force-Load curves with lower inclination (Figure 3.11b). This method seems quite laborious and time consuming nowadays. Moreover, the repeatability of the measurements seems rather low.

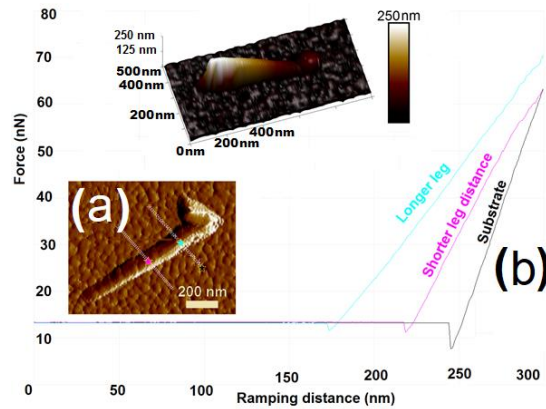


Figure 3.11 (a) Force error channel representing NW's fixed end at lower left and free end at upper right. Force spectroscopy was performed according to the coordinates seen by color marks. (b) Force-Load curves $F(z)$ for substrate, middle of NW and free end of a NW. The upper insert shows 3D topography model of an inclined InP NW representing angle 22° to silicon substrate after visualization of the NW under small setpoint force.

The following discussion presents the AFM PeakForce QNM measurement protocol for the measurement of the mechanical properties of inclined NWs in extended details. The measurement protocol developed in our work combines the tools typically available in the laboratories oriented toward fabrication of NWs while such modern research centers are usually equipped with AFM devices with force control regime equivalent to PeakForce QNM. Bruker Multimode 8 AFM was used in this work (with support of NT-MDT NTegra Aura device described in Publications VI – VII and SII). Since it is one of the most widespread AFM stations in the world and the Software for data acquisition NanoScope is also used by plenty of operators worldwide, we will here present the protocol with the parameters called in the way they are termed in the NanoScope software.

3.2.3 Detailed PeakForce QNM protocol of acquisition of the flexibility profiles for separately standing individual NWs

Primary item to be noted is that an angle of fixation of the sample on the AFM piezoelectric scanner's tube is useful to be registered. It is typically possible to recognize the major submicron or few-micrometer-level features on the surface, e.g. scrapings, dust particles and agglomerations of the NWs (see Figures 3.9a), which sometimes resemble the constellations on the substrate. Accuracy of approximately $\pm 5^\circ$ is enough to locate the sample (after the QNM calibration sample would be installed and removed) back into its initial position.

Further parametrization is done in the NanoScope software for online data acquisition. Initially it is vital to choose the probe with appropriately small spring constant, e.g. for NWs with diameters 10 - 50 nm $k \sim 0.4 - 2$ N/m; for NWs with diameters 50 - 100 nm k

~ 2 - 10 N/m. Shape of the bulk does not considerably matter, although various shapes of cantilevers can have different tendencies for torsional rotation. The probe is installed into regular probe holder. Standard calibration of the laser is recommended to be supported with fine calibration. Fine calibration lies in maximization of Amplitude of induced oscillations from the resonant Tapping contour. This is preferential instead of maximization of SUM intensity of the laser for highest sensitivity of the measurements. Utilization of the advanced calibration protocol allows observing the proper shape of the resonant contour in the bandwidth displaying the appropriateness/freshness of the probe. Adequacy of the Q factor, thermal contour location and shape and adequacy of value of Drive Amplitude electrically inducing the probe oscillations (should be around 5 - 50 mV and not changing significantly after hours and days of the measurement) for reaching the normal value of 0.5 V of AFM feedback laser's repositioning amplitude as a spot falling onto the 4 quadrant AFM's photodetector.

Engage setpoint should be decreased in Engage Settings from 0.15 V presetted by default to ~0.05 V, in order to protect the tip's apex from damaging already at the moment of the engage/landing. In fact, blunt probes are not the problem for mechanical measurements (as will be shown later), although adequate regularity in the measurement procedure must be kept. Moreover, damaging of the probe can spoil the electrical measurements because the conductive coating would be teared away and the AFM probe conductivity would be affected.

All measurement settings need to be permitted for change in the Experiment category (while they are preliminary locked). The Show all function realizes the control of Sync Distance and Sync Distance QNM features that are important for establishment of proper parameters for topography measurements on area with high concentration of NWs on the substrate. In addition, we have observed that Sync Distance, i.e. the moment when the PeakForce is recorded having the highest value of force during one cycle, is affected by the setpoint force and is not measuring the correct time moment for the bendable objects like our NWs. This is because additional time is needed to bend the top parts of the NW in comparison to the segment near the base, while the Sync Distance is fixed for the entire scan image. Unfortunately, we were ought to neglect this deviation and did not study its influence in details. It is possible to suggest that Data capturing feature may be used in order to record all the datapoints of the scan (500 points per cycle (see Figure 2.10), 2000 cycles per second, each optimized scan take around 21 minutes). Later it is possible to process the locations of the NWs separately in MatLab to recognize the correct values of the setpoint forces applied in certain locations, which can be a part of further detailed investigation.

All measurements were sampled at 2 kHz PeakForce frequency (2000 cycles of taps per second), since the default 4 kHz sound produced by AFM scanner tube felt intolerable for long-term work with the AFM equipment. Moreover, shorter cycles of PeakForce tap result in shorter time of the contact and are appropriate for fast scanning rather than accurate measurements.

Data channels should include both “Height” and “PeakForce” turned on in both directions of recording (trace and retrace). “Deformation”, “PeakForce error”, “Adhesion”, “Dissipation” and “DMTmodulus” can be also switched on (see Figure 3.12) since Multimode allows acquisition of 8 channels of data simultaneously from one and every line of the scanning. This can support the comparison of channels, e.g. ”Height” can help in recognizing direction of growth of the NW, and both directions switched on would indicate problems associated with parachuting, breakage, slippage and other parasitic phenomena that often emerge during scanning of flexible 1D structures.

Automatic configuration of all parameters except the setpoint force should be turned on. Setpoint is supposed to be adjusted manually to capture data of inclination under different load forces. We used the following sequence of setpoint forces in our experiments with inclined InP NWs: 0.1; 0.2; 0.5; 1; 2; 5; 10; 20; 50; 100 nN. Typically, forces from 0.5 nN until 20 nN were the most informative (Figures 3.13b and 4.12d) for our study of NWs with micrometer length and 10-20 nm diameters of free ends.

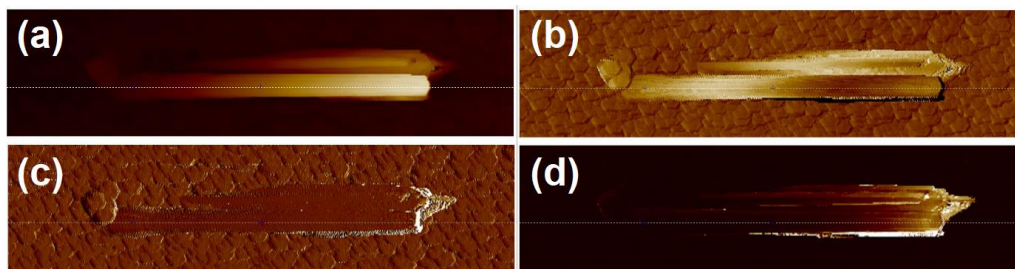


Figure 3.12 SPM images of inclined InP NW, with NW base on the left. Image sizes are $3 \times 0.75 \mu\text{m}$. Comparison of data from PeakForce mode channels used to quantify the elasticity: (a) Topography, (b) PeakForce, (c) PeakForce Error and (d) Deformation. PeakForce setpoint was normalized to 0.2 nN.

“Realtime RT” and “offline OL” plane fitting need to be switched off. This is an absolute requirement for “OL” plane fit, and important note because this parameter is turned on by default in Bruker's software NanoScope. The latter analysis of the “Height” and “PeakForce” data will be done with the raw data and it must not be fitted or altered in any possible way.

It seems optimal if the size and position of the video-optical window in Undock mode will be permanent during the scan. This considerably simplifies the post-imaging analysis, because the collection of screenshots taken during the scanning is in fact a detailed lab journal of a scientific experiment. It does not seem feasible and adequate to write plenty of the parameters changing during the AFM experiments, so luckily saving of screenshots (e.g. via Dropbox) seems helpful. Thermal drift of the sample can occur in non-equilibrium room conditions, similarly with shift of the position of the laser on the cantilever. Additionally, thermal expansion of the AFM parts after extensive operation was found to change the position of the laser beam. Thus, AFM feedback system

calibration would be enhanced, if the fine fitting would be performed once more after approximately half an hour from the beginning of the experiment.

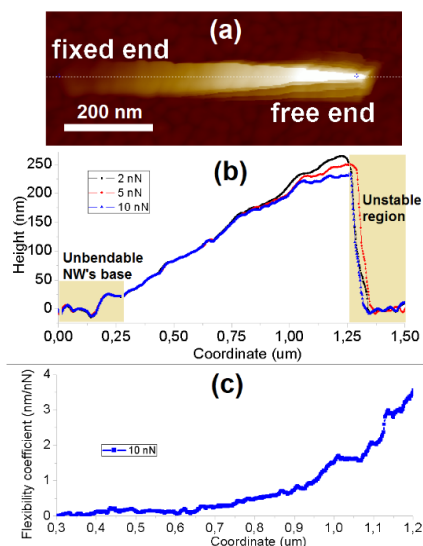


Figure 3.13 (a) High resolution rectangular shaped 2D topography image of an inclined InP NW under significant force setpoint 10 nN. (b) Comparison of topography profiles for bending of inclined InP NW under different forces. (c) Bending profile representing flexibility spectra of a single bendable NW along its length, where fixed end is on left and free end is on right side.

During the abovementioned parametrization and establishment of the temperature equilibrium (which takes 10 - 30 minutes), it is possible to perform the survey scan of the sample. After that, the sample is replaced by the special hard test calibration sample, which is normally sapphire with elastic modulus ~ 345 GPa. This test sample is used to calibrate the Deflection (DFL) sensitivity. The DFL sensitivity value is found from the inclination of probe-sample force curve taken in Ramp mode, and is typically within the range of 10 - 60 nm/V. The higher value indicates the higher flexibility of the chosen AFM cantilever. Standard requirements are specified in software Help, so no exhaustive details will be provided here except one practical detail related with the PF deflection sensitivity. It is needed to evaluate PF sensitivity with update sensitivity in PeakForce Monitor, while “Autoconfig” function for the PeakForce curve is done beforehand. “Autoconfig” corrects the shape/background of the PeakForce curve array, and establishes the proper time of consideration of the PeakForce time moment. This seem to work fine with flat surfaces, but not with bendable structures. Some discrepancy of the PF sensitivity can be observed, when the PeakForce setpoint value is changed, so that Ramp sensitivity and PF sensitivity were found equal only for comparatively narrow range of PeakForce setpoints (typically within 1 - 10 nN). Along with that, importance of the PeakForce amplitude was not fully understood, because it could affect the established value of PF sensitivity. Visualization of the standing NWs requires large PF amplitudes,

while accurate acquisition of PF setpoint force requires low PF amplitude. We used the PF amplitude 150 nm for our experiments.

The Thermal tune feature allowed to calibrate the spring constant of the probe. The procedure is standard and described in Help. It is needed to consider the surrounding ambient air or other media, where the bending takes place. Here it seems important to add only that the spring constant value can vary in time, so the digits after the second decimal point of the spring constant can be disregarded as part of the systematic error of the method. Furthermore, the normal spring constant value depends on the temperature as known from the Sader's method (Sader, 1999), while temperature can experience some change during the time of scanning. Heating of the cantilever and associated changes in its thermal/electrical conductance were neglected. Still, even though one or few parameters can be neglected, the combination of all parameters can appear important for consideration, so they are either mentioned or described in details in this thesis. Last step of QNM calibration is evaluation of the AFM tip radius, but it is unnecessary, since the radius only quantifies channels of elastic modulus, adhesion and dissipation that will not be useful.

The standardized calibration sample is replaced by the desired one, with consideration of the previously observed angle of fixation. It seems rather simple to repeat the position of the sample manually with accuracy of few degrees (as stated above) to foster the processing of images. Recognition of features on the topography image taken after placing the studied sample back onto the scanner helps to allocate the NWs of interest during few minutes.

The actual experiment takes place after the above-described calibration. The scan area is decreased to the size comparable with the projection of length of the NW (Figures 3.12, 3.13a, 3.14b and 4.12b) and fast survey scan is done to evaluate the angle of tilt of the NW to the fast scanning axis (horizontal axis) of the AFM image. This angle is set into the "Scan angle", so that the long axis of a NW would be fixed as parallel as possible to the AFM's fast scanning direction. A paramount detail here is that it is optimal to choose the NWs that are initially oriented directly toward the AFM cantilever (like in the schematics in Figures 3.10 and 3.14a), or are fixed with small angle toward the AFM cantilever. Angle of projections of the NWs to the substrate is defined from crystallographic data and can be foreknown on the basis of SEM or optical images. Establishment of low angle between the NW's projection to the substrate and cantilever's projection (they both should be situated in the same plane with the axis and projections of the bent NWs and cantilever's vertical movement) can result in optimal compensation of the AFM cantilever angle and NW's angle to the substrate, so that sliding of the probe from the NW will be minimized. Furthermore, it is possible to increase the discretization of fast scanning X horizontal axis (see Figure 3.14b) of fast scanning to few hundreds of pixels. We used 1024 pixels for the experiment with WZ InP NWs (Publications III-V) with no additional time spent on the measurements, while error associated with averaging of the PeakForce mode data along the scan line could be just slightly worsened. Bigger amount of datapoints results in a wider statistics of the bending along the studied structure, thus strengthening the repeatability of the measurements.

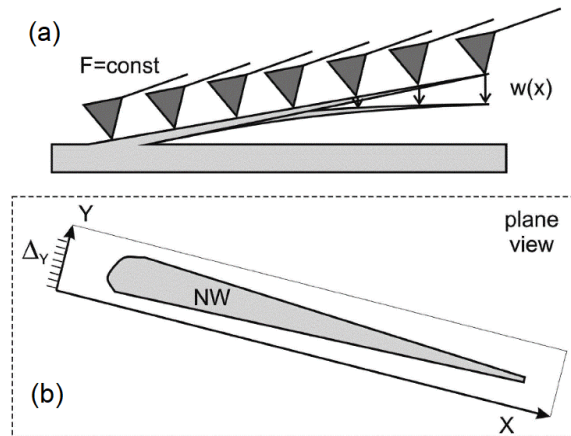


Figure 3.14 (a) Scheme of SPM bending profile measurement. (b) Orientation of SPM X-axis relating to the long axis of the NW.

Later on, the amount of lines (amount of pixels per slow scanning AFM direction is shown as Δy in Figure 3.14) is put in such a way, that distance between the scan lines (Y-width of the pixel) must be significantly less than the diameter of the NW. Otherwise, slipping of the probe from the spine of the NW would take place. Moreover, the length of the profile could be decreased and free end of the NW could appear not measured at all (see sharpening in the right part of the NW in Figure 3.13a), which is a prominent problem for bends measured with the large PeakForce (setpoint force) values. This drawback is associated with the quantization of the angle of scanning as full digits (in Bruker NanoScope software). The ultimate goal of this combination of rotation of angle and pixel establishment is acquisition of long low-noise bending profile along the full length of the NW. In addition, it can be proposed to rotate the sample itself, so that the studied NW would be oriented toward the cantilever. Unfortunately, this rotation of the sample on the sample stage is not realized in Multimode 8 AFM and requires manual rotation of the entire sample on the scanner. However, this feature can be found in other microscopes or introduced in later advanced sample stages/holders. The aspect ratio can be increased to 4-16 (aspect ratio for Figure 3.12 is equal to 4) so that amount of lines of the scan and corresponding duration of the measurement will be shortened respectively with the aspect ratio value. This does not affect the informative data, but only eliminates the nearby areas of the substrate that are uninformative. The scan rate should be decreased as much as possible, e.g. until 0.1 Hz as the minimal default value, but it can be decreased even lower in the advanced settings of calibration feature in the NanoScope software. The slower the scan will go along the NW, the better will be the representation of each pixels data of the Height/PeakForce pair and associated bends.

Bends are accounted as “Height” for the lowest force after deduction by Height in desired force, but not taken from the “Deformation” channel. The “Height” observed under the smallest force is admitted as the real height, while in fact all AFM measurement always

show the topography of the deformed structure. Scanning is preferably to be taken always either from up-to down, or down-up of the scan, to reduce additional torsional movement and eliminate parasitic sample drift inputs to the measurement error. Finally, if all the resultant profiles of NWs are oriented in the same direction (bottom on the left like in Figures 3.9, 3.10a and scheme in 3.14b), then analysis of data do not require 180° rotation each time and processing the numerical data becomes faster.

It seems optimal to start from the smallest setpoint forces to eliminate possibility of non-elastic regime of bending and damaging of the studied NW. In the course of AFM topography images it will be visible how the NW becomes visualized slimmer and shorter with increase of the setpoint force (see Figure 3.13ab). This effect is mainly due to torsional bends of the NW, partly due to the slippage of the probe from the NW surface and slightly due to the torsional bends of the probe. Nonetheless, it should be possible to acquire a few hundred nanometer long profile along the NW, with few hundred of “Height”/“PeakForce” pairs of data values for $k(x)$ stiffness profiles and their further analysis.

3.2.4 Processing of the experimental QNM-based bending data for NWs

The results of processing of the results recorded for real samples of InP NWs are presented in Section 4.3 of this thesis. The data files were analyzed in the following way. From the eight channels of recorded data we considered the channels of “Height” and “Deformation”. We took channels recorded in trace direction because NWs had stable base segments in the left side and the deviation of position of AFM probe is the smallest there, so beginning of the profile recording from stable part was found to be preferential.

The values of Height measured under the low scanning setpoint force are subtracted by the Height in the desired force (see Figure 3.13b) and divided by the known PeakForce value. This produces a stiffness profile, while its inversed values give flexibility profile (see Figures 3.13c and 4.12e). It seems better to utilize the flexibility profile, since it does not go to infinity near the fixed end of the NW. This allows fitting of the data values in numerical calculation software like Origin, Excel or MatLab. We produced an original Origin script that was written for the NW flexibility profile analysis.

Averaging of the data was done so that few flexibility profiles were normalized into one representing the structures elastic property under the force 1 nN (see bends in Figure 4.12d and corresponding averaged flexibility profile in Figure 4.12e). It was necessary to determine and use the analytical solution governing the measurable parameters of a tapered beam with properties of the material and applied impact formulated in a formula or system of equations. This equation was determined and can be used for NWs in its universal form (4.3.37). The procedure of fitting the values was done for the averaged profile in Origin software with the “non-linear fitting” feature according to the equation (4.3.35) in later Section 4.3. Analysis of the auto-fitting parameters resulted in establishment of the Young's modulus for the NW. Thus, 4-6 flexibility profiles for different forces containing ~300 datapoints were averaged into one profile, then auto-

fitted by the formula (4.3.35) (see Section 4.3) for tapered beam and resulted in one value of the Young's modulus of material in the studied NW. These values for different NWs from the studied samples were combined and are presented in Figure 4.13. This figure indicates the difference in elasticity for the material in studied NWs, but the effect does not seem to be related with size of the material as it is described for certain nanomaterials in the literature. Explanation will be given in the sections 4.3 and 4.4 where the results of various approaches are compared.

3.2.5 Assumptions of the applied theory and limitations of our model

Must be noted that it is vital to consider not only the generalized form of relation between variables in equation defining the model properties with the experimentally measured parameters, but it is compulsory to consider the assumptions of the model. This of course seems valid for appropriate application of any model and defines the limits of the model's usage. The four fundamental assumptions of Euler-Bernoulli beam theory were specified in Section 2.5. Two additional assumptions for the model of our physical beam in Euler-Bernoulli beam theory are (1) isotropy of NW's material and (2) elastic regime of bending. Material of a NW is considered isotropic along the entire length of a NW ($E_{mat} \neq E_{mat}(x)$), discarding e.g. surface effects, possible defects in crystal structure, absence of the oxide shell affecting the resulting elasticity etc. In reality, possible defects act as deformation accelerators and result into the spikes that appear visible in the experimental bending profiles. Elastic regime of bending means that the object's deformation should be very small ($\omega \rightarrow 0$) even under the highest Setpoint force applied for the deformation of a NW. Actually, all bending forces in elastic regime must lead to same normalized stiffness profiles for certain NW ($k(x) \neq k(x, F)$).

In addition to these two additional assumptions of the model, we considered three practical assumptions related with the experimental setup. (1) The first was that Young's modulus is independent from temperature ($E_{mat} \neq E_{mat}(T)$), while equivalently no temperature change was during the experiment and no heat was generated due to the bending and applied work. (2) Secondly, was that the modulus is independent from the speed of bending in our model ($\omega \neq \omega(\text{time})$), which is correct in the limited range of applied impacts. The speed of bending is associated with the local deformation, which is dependent from the distance to the base, and no local indentation was affecting the bending profile of the structure. In addition, it is linked to viscosity of the environment, where the bending takes place and viscosity of air was neglected. (3) Thirdly, as it was mentioned earlier, we considered absence of bending ($\omega_{F \approx 0} = 0$) for the smallest Setpoint force used to evaluate the topography of the NW.

3.2.6 Core-shell model for semiconductor NWs

It can be separately mentioned that NWs can be considered not as isotropic, but complex core-shell structures. In such arrangement, an oxide or other compound covers the inner material of the core. Since properties of the two materials can be different, then

characterization of such a complex model require consideration of both, making the model somewhat complicated. It can appear that the surface layer of NW is harder than the inner material ($E_{shell} > E_{core}$) (Wang, 2017). In addition, for thin structures, e.g. thin NWs, the shell made of the native oxide can be thicker than the core done from, e.g. GaAs. Thus, a NW that is still called GaAs NW is in fact mostly done from native oxide. In both cases, defining the strength of the NW can require characterization of the shell's dominating input to the elasticity of a NW. Description of the core-shell NW is done in the frame of core-shell model presented previously for ZnO (Chen, 2006). Recognizing the influence of the shell onto NWs can have paramount importance for practice, so its thickness R_{shell} should be controlled, e.g. with help of TEM. If parameters of the shell and core are known, then dependence of the elastic modulus of the composite material in the NW is described by the formula (Chen, 2006) presented Publication V:

$$E_{mat} = E_{core} \left(1 + 8 \frac{E_{shell} - E_{core}}{E_{core}} \left(\frac{R_{shell}}{R} - \frac{3R_{shell}^2}{4R^2} + \frac{R_{shell}^3}{2R^3} - \frac{R_{shell}^4}{8R^4} \right) \right) \quad (3.2.1)$$

where R_{shell} is thickness of the surface shell layer and R is the radius of a NW.

The experimental results of three-point bending of silicon NWs studied by AFM were well described within the core-shell model of NWs (Calahorra, 2015). Therefore, we performed modeling of our experimental results in Section 4.3 to check the validity of core-shell model for our structures.

3.2.7 Proposed methodical development with a sickle-shaped AFM probe for bending of NWs

As a further proposal mentioned in Publication V, double-apex probes (Figure 3.15) can be manufactured with Focused Ion Beam (FIB) milling technique. Such AFM probes are not expensive in production. Important feature is that they have a sickled-shape ending of the AFM tip. This means that such tips are dull in the part directly touching the NWs, so that their sickled area is expected to catch and stabilize the measurements of thin NWs, can allow the measurements of ultra-long NWs and also might allow measurements of NWs standing in angles toward the substrate much more than 20° .

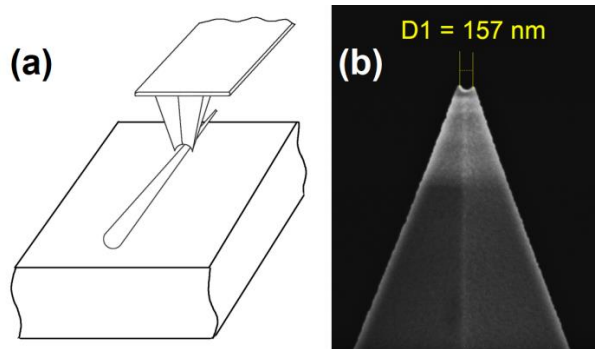


Figure 3.15 (a) Schematics of the experiment with the double-apex tip (Bespalova, 2018) and (b) SEM image of the FIB-cut SCM-PIT tip with the milled area slightly bigger than diameter of the NW that was fabricated for pilot AFM experiment.

We performed the preliminary experiments with such probes with supervised MSc student K.Bespalova (Bespalova, 2018), which resulted into MSc thesis demonstrating pros and cons of such approach. It has shown possibility to fix the small NWs in the FIB-cut area. Here we present only the concept with schematical representation of the AFM-NW arrangement and experimental SEM image of the obtained probe. However, at the same time NWs could be trapped in the cut area of the probe. After few cycles of survey scanning one of the NWs become broken and strongly attached to the probe. This lead to complete inability to use this spoiled probe.

3.3 Piezoelectric measurements of GaAs NWs

At last, we decided to utilize the experience gained from electrical and mechanical studies for AFM-based electro-mechanical experiment with NWs. Few prominent approaches from research papers (Wang, 2006; Lysak, 2016; Calahorra, 2017) describing the measurements of piezo effects in NWs seemed permitting the study of piezoelectric response in rather exotic WZ crystal phase of GaAs. The combination of optoelectronic advantages of GaAs with piezo-response of not well studied WZ structure of GaAs and local AFM-based method seemed motivating interplay of novel material and technique.

3.3.1 Mapping of piezo-electric current from a sample with NWs

Similarly with electrical and mechanical measurements, electro-mechanical (i.e. piezo) measurements can be carried out using the mapping approach and spectroscopy approach. Preliminary experiments with mapping of piezo-current generated due to mechanical deformation of NWs was shown in Publication V. However, the fabricated NWs were easily breakable during the routing survey scans carried out by a protocol similar to one presented in Section 3.2.1. It appeared that the “stumps” are left standing on the substrate after the longest segment of NWs are detached. Their height was in the order between tens and hundreds of nm, i.e. much smaller than few micrometer tall as-grown NWs. The

electric current output was registered at locations of the stumps, i.e. old locations of the standing vertical NWs, as can be seen from the Figure 3.16.

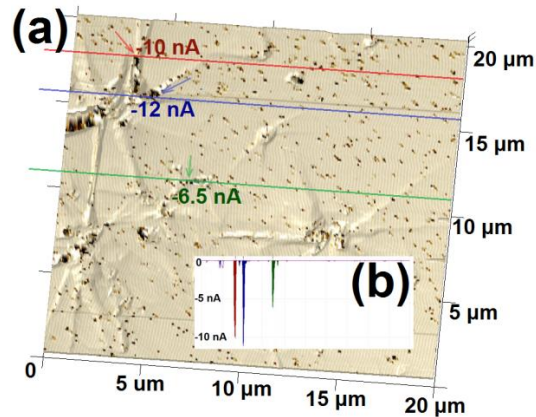


Figure 3.16 Piezo-current mapping for the sample with NW stumps.

Nevertheless, it was decided to skip this direction of mapping experiments and focus on studies of individual structures in current-generation regime. Firstly, because the NWs were broken during such mapping, while we tried to present the methods of noninvasive research. Secondly, the stumps left after the detaching of the upper segment had rather irregular shapes and height distribution. Therefore, recognizing the quantitative values from such sample seemed rather problematic. Moreover, the control of crystal quality in them could be rather complicated.

3.3.2 Piezo-induced current measurements of vertical wurtzite NWs

Typical AFM experiments previously reported for ZnO (Lu, 2009), CdSe (Zhou, 2012) and other NWs presented the concept of voltage measurement, i.e. recording of the piezo-induced electric potential. In our experiment, we registered the current generated during the bending of the NWs. In fact, the bending took place when the NWs were scanned in the constant Z-height mode, when the distance Z between the substrate and the trajectory of the AFM probe movement is kept constant. This regime is more simple than constant force mode, although it can demonstrate the phenomena and relative difference of piezo-induced current from the NWs for the different scanning heights Z.

2 samples of vertical NWs were fabricated on a Si(111) substrate with golden colloid nanoparticles having diameters around 20 nm by VLS mechanism in MBE chamber in Academic University in St.Petersburg, Russia (described in Publication VII and S2). The series was grown test the idea of piezo response arising from WZ phase in GaAs NWs. First sample was without AlGaAs passivation and did not indicate any electric output.

The Be-doped sample with 7 nm thick AlGaAs passivation shell (not reaching the metal cap) was analyzed in Publication VII.

Resulting height of the NWs was $\sim 6 \mu\text{m}$ and diameters were $\sim 100 \text{ nm}$. Post-fabrication microscopy and spectroscopy data for the samples is shown in Figure 3.17. WZ crystal structure was confirmed by the TEM data. For the correct AFM-based measurement, it was very significant that the AlGaAs shell would be grown in such way that it will not touch the metal cap on top of the NW. This is required to guarantee that that no short-circuiting of the opposite sidewalls will occur via the cap.

The AFM-based piezo-current measurements of the WZ GaAs NWs samples were initially performed on Bruker Multimode 8 AFM with conductive probes PFTUNA in room environment. These measurements have shown electric output of very small level. Later the experiment was carried out on NT-MDT NTegra Aura AFM with conductive probes HA_FM/W2C+ also in room environment. The probes used by NTegra Aura were significantly more stiff than those used for the first pilot experiment. Moreover, they were much stiffer than the NWs under the study. The measurements on NTegra Aura device have indicated a highly positive result, which was due to capability of turning the illumination laser off, which is not freely available on Bruker Multimode 8.

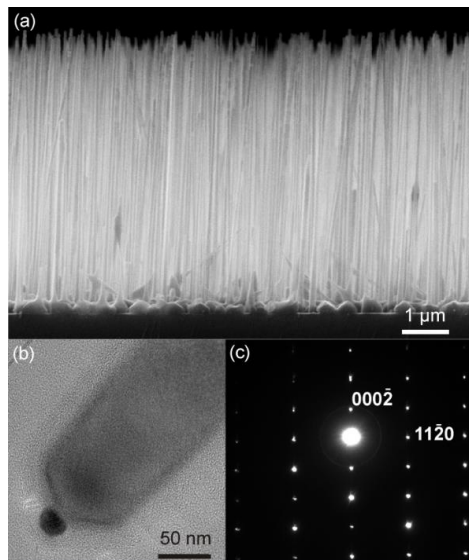


Figure 3.17 (a) SEM image of an array of vertical as-grown GaAs NWs. (b) Exemplary TEM image of an individual GaAs NW with Au cap visible as dark object at down-left. (c) Electron diffraction pattern of an individual WZ GaAs NW.

The current was measured by the built-in current amplifier with sensitivity $\sim 50 \text{ fA}$. Decreasing the Z distance between the scanning plane and the substrate caused bending

of the NWs by the AFM tip. The scheme of the experimental setup is shown in Figure 3.18ab. Motion from left to right is designated with blue, while movement from right to left is shown with red. It is visible that the current is being registered for both cases representing the repeatability of the piezo-generated current.

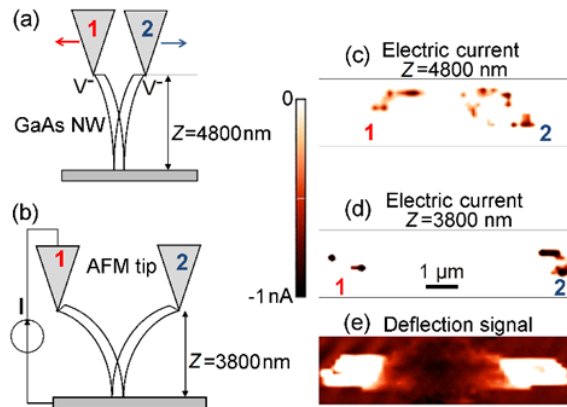


Figure 3.18 (a), (b) Schematic illustrations of the experimental setup. (c), (d) Electrical current maps for the same NW obtained for tip–substrate distance $Z = 4800$ nm (c) and $Z = 3800$ nm (d). (e) Combined AFM image presenting deflection of the NW to both left and right from the centre for $Z = 4800$ nm. “1” and “2” are the right-to-left and left-to-right directions of AFM probe movements, respectively. Electric current maps were obtained under illumination by the AFM registration system’s laser and the values at each pixel in (c) and (d) were averaged over a measuring time of 4 ms.

The locations of the measured current were combined in the Figure 3.14cd representing that a short-circuit current emerges solely when the AFM tip contacts the compressed side of the NW. Further, it was possible to see that decrease of the Z distance leads to a visible raise of the current on the electric current maps. At the same time, distance between the current spots has increased, verifying the idea about deflection of the NWs as a source of higher internal stress and elevated current. The combined DFL channel for the Z distance 3800 nm (which was less than the height of these NWs ~ 6000 nm) is shown in Figure 3.14e. The results are summarized in Section 4.5.

4 Results

All results of the Doctoral study are summarized in this chapter. Experimentally measured I-V curve spectroscopy results and conductive AFM mapping are compared for various vertical ZB GaAs NWs in Section 4.1. Computational model of electrical properties will be presented for studies of ZB GaAs NWs in vertical and horizontal geometries and compared with experimental KPFM data and I-V curves in Section 4.2. Derivation of the formula for analysis of bending parameters of the WZ InP NWs will be followed by application of this analytical formulation to experimentally measured flexibility profiles in tapered inclined WZ InP NWs. This permitted analyzing the experimental dependence of moduli in NWs from the NW diameter (i.e. crystal phase composition) and comparing it with the corresponding values of Young's moduli determined from the numerical model for core-shell NWs in Section 4.3. These results are also supported by determination of the elastic coefficients by the numerical R.M.Martin's method and comparison with the Young's modulus calculated based on these elastic coefficients in Section 4.4. Last Section 4.5 presents the results of an experiment combining both electrical and mechanical properties of vertical WZ GaAs NWs, followed by the discussion about combined piezo-phototronic effect allowing useful electric power generation in the NWs.

4.1 Analysis of experimental I-V curves for vertical nanowires

The first successful I-V curves that were recorded in PeakForce mode with the help of C-AFM. I-V curves for the vertical NWs from series described in Table I were visualized and analyzed in Publication I. Variation of NW parameters was studied by comparison of shape and inclination of the I-V curve branches. The I-V plots closest to the vertical axis with the steepest inclination of the linear region were chosen in each sample. Distinctive characteristics of individual NWs were typically almost equal with a variation of inclination of the branches less than 10%. The repeatability of these plots was approved by 2 - 3 repeatable cycles of I-V curve recording on the same NWs (in direction of increasing and decreasing the voltage) and verified for 3 - 7 NWs in each sample. Repeatable I-V curves data were assembled from a substantial amount of measured datapoints (i.e. each curve consists from 512 measurements) showing insignificant noise (noise can be visible in Figure 3.3c, 4.8 and 4.9). Therefore, the curves in Figures 4.1, 4.2, 4.5 and 4.6 (from Publications I and II) represent the most conductive NWs in each sample. The graphical dependencies are presented for indication of the influence of following parameters: SOG (red and black curves in Figures 4.1 and 4.2), passivation (images (a) and (b) in Figures 4.1 and 4.2) and substrate doping (comparison of Figures 4.1 and 4.2), passivation material (Figure 4.5) and passivation thickness (Figure 4.6).

The shape of I-V curves resembled the typical rectifying characteristics of a diode. Such shape was previously reported for GaAs diodes (Ellis, 2000) and particularly for lithography-prepared semiconductor NW samples (Talin, 2010). The shape of the curves is explained by rectifying contact related with the Schottky barrier between the metal cap and the semiconductor part of a NW or/and with the p-n junction between a p-doped NW and an n-doped substrate. The linear Ohmic region for specific curves is defined in terms

of thermionic emission theory and relates with impurity-based conduction of a semiconductor.

I-V curves shown in Figure 4.1 were recorded to compare the influence of spin-on-glass (SOG) coating toward the conductance of vertical micrometer long NWs. Moreover, we noticed the difference in shape of the characteristics depending on the length of the NWs and their passivation, which was studied later in Publication II. Here we also revealed that the limits for the C-AFM lowest resistivity that can be measured are lower than $7 \text{ k}\Omega$. This is because the NW with resistance around $R_{NW} \sim 7 \text{ k}\Omega$ was measured as inclination of the black curve in Figure 4.1b.

The SOG coating lead to increase of current for non-passivated NWs, while it was found to reduce the current in GaP passivated GaAs NWs (Figure 4.1b). The red curve in Figure 4.1bc seems visually linear for the presented range of electric current, while its “inclination” is lower than for the almost vertical black curve. The value of mobility found from the black curve resembles the expectations drawn from the consideration of the NW growth conditions by MOVPE technique.

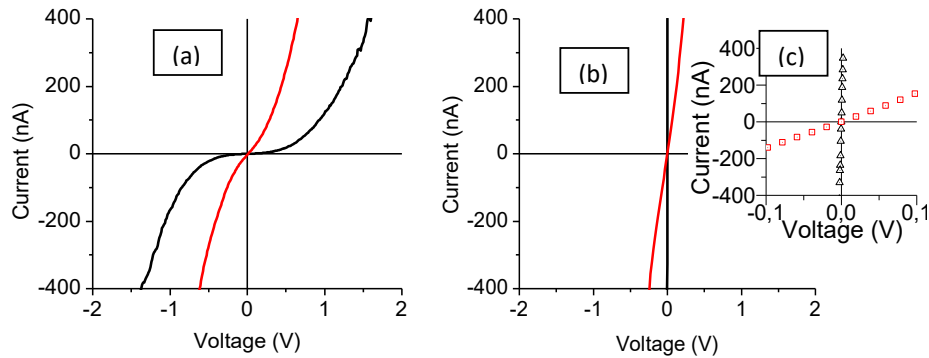


Figure 4.1 I-V curves of GaAs NWs grown on p-substrate: uncoated (black) and coated (red) by SiO_x layer for (a) unpassivated and (b) passivated samples. (c) Detailed inset of image (b).

The studies of the same p-type doped GaAs NWs grown on the n-substrate allowed comparison of different substrates and visualize the difference in I-V curve shape. It is clear that the characteristics in Figure 4.2 present a diode shape instead of the linear Ohmic resistance shown in black curve in Figures 4.1bc. Moreover, the energy barrier formed by the pn-junction between the pNW and n-substrate enlarges the threshold voltage needed to open the Schottky or pn-barrier. Different directions of sweeping, i.e. alteration of applied bias, lead to observation of hystereses on I-V curves (see the combination of blue and black curves in Figure 4.2). This was explained by major carriers trapping on the surface states of p-doped NW and was studied in Publication IV. Comparison of Figures 4.2a and 4.2b shows that application of SOG is rational for non-passivated NWs, while no significant changes were registered for passivated GaAs NWs.

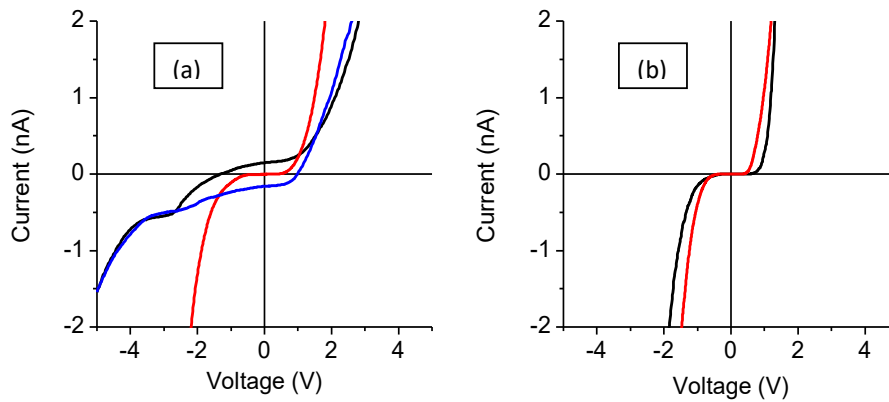


Figure 4.2 I-V curves of the GaAs NWs grown on n-substrate: uncoated (black/blue) and coated (red) by SiO_x layer for (a) unpassivated and (b) passivated samples. Black/blue curves indicate current during increasing/decreasing of the input voltage for uncoated NWs.

The inclination of the linear segments of I-V curves (their linearity were confirmed based on logarithmic plots) leads to calculation of electrical resistance of certain individual NWs. After their diameter and length are identified on the basis of SEM data, it becomes possible to calculate the mobility of major carriers in NW based on growth parameters related with doping level using equation (4.1.2). Deviation of the calculated value of resistance and resulting error in the value of mobility were noted, but the mobility correlated with the values expected from fabrication conditions and literature. Considering the variation in fabrication parameters, this irregularity in resistance is believed to be related with a variation of structural properties of certain individual NWs in each sample. In other words, we believe that the curves are slightly different because of not completely optimized fabrication conditions of nearby standing NWs, but not due to the AFM measurement error.

In relation to the fabrication step, we consider that the NWs possessed difference in diameters and doping levels, thicknesses of passivation layers and diameters of the metal cap etc. This means that it is necessary to improve the fabrication quality of the NWs and this quality can be accessed by C-AFM. Primarily, the fabrication developments are important for the future NW-based devices, where the industrial level of repeatability is required. Secondly, equality of parameters of structures is important for the correct I-V curve measurements, including the studies of NWs on a substrate connected with horizontal lithography patterns, horizontal NWs in a bridge-like geometry, for vertical standing NWs by SEM-multiprobe or C-AFM. C-AFM combines direct electrical measurement without detaching of NWs, wide availability of stations and simplicity of experiment, if PeakForce or analogous regime is used.

As mentioned above, the second possible systematic error could be AFM-related. Deviation in I-V curves could result from instability of electrical contact with C-AFM

probe. However, this possibility was neglected for our NW samples due to the almost identical shape of I-V curves repeatedly measured for the same NW.

Same measurement technique as performed for the series of GaAs NW samples with different passivation coatings summarized in Table 2. Their typical shapes are compared in Figure 4.3 where SEM images reveal the hexagonal shape of the surface of NWs, the upper cap is visible and a very thick passivation coating can be seen from comparison of Figures 4.3b and 4.3c. Typically, the diameters of the metal caps were similar to the NW diameters, although the influence of the difference between these two parameters (Lord, 2015) was not considered by us in details. Figure 4.3e represents the shape of the NW, which appears due to the convolution of applied pyramidal tip at the end of AFM probe and cylindrical vertically standing GaAs NW.

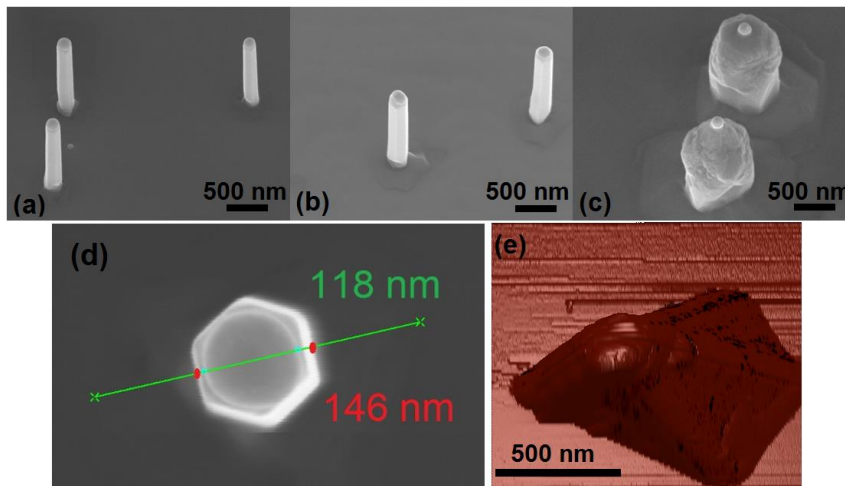


Figure 4.3 SEM images of p-GaAs NWs covered with shell layers of AlGaAs passivation with thickness: (a) 10 nm, (b) 30 nm and (c) 300 nm. (d) Top view SEM image of cross-sectional profile of covered by 10 nm thick AlGaAs passivation (designated #5 in later Figures 4.5 and 4.6). (e) The overlay of C-AFM conductivity map with black spots onto 3D topography for arbitrary single NW covered by 10 nm thick AlGaAs passivation.

It was found that the proper acquisition of I-V curves can be done using certain facets of the AFM tips pyramid. This feature is associated with the thickness of the coating and its capability to be ripened off. Additionally, it appeared necessary to consider the geometry (Figure 4.4a) of probe-NW contact, because the force of interaction (related with stability of this contact) is different for probes with different shapes and for different facets of the tip pyramids. Equivalent electrical scheme of the experimental setup was formulated and is presented in Figure 4.4b.

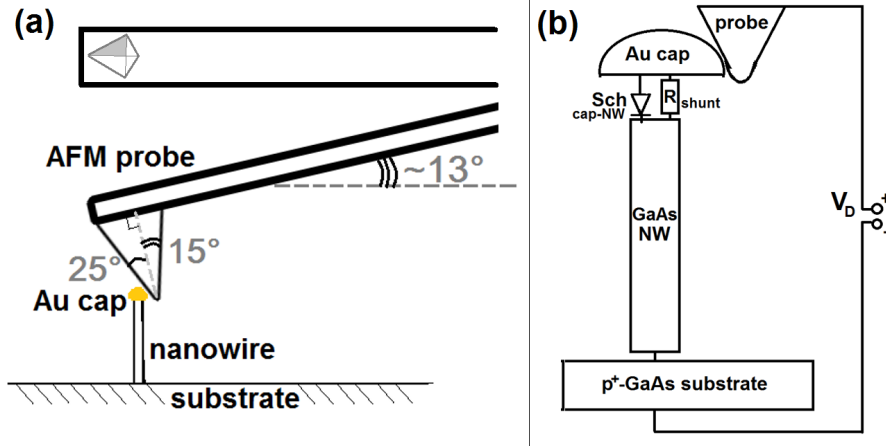


Figure 4.4 (a) Schematics indicating the geometry of contact between AFM pyramidal tip and the vertical NW, where most conductive facet is shaded. (b) Equivalent electric circuit for the measured system. Resistance of the substrate, Au cap, probe and probe-cap area are considered negligible, while resistance of the shunt is high.

Summary of the I-V curves for various passivation materials covering the side surfaces of GaAs NWs is shown in Figures 4.5 and 4.6. It seems beneficial to represent the characteristics in logarithmic scales because linear parts of the curves in logarithmic scales can indicate the specific potential of opening of the Schottky energy barrier and beginning of the linear Ohmic resistive regime. Moreover, we were able to calculate the resistivity of the NWs and evaluate the mobility of charge carriers on the basis of the thermionic emission theory. We applied the following protocol to evaluate the mobility of carriers in the studied NWs.

The diode law describing the conductance of the Schottky diode is described by formula (Zhang, 2007):

$$I_d = I_0 \cdot (\exp^{\frac{qU}{k_B T}} - 1) \quad (4.1.1)$$

where I_d is current through a diode, I_0 is leakage current in reverse bias, U is applied bias, elementary charge $q = 1.6 \cdot 10^{-19}$ C, $k_B = 1.38 \cdot 10^{-23}$ [J/K] is the Boltzmann constant and T is an absolute temperature of a diode.

The resistivity R_{NW} of a semiconductor NW is found as (Zhang, 2007):

$$R_{NW} = \frac{L}{qn_A \mu \pi R^2} \quad (4.1.2)$$

where L is NW length (height), elementary charge $q = 1.6 \cdot 10^{-19}$ C, n_A is the doping level, μ is mobility and R is a NW radius.

The parameters for our sample: $L = 1 \mu\text{m}$, doping level $n_A = 10^{19} \text{ cm}^{-3}$, $R \sim 50 \text{ nm}$. Therefore, the mobility of major carriers in the NWs found $\mu \sim 400 \text{ cm}^2/\text{V}\cdot\text{s}$ from the inclination of linear parts in Figure 4.5b.

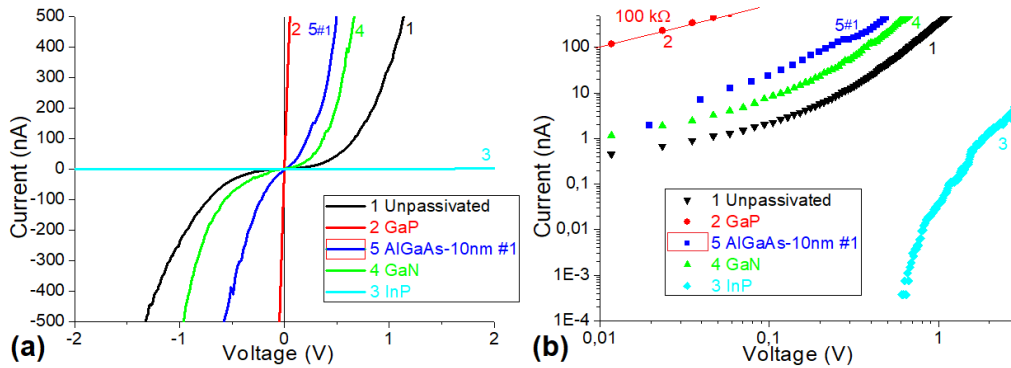


Figure 4.5 Comparison of I-V curves for p-GaAs NWs covered by four studied types of surface passivation. I-V curves are given in (a) linear and (b) double logarithmic scales for region of forward bias.

NWs with different types of passivation material are compared in Figures 4.5 and 4.6. On the basis of their I-V curves, it was possible to conclude that GaP leads to linear I-V curves with resistance around $100 \text{ k}\Omega$, while AlGaAs lead to passivation effect for 10 nm thick layer. Thicker AlGaAs passivation shells leads to an observable decrease in conductivity. InP leads to a fully insulating electrical element, while the reasons for this behavior still seems unclear, because photoluminescence data for the array lead to suggestions of significant carrier mobility in InP-passivated NWs. GaN showed an intermediate passivating effect, while it is still meaningful to check the layers impact for GaAs NWs with equal lengths and with passivation shell prepared by vapor-phase layering technique.

The measured resistances for the NWs were in the level of hundreds of $\text{k}\Omega$. Their values were corresponding with the expectations drawn from precursor flow parameters in the step of fabrication according to equation (4.1.2). Therefore, an increase of current coming from electrically biased NWs due to decrease of surface state density on the surface of NWs was registered for passivated NWs by C-AFM.

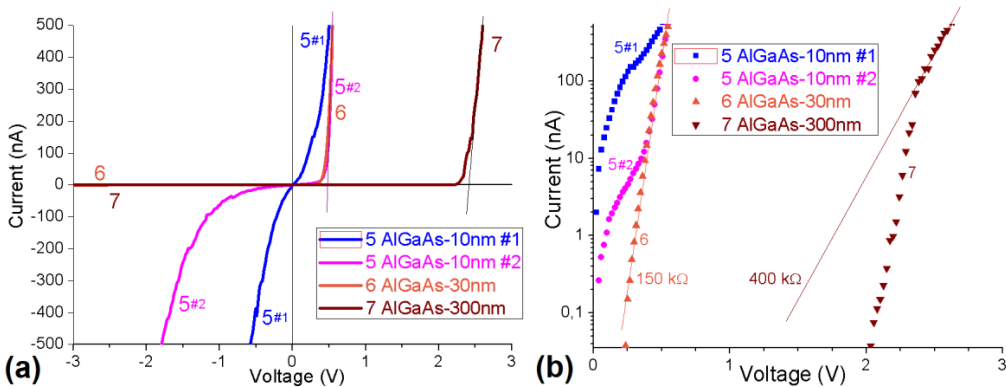


Figure 4.6 Comparison of p-GaAs NWs covered with AlGaAs shell layers. Electrical characteristics are given in (a) linear and (b) semi logarithmic scale for quadrant with forward bias. Two separate NWs are represented for sample with same thickness of passivation 10 nm.

We conclude that it is possible to use the C-AFM method based on PeakForce control of setpoint force for characterization of properties of individual NWs in an array. This method can provide data about resistivity and allow fast control of quality and distribution of properties within an array of fabricated NWs.

4.2 Simulation of charge accumulation in nanowires and influence of native oxide shell

2 samples with different levels of doping for both NW and substrate were fabricated by VLS mechanism inside MOVPE chamber (described in Publication VI). We compared the results of AFM experiments (KPFM and I-V curves) and computer simulation.

Numerical model with ATLAS in Silvaco (SILVACO Inc., 2015) software was used for modeling of electrical properties of GaAs NWs and charge accumulation in its surface oxide. The distributions of electric potential in native oxide of the p⁺-GaAs NWs under three levels of reverse bias are presented in Figure 4.7a. The Schottky barrier is located in the left part while the Ohmic contact is situated on the right. It is clear that the major part of the voltage drop occurs non-linearly in the close proximity with the Schottky barrier. In order to compensate the additional energy of the system it is needed to have the positive electric charge being installed into the oxide layer. Location of this installed charge is shown in Figure 4.7bcd. These figures show the modelled semi-cross sections of the NW near the Schottky barrier under 10V reverse bias. We modelled the electron concentrations inside the surface oxide layer of the NW. Three types of surface charge were modelled. It appeared that accumulation of the majority carriers in the surface oxide layer of the low-doped NWs will lead to decrease of electrical conductance. At the same time, the modeled increase of conductance in highly doped NWs can be explained by reinforcement of the recombination current.

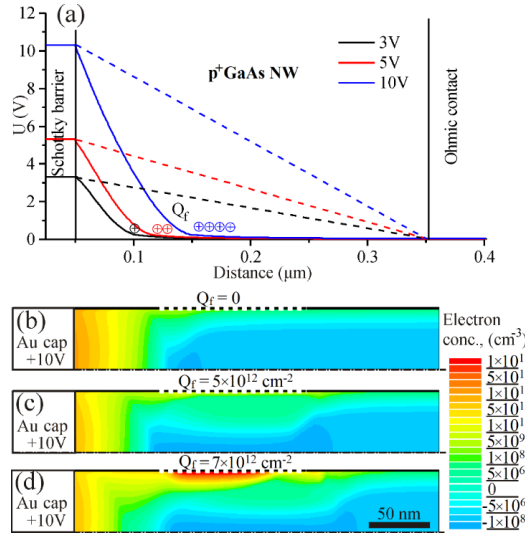


Figure 4.7 (a) Distribution of electric potential in the surface oxide of a GaAs NW under reverse bias 3 – 10 V applied to the Schottky barrier at the border between the Au cap and the NW. Q_f indicates the location of the charge accumulated in the surface oxide. The dashed lines indicate the linear potential distribution. (b) - (d) Semi-cross-sectional maps of the distribution of electron density under different Q_f in surface oxide layers near the surface charge region of the Schottky barrier under +10 V applied to the Au cap.

Later we performed the experimental measurements on the p^+ -GaAs NWs grown on the n^+ -GaAs substrate. The I-V curves and experimental schemes are shown in Figure 4.8. We performed the I-V curve measurement with two different sweeping rates, i.e. velocity of change of the external bias applied to the sample. Firstly, we notice the hysteresis of the current on both of these I-V curves. This represents the charge accumulation in the system. Secondly, the area of the hysteresis for the case of lower sweeping rate is higher than for the faster change of the potential. It means that the charges are accumulated in the slow states. Therefore, we assumed that the accumulation occurs near the Schottky barrier. Lastly, we performed the same experiment on p-GaAs NWs grown on the p^+ -GaAs substrate (Figure 4.9). The I-V curves also represented hysteresis. However, the direction of the hysteresis appeared inverted in comparison to Figure 4.8. Considering the characteristic lifetimes of the charges we concluded that the charge accumulation occurred exactly in the surface oxide of these NWs.

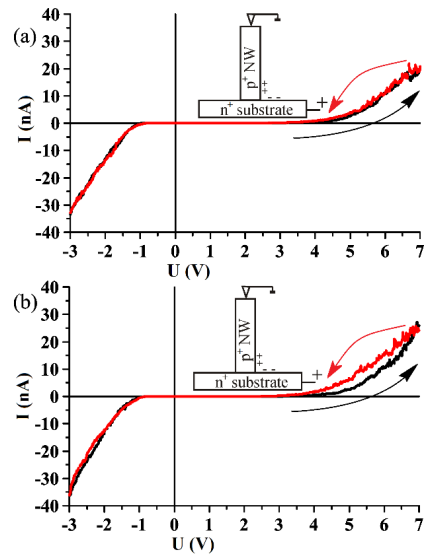


Figure 4.8 I–V curves of vertical p^+ -GaAs NW grown on an n^+ -GaAs substrate. The black and red curves denote measurements corresponding to an increase or decrease of the voltage. The bias sweeping rates were (a) 4 V/sec and (b) 1 V/sec. The insert shows the experimental arrangement.

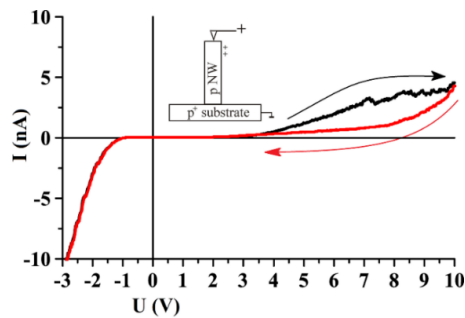


Figure 4.9 I–V curves of vertical p-GaAs NW grown on a p^+ -GaAs substrate. The black and red curves denote measurements corresponding to an increase or decrease of the voltage. The bias sweeping rate was 4 V/sec. The insert shows the experimental arrangement.

In order to verify the hypothesis, we simulated the vertical NW and modeled the distribution of charges and I-V curves for various surface charges installed in few locations on the NW and in the nearby location on the substrate. Figure 4.10a shows the model and colored distribution of the current density. Experimental and modelled I-V curves for p^+ -GaAs NW grown on an n^+ -GaAs substrate (Figure 4.10b) were completely matching with each other. Variation of the fixed charge density shown in Figure 4.10c lead to matching experimental curve with the modeled one for the $Q_{f1}=10^{12} \text{ cm}^{-2}$. Figure

4.10d depicts the raise in surface charge density and how it leads to reduction of the reverse current through the Schottky barrier.

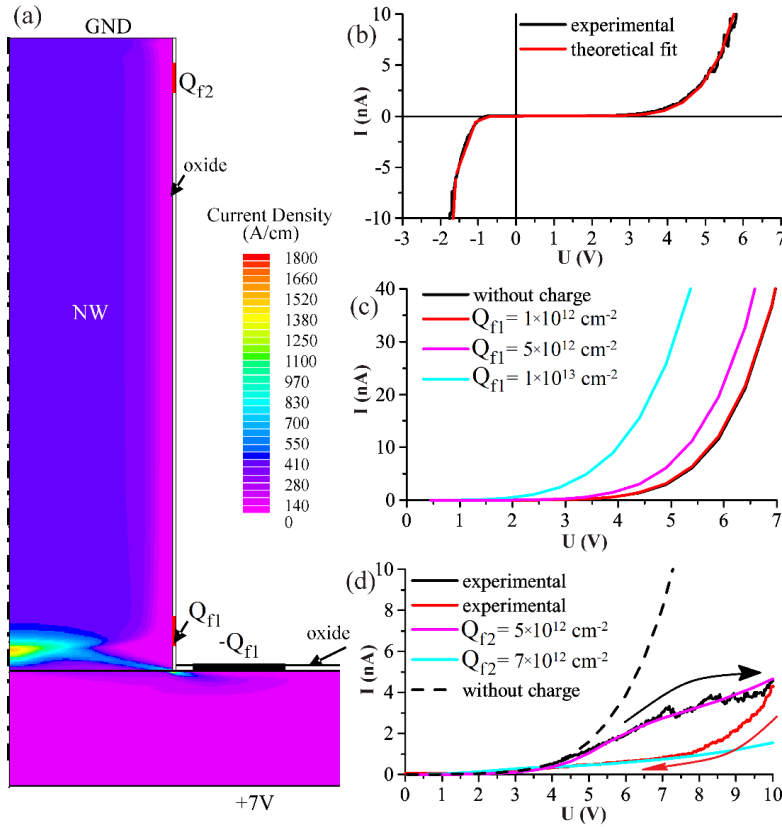


Figure 4.10 (a) Semi-cross section of vertical p⁺-NW on the n⁺-GaAs substrate with simulated distribution of the current density under the bias voltage of +7 V. Q_{f1} and Q_{f2} are the positions of fixed charge densities. (b) Experimental and simulated I–V curves of p⁺-NW on the n⁺-GaAs substrate. (c) Simulated I–V curves of p⁺-NW on the n⁺-GaAs substrate with a different fixed charge density Q_{f1}. (d) Experimental and simulated I–V curves of the p-NW on the p⁺-GaAs substrate with a different fixed charge density Q_{f2}.

Therefore, it was possible to record and explain the hystereses observed for p-doped GaAs NWs on different substrates. The charge accumulation near the Schottky barrier in the native oxide lead to intensified current for highly doped NWs based on intensified recombination of carriers and to decrease of the current for low-doped NWs explained by blockage of the conduction channel.

4.3 Numerical modeling of elasticity based on bending experiment with individual tapered NWs

The experimental approach we have used and corresponding results reported in Publications III-V employed the bending profiles taken along single inclined NWs. We presented the shortened derivation of the necessary formula, which has few non-obvious mathematical transitions in Publication V and in Supplementary material to Publication IV. In order to clarify few complicated transitions, the complete derivation was formulated as follows.

Our approach was based on the Hooke's law and the Euler-Bernoulli theory. The body compression law (Hooke's law) states that (Gere, 2012):

$$F = k\delta \quad (4.3.1)$$

where k is a linear stiffness coefficient, i.e. spring constant, of a structure and δ is a linear displacement, i.e. deformation, by the force F acting in same axis with the deformation.

In case of a NW bended by force F until its bended position through deflection $\omega(x)$ (please note that $\omega \propto \delta$) distributed along the length of a NW the equation should be written as:

$$F = k_{NW}(x) \cdot \omega_{NW,F}(x) \quad (4.3.2)$$

Noteworthy that the "spring constant" k_{NW} was not invariable along the NW structure in our bending experiment, but depended from a distance to the fixed end $x \in [0, L]$, where L is length of a NW.

Deflection of a NW $\omega_{NW,F}$ under certain applied force F is a parameter measurable from SPM topography data (Figures 3.12b, 3.14a, 4.12bc):

$$\omega_{NW,F}(x) = \Delta height = h_F(x) - h_0(x) \quad (4.3.3)$$

where h is the registered height, so that $h_{10nN}(x)$ is the height observed by SPM when the probe pushes with a setpoint force 10 nN at a certain coordinate $x \in [0, L]$.

It should be noted that F is a fixed setpoint parameter in PeakForce mode of AFM and this setpoint force is established with piconewton accuracy in QNM regime. The spring constant k is known as dependent from the leg distance x , so that relation between k and x is approximately cubic for a cylindrical beam $k \sim x^3$ similar to experimental plot of flexibility profile $f(x)$ in Figures 3.9e and 4.13e. (We will later calculate how exactly k is related with x for a tapered beam with the cone angle 2γ and radius in the middle of the NW's length R_{mid} shown in Figure 4.11) Height $h_0(x)$ is typically considered as the height of a structure scanned by SPM. Despite that, the topography is in fact always measured under specific setpoint force applied by SPM, resulting in a small deformation of all scanned objects. Therefore, we need to assume the force established for acquisition of $h_0(x)$ profiles as negligible. Unlike SPM, HR-SEM visualization do not bend the

structures and allows measuring of sizes with affordable accuracy, but in practice SPM setpoint force is ~ 10 pN for a gentle scanning, which is also affordably small. Moreover, one of our major motivations was to demonstrate the possibility to avoid expensive and laborious SEM-coupled AFM stations for such task.

Euler-Bernoulli beam theory defines bending of an isotropic beam (Labuschagne, 2009; Gere, 2012), depending on its composition (by elastic modulus of a certain material $E \equiv E_{mat}$) and geometrical shape of a beam, e.g. by length L and radius R under the applied load Q :

$$E \frac{d^2}{dx^2} (I(x) \frac{d^2 w(x)}{dx^2}) = Q \quad (4.3.4)$$

where $I(x)$ is the second moment of inertia of a beam and Q is the distributed load.

The equation for deflection of a bulk/beam/NW by the point contact (established by an SPM probe along the coordinate $x \in [0, L]$ on the NW) considers the static load $Q = 0$:

$$\frac{d^2}{dx^2} E_{mat} I(x) \frac{d^2}{dx^2} w(x) = 0 \quad (4.3.5)$$

It is required to consider the four appropriate boundary conditions to solve the task, so that Euler-Bernoulli beam is considered fixed at one end. For the base of the NW ($x = 0$), which is the fixed end, the boundary conditions are written as:

$$w|_{x=0} = 0 \quad (4.3.5.a); \quad \left. \frac{dw}{dx} \right|_{x=0} = 0 \quad (4.3.5.b).$$

The physical meaning of these two boundary conditions are #1: the bending equal to zero at the fixed end and #2: the slope equal to zero at the fixed end, correspondingly.

The boundary conditions for the free end of the beam ($x = L$), which is the upper unfixed part of the NW, where the force F is applied:

$$\left. \frac{d^2 w}{dx^2} \right|_{x=L} = 0 \quad (4.3.5.c); \quad \left. \frac{d^3 w}{dx^3} \right|_{x=L} = \frac{-F}{E_{mat} I(L)} \quad (4.3.5.d).$$

The physical meaning of the latter two boundary conditions are #3: the bending moment (skewness) equal to zero at the free end and #4: the first derivative of bending moment is the shear force that is equal to zero (which leads to formulation of criterion of units per surface area equal to $\frac{-F}{E_{mat} I(L)}$) at the free end, correspondingly. The last condition clearly

separates the measurable parameters on the object, i.e. coordinate x and applied impact F from the object's parameters, i.e. strength of its material E_{mat} and geometrical shape I .

The problem is thereby formulated as follows. We need to solve the Euler-Bernoulli equation for the case of the tapered beam. The major considerations of our model are point force bending by the force at the free end, small bending deflection and absence of rotation.

The analytical solution is done through derivation of equation linking the measured parameters (deflection), known argument (coordinate) and desired parameter (elastic modulus). Should be specially noted that in the object, the parameters of material (elastic modulus) must be separated from the geometrical parameters (shape) of the structure.

Initially, let us perform integration of the eq. (4.3.5) twice. We get the following:

$$\frac{d}{dx} E_{mat} I(x) \frac{d^2}{dx^2} w(x) = A \quad (4.3.6)$$

$$E_{mat} I(x) \frac{d^2}{dx^2} w(x) = Ax + B \quad (4.3.7)$$

where A and B are constants, whose values will be determined from the boundary conditions.

Let us put the boundary condition (4.3.5.c) into equation (4.3.7). The result is:
 $0 = AL + B$.

Therefore $B = -AL$, which should be put in equation (4.3.6.b), resulting into:

$$E_{mat} I(x) \frac{d^2}{dx^2} w(x) = A(x - L) \quad (4.3.8)$$

It is necessary to perform additional transition in order to utilize the boundary condition 4.3.5.d with the third order derivative. Let us differentiate the eq. (4.3.8). We obtain:

$$E_{mat} \left(\frac{d}{dx} I(x) \cdot \frac{d^2}{dx^2} w(x) + I(x) \cdot \frac{d^3}{dx^3} w(x) \right) = A \quad (4.3.9)$$

Inserting the boundary conditions (4.3.5.c) and (4.3.5.d) we obtain:

$$E_{mat} \left(0 + I(L) \cdot \frac{-F}{EI(L)} \right) = A$$

Therefore finding the value of constant A : $A = -F$.

Thus, we have found constants A and B and have transformed the differential equation of the fourth order (4.3.8) to the equation of the second order (4.3.10):

$$E_{mat} I(x) \frac{d^2}{dx^2} w(x) = -F(x - L) \quad (4.3.10)$$

Here it is needed to recall the scheme representing a simple geometrical model of a tapered NW (see Figure 4.11). The taper angle “ α ” from Publication IV is written as “ γ ”

in the present thesis in order to avoid misspelling with the coefficient “ a ” used instead of “ u ” later on in formula 4.3.12. The taper angle was considered small (in the order of few degrees as seen from the Table 2) for the studied NWs. Therefore, it was considered that $\gamma = \sin \gamma$ using the small angle approximation. $\sin \gamma = AC/AB$; $R(L) = 0$; $R(0) = 2R_{mid}$; $AC = R_{mid}$; $\gamma = 2R_{mid}/L$. In general for the cone: $R(x) = 2xR_{mid}/L$. The case of a tapered beam is more generalized than cone and more complicated. Later on we will introduce coefficient $u = \gamma/R_{mid}$.

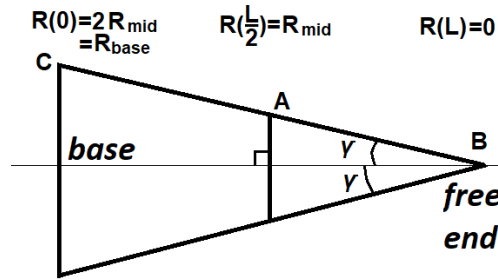


Figure 4.11 Cone shape of a NW with cone angle 2γ , taper angle γ , NW length L and $\sin \gamma \approx \gamma$.

Further, it is needed to find the formulation of the second moment of inertia $I(x)$ of the tapered beam. The second moment of inertia (also called the moment of inertia of a plane area) is a characteristic that describes geometrical characteristic of a body denoting its resistance to bending as a function of the body’s shape. For the beam having the tapered (or conical) shape, the cross-sections perpendicular to the long axis are circles. The radius of the tapered beam linearly depends from the coordinate x :

$$R(x) = R_{mid} + \sin \gamma(x - L/2) \quad (4.3.11)$$

while $\sin \gamma$ is a constant and $(x - L/2) = 0$ in the middle of the beam.

$$R(x) = R_{mid} + \gamma(x - L/2) = R_{mid}(1 + u(x - L/2)) \quad (4.3.12)$$

Here we introduced the coefficient $u = \gamma/R_{mid}$ where γ is the taper angle and R_{mid} is the average radius of the tapered beam. This coefficient defines the geometrical tapering parameter of a certain NW and is useful for computational script used for processing of the experimental data. The coefficient is found from the HR-SEM images. It is introduced here to shorten the written form of expressions in equations (4.3.12) – (4.3.28).

The 2nd moment of inertia $I(x)$ of a filled circular area with the radius $R(x)$ of a general case of a tapered/conical beam is found as:

$$I(x) = \iint_S z^2 dx dy = \int_0^{2\pi} d\varphi \int_0^{R(x)} \rho d\rho \cdot \rho^2 \cos^2 \varphi = \pi \frac{R(x)^4}{4} \quad (4.3.13)$$

This was solved in spherical coordinates, where $S, z, x, y, \rho, \varphi$ are parameters of our model presented in spherical coordinates.

Let us put the equation (4.3.12) instead of $R(x)$ and we will obtain:

$$I(x) = \frac{\pi R_{mid}^4}{4} (1 + u(x - L/2))^4 \quad (4.3.14)$$

Let us move E_{mat} and $I(x)$ into the right side of the equation (4.3.10):

$$\frac{d^2 w(x)}{dx^2} = \frac{F}{E_{mat}} \frac{4}{\pi} \frac{1}{R_{mid}^4} \frac{-(x-L)}{(1+u(x-L/2))^4} \quad (4.3.15)$$

Here we put away the minus sign before the right part of the equation for simplicity of the formula. Since the coordinate plane for the system has positive values above the axis of the beam, then deflection by the force F applied from the top (as seen in the Figures 3.13d, 3.14a and 4.12c) leads to bending in the direction of negative values in the geometrical coordinates. We are interested solely in the deflection values, but not in its known direction, so the absolute values of deflection might be taken to calculate the elastic modulus E_{mat} .

$$\frac{d^2 w(x)}{dx^2} = \frac{F}{E_{mat}} \frac{4}{\pi} \frac{1}{R_{mid}^4} \frac{(x-L)}{(1+u(x-L/2))^4} \quad (4.3.16)$$

Let us integrate the equation (4.3.16) by x :

$$\frac{dw(x)}{dx} = \frac{F}{E_{mat}} \frac{4}{\pi} \frac{1}{R_{mid}^4} \frac{-2}{3u^2} \left(\frac{2-5uL+6ux}{(2-uL+2ux)^3} + C \right) \quad (4.3.17)$$

C is the constant, found from the boundary condition (4.3.5.b):

$$0 = \frac{F}{E_{mat}} \frac{4}{\pi} \frac{1}{R_{mid}^4} \frac{-2}{3u^2} \left(\frac{2-5uL}{(2-uL)^3} + C \right) \quad (4.3.18)$$

Considering that $\frac{F}{E_{mat}} \frac{4}{\pi} \frac{1}{R_{mid}^4} \frac{-2}{3u^2} \neq 0$ because none of the parts are equal to zero, including $F \neq 0$, because in such case the problem has no sense since no reason for bending occurs. Thus:

$$0 = \frac{2-5uL}{(2-uL)^3} + C,$$

$$\text{which means that } C = -\frac{2-5uL}{(2-uL)^3}. \quad (4.3.19)$$

By inserting this value into the eq. (4.3.17) we obtain:

$$\frac{dw(x)}{dx} = \frac{F}{E_{mat}} \frac{4}{\pi} \frac{1}{R_{mid}^4} \frac{-2}{3u^2} \left(\frac{2-5uL+6ux}{(2-uL+2ux)^3} - \frac{2-5uL}{(2-uL)^3} \right) \quad (4.3.20)$$

After integration of this equation by x we obtain:

$$w(x) = \frac{F}{E_{mat}} \frac{4}{\pi} \frac{1}{R_{mid}^4} \frac{-2}{3u^2} \left(\frac{(2-5uL)x}{(-2+uL)^3} + \frac{2+uL}{2u(2-uL+2ux)^2} - \frac{3}{2u(2-uL+2ux)} + D \right) \quad (4.3.21)$$

D is a constant that can be found from the boundary condition (4.3.5.a):

$$0 = \frac{2+uL}{2u(2-uL)^2} - \frac{3}{2u(2-uL)} + D,$$

$$\text{which means that } D = -\frac{2+uL}{2u(2-uL)^2} + \frac{3}{2u(2-uL)}. \quad (4.3.22)$$

By inserting this value into the equation (4.3.21) we obtain:

$$w(x) = \frac{F}{E_{mat}} \frac{4}{\pi} \frac{1}{R_{mid}^4} \frac{-2}{3u^2} \left(\frac{(2-5uL)x}{(-2+uL)^3} + \frac{2+uL}{2u(2-uL+2ux)^2} - \frac{3}{2u(2-uL+2ux)} - \frac{2+uL}{2u(2-uL)^2} + \frac{3}{2u(2-uL)} \right) \quad (4.3.23)$$

Luckily, this long formula can be simplified by assembling the parts inside the brackets:

$$w(x) = \frac{F}{E_{mat}} \frac{4}{\pi} \frac{1}{R_{mid}^4} \frac{-2}{3u^2} \frac{4u^2x^2(3uL^2+2x-L(6+5ux))}{(-2+uL)^3(2-u(L-2x))^2} \quad (4.3.24)$$

At last, the formulation of the bending of the tapered beam in the coordinate between 0 and L under the force F applied in the location $x = L$ can be simplified and formulated as:

$$w(L) = \frac{F}{E_{mat}} \frac{4}{\pi} \frac{1}{R_{mid}^4} \frac{8x^2(3uL^2+2x-L(6+5ux))}{3(2-uL)^3(2-u(L-2x))^2} \quad (4.3.25)$$

However, we are interested in finding the bending in the location of the force applied by the AFM probe, i.e. at the end of the beam ($x = L$). In order to find such generalized formulation for the bending, let us put $x = L$ into the formula (4.3.25):

$$w(L) = \frac{F}{E_{mat}} \frac{4}{\pi} \frac{1}{R_{mid}^4} \frac{16L^3}{3(2-uL)^3(2+uL)} \quad (4.3.26)$$

This equation can be modified and expressed as:

$$\frac{w(L)}{F} = \frac{4}{3\pi} \frac{1}{E_{mat}} \frac{L^3}{R_{mid}^4} \frac{1}{(1+uL/2)(1-uL/2)^3} \quad (4.3.27)$$

It is needed to highlight here that this equation determines the bending of the beam in the location of the force applied at $x = L$. Now we want to obtain the formula for the NW bending when the AFM probe acts in each of the interim locations x between 0 and L ($x \in [0, L]$). In order to do that, three conditions should be met:

- (i) L should be changed to x ;
- (ii) the universal R_{mid} must be changed to the effective average radius $R_m(x)$:

$$R_m(x) = R_{mid} + \frac{\gamma}{2}(x-L) \quad (4.3.28)$$

The effective average radius will change due to the movement of the AFM probe from the base to the free end of the beam, i.e. NW. Here we state that it is necessary to consider that the "effective average radius of the deformed part of tapered NW" changes with the shift of the location of the force applied (from the NW base to the NW free end). This tricky moment indicates the effective meaning of this radius R_m as a measure of the system considered, but not the real object's dimensional property itself.

- (iii) u must be changed to $\gamma/R_m(x)$, instead of $\gamma/R(x)$. Please note that we prefer not to introduce an additional coefficient (like u_m) here, but will return u in (4.3.34) instead.

After implementing of all the items above, we obtain the formula for the bending in x :

$$\frac{w(x)}{F} = \frac{4}{3\pi} \frac{1}{E_{mat}} \frac{x^3}{R_m(x)^4} \frac{1}{(1+\gamma x/2R_m(x))(1-\gamma x/2R_m(x))^3} \quad (4.3.29)$$

This equation can be simplified to reach the form:

$$\frac{w(x)}{F} = \frac{4}{3\pi} \frac{1}{E_{mat}} \frac{x^3}{(R_m(x) + \gamma x/2)(R_m(x) - \gamma x/2)^3} \quad (4.3.30)$$

Let us put $R_m(x) = R_{mid} + \frac{\gamma}{2}(x-L)$ into the equation (4.3.30), so we obtain:

$$\frac{w(x)}{F} = \frac{4}{3\pi} \frac{1}{E_{mat}} \frac{x^3}{(R_{mid} + \frac{\gamma}{2}(x-L) + \gamma x/2)(R_{mid} + \frac{\gamma}{2}(x-L) - \gamma x/2)^3} \quad (4.3.31)$$

This formula can be simplified to the form:

$$\frac{w(x)}{F} = \frac{4}{3\pi} \frac{1}{E_{mat}} \frac{x^3}{(R_{mid} + \frac{\gamma}{2}(2x-L))(R_{mid} - \frac{\gamma}{2}L)^3} \quad (4.3.32)$$

Now let us put R_{mid} the out of the brackets:

$$\frac{w(x)}{F} = \frac{4}{3\pi} \frac{1}{E_{mat}} \frac{1}{R_{mid}^4} \frac{x^3}{\left(1 + \frac{\gamma}{2R_{mid}}(2x-L)\right)\left(1 - \frac{\gamma}{2R_{mid}}L\right)^3} \quad (4.3.33)$$

After utilizing $u = \gamma/R_{mid}$ transition we obtain:

$$\frac{w(x)}{F} = \frac{4}{3\pi} \frac{1}{E_{mat}} \frac{1}{R_{mid}^4} \frac{x^3}{\left(1 + \frac{u}{2}(2x-L)\right)\left(1 - \frac{u}{2}L\right)^3} \quad (4.3.34)$$

After considering $\frac{w(x)}{F} = \frac{1}{k(x)}$ and simplification we obtain the final form of the equation

that can be used to perform quantitative analysis of the bending of the tapered beams and NWs in our experiments (formula #3 in Publication IV, where “ α ” is changed to “ u ” here):

$$\frac{1}{k(x)} = \frac{4}{3\pi} \frac{1}{E_{mat}} \frac{1}{R_{mid}^4} \frac{x^3}{\left(1 + u(x-L/2)\right)\left(1 - uL/2\right)^3} \quad (4.3.35)$$

Thus, equation for the Young’s modulus of a material in a tapered beam is expressed as:

$$E_{mat} = \frac{4}{3\pi} k(x) \frac{1}{R_{mid}^4} \frac{x^3}{\left(1 + u(x-L/2)\right)\left(1 - uL/2\right)^3} \quad (4.3.36)$$

When we have averaged the $k(x)$ for a certain NW bent by few different setpoint forces, we can finally calculate the elastic modulus E_{mat} in NWs. If the coefficient u is identical for all the NWs within the sample (low dispersion of tapering angle and lengths for the studied array), then the equation (4.3.36) can be used. This equation is equivalent to the formula #12 in Publication V, while the taper angle “ α ” is written as “ γ ” in order to avoid misspelling with the coefficient “ a ” written in Publication IV instead of “ u ”.

However, if the NWs in the array has slightly different shapes due to the fabrication conditions (and the taper angle is different for them), then the general equation of the following form can appear more useful in practice for each NW:

$$E_{mat} = \frac{64}{3\pi} \frac{1}{f_{NW}(x)} \frac{1}{D_{mid}^4} x^3 \frac{1}{\left(1 + \frac{\gamma}{D_{mid}}(2x-L)\right)\left(1 - \frac{\gamma L}{D_{mid}}\right)^3} \quad (4.3.37)$$

The latter formula (4.3.37) is universal for cylindrical ($\gamma = 0$) and conical ($\gamma \neq 0$ but is small enough) beams since it represents the complex case of a tapered beam. In addition, it is possible to distinguish the parts responsible for the shape, coordinate and measured experimental values for one certain individual NW. Apart from constants, (1) E_{mat} is physical property of the material in certain NW; (2) R_{mid} , L and $u = \gamma/R_{mid}$ are geometrical properties of a certain NW; (3) x is a controlled experimental parameter of the experiment

(argument) and (4) $k(x)$ is the measured experimental parameter (function). This separation allows to see how the interpretation of the experimentally measured values for a model (geometrical shape with physical parameters) within specific theory results into formulation of purely the material's property. Therefore, its usability can appear important not only for future studies of NWs, but also for classical Mechanics and Civil engineering areas. Surprisingly, we did not find the expression consistent to (4.3.37) relating the elastic modulus of material and stiffness/flexibility of the strained tapered beam in the literature even though Mechanical science is few centuries old.

As mentioned earlier in Section 3.2, in order to quantify the values of elasticity we performed the following averaging method (see Figure 4.12). The script was written in Origin software in order to correlate the flexibility coefficient with the measured experimental bending profiles. Autocorrelation allowed modeling of the flexibility profiles along the NWs for different forces applied. Normalizing the flexibility coefficients to equal force lead to consilience of the profiles (see black curve in Figure 4.12e). This supports the assumption that all bending profiles for different forces were taken in elastic regime along the entire length of the NWs. Averaging of the profiles lead to the summarized bending profile (see red curve in Figure 4.12e). This joined profile based on approximately 2 thousand data points of experimental AFM bends was modelled with the script equation in order to obtain the value of the Young's modulus of the NW considering its average radius as the size-parameter of the nanomaterial.

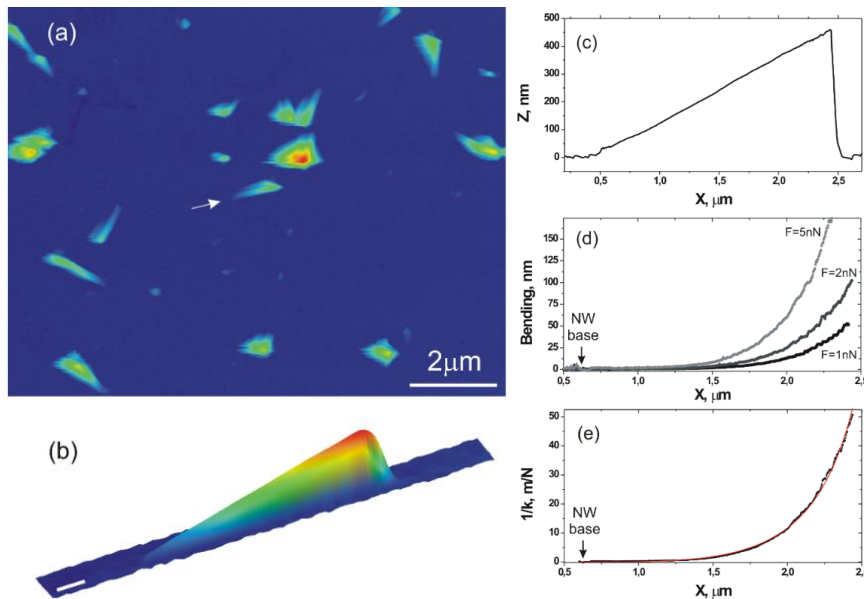


Figure 4.12 (a) SPM image of the inclined InP NWs; (b) 3D SPM image of one of the InP NWs when scanning it with ultralow force $F_{\approx 0} = 0.05$ nN; (c) cross-section profile for $h(x)_{0.05nN}$; (d) bending profiles for various values of Peak force $\omega(x)_{1nN}$, $\omega(x)_{2nN}$ and $\omega(x)_{5nN}$; (e) flexibility profile $1/k(x)$ measured for one InP NW and smooth fitting curve using the equation (4.3.37) for a tapered beam.

Different NWs had different lengths and thicknesses with small variation. Moreover, the thinnest NWs were predominantly comprised of WZ phase InP. Therefore, we obtained the data points of the Young's modulus for 16 NWs under the study. Comparison of these data points (with consideration of the calculated experimental accuracy of each measurement) demonstrates that the NWs had typically higher values of elasticity. At the same time, it is known that the elastic modulus of WZ phase in [0001] direction is equal to elastic modulus of ZB phase in [111] direction. Thus, the explanation of the observed stepwise increase of the Young's modulus of InP in the NWs (levels are visible in Figure 4.13) was either in the core-shell influence or in the WZ/ZB mixing.

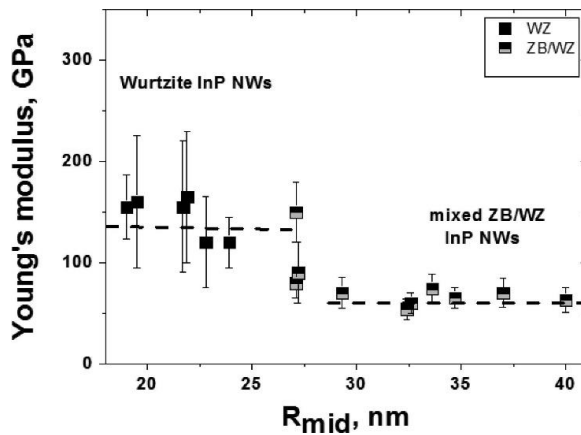


Figure 4.13 Dependence of the measured Young's modulus from the average radius of conical InP NWs.

The model introduced by Chen (Chen, 2006) uses the equation (3.2.1). The core-shell modelling ($E_{core} = 60$ GPa, $E_{shell} = 130$ GPa, $R_{shell} = 1$ nm) of experimental results $E_{mat}(R)$, which fits well the region with average NW radius $R > 27$ nm (InP NWs with 1 nm thick native oxide), is shown in Figure 4.14. We applied the tabulated values of hardness of oxide I_2O_3 130 - 150 GPa, and geometrical parameters of possible oxide with the value of elastic modulus of bulk InP material 60 GPa into the equation (3.2.1). It is clear that the modelled curve shown in Figure 4.14a lacks the accuracy in description of NWs with average $R < 27$ nm. Therefore, such model is inadequate. However, if we try to perform the core-shell modelling of experimental results $E_{mat}(R)$ in such a way that they fit well all the experimental data (Figure 4.14b), then the model requires inadequate fitting parameters. We can state that because it is incorrect and inadequate that elastic modulus of the core is negative $E_{core} = -50$ GPa and shell material exceeds the hardness of hardest known materials $E_{shell} = 1000$ GPa, while $R_{shell} = 1$ nm. Variation of R_{shell} did not significantly affect the result and thickness was controlled by TEM as discussed previously in Section 3.2. These results can be accessed in more details in supplementary material to Publication IV.

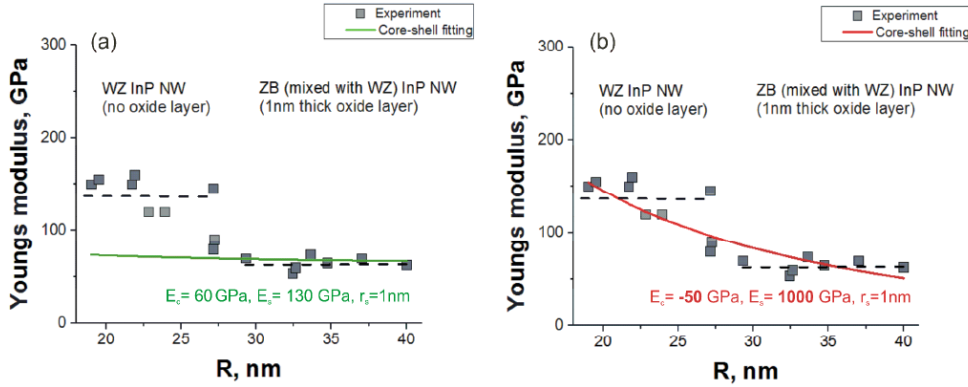


Figure 4.14 (a) The core-shell modelling ($E_{core} = 60$ GPa, $E_{shell} = 130$ GPa, $R_{shell} = 1$ nm) of experimental results $E_{mat}(R)$, that fits well the region with average NW radius $R > 27$ nm (InP NWs with 1 nm thick native oxide), but lacks the description of NWs with average $R < 27$ nm. (b) The core-shell modelling ($E_{core} = -50$ GPa, $E_{shell} = 1000$ GPa, $R_{shell} = 1$ nm) of experimental results $E_{mat}(R)$, that fits well all the experimental data, but requires inadequate fitting parameters.

After the value of Young's modulus for WZ InP [0001] was found, we compared our observations about decline in elastic modulus with the similar results for semiconductor NWs available in the literature. Interestingly, similar discoveries about decrease of the elastic modulus by ~ 40 - 50% were reported previously for the mixed ZB/WZ phase structures in ZnS (Moon, 2015) and InAs (Lexholm, 2009), which is also a III-V semiconductor material.

According to Moon and coauthors (see "Fig. 11a" in (Moon, 2015)) that the 30% decrease from the expected Young's modulus for ZnS NWs is explained by ZB/WZ mixing. It is also remarkable that ZB(111) and WZ(0001) phases of ZnS have approximately similar values of the Young's modulus. According to the authors, the reason for decreasing of the Young's modulus was that phase borders of ZB and WZ phases in polytypical NWs are potentially deformable/weak/defectuous sites. These defects reduce the strength of material and lead to formation of areas providing significant deformability under extensive loads. This factor finally leads to fractures inside a nanostructure.

Similar effect of decreasing of the Young's modulus was observed by Lexholm for ZB InAs NWs (Lexholm, 2009). The value of elastic modulus was reported to decline from $E_{mat}(111) = 97$ GPa (for bulk ZB InAs) to ~ 40 - 55 GPa (Figure 4.16), when the diameter of the NWs decreased from 100 nm to 40 - 50 nm. In other words, the declined diameter of the structure reduced the measured Young's modulus of NW material by ~ 40 - 50% based on "Fig. 3" in (Lexholm, 2009).

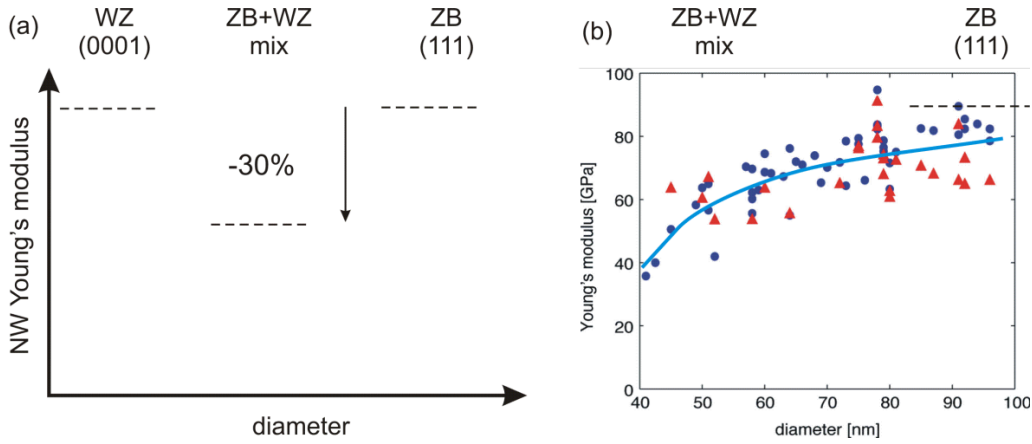


Figure 4.15 The influence of ZB/WZ mixing takes place. (a) Representation of the general principle valid for different III-V semiconductors. (b) Fitting of the data for InAs taken from Lexholm et.al. for ZB InAs NWs (Lexholm, 2009) (blue curve) also demonstrates ~ 40 - 50% decrease of the Young's modulus for the ZB/WZ mixed structure.

Consequently, we suppose that one of the possible factors affecting the decrease of experimentally measured Young's modulus of NWs (like in our case) is same effect caused by ZB/WZ mixing. Since modeling of the core-shell structure (Figure 4.15) lead to inadequate outcome, we conclude that the explanation of the decreased elastic modulus for thicker InP NWs (in the right part of the Figure 4.13) is in ZB/WZ mixing. The value of the Young's modulus of InP was found to be ~120 GPa. An increase of Young's modulus for pure WZ InP in NWs in comparison to mixed WZ/ZB crystal arrangement was registered. Corresponding value of Young's modulus ~120±10 GPa was measured in direction [0001].

In addition, it was possible to perform modeling of the nanostructure resembling the shape of the real object in COMSOL software (COMSOL Inc., 2014). This was done in order to verify the direction of plane where the deformation took place. The deformations of the real NWs were compared with the modelled structure and applied stress, so that the bends were the same for the ZB [100] and WZ [1000] directions. Therefore, we concluded that the value of Young's modulus was measured exactly in these directions.

4.4 Calculation of the elastic coefficients and elastic moduli of various crystal structures by the R.M.Martin's matrix transformation method

Consideration of the values of Young's moduli for ZB and WZ crystal structures of InP from ab initio principles and on the basis of numerical modeling based on elastic coefficients taken from acoustic experiments show that moduli for ZB and WZ phases should be nearly equal. We performed the calculation of elastic modulus of InP for

WZ[0001] and ZB[111] on the basis of method developed from old 1950s works of Mason and Nye matrix transformation method (Nye, 1957), R.M.Martin matrix transformation method (Martin, 1972) and Wang simulation method (Wang, 2003). We will later call it R.M.Martin's method, because we believe that his input to transformation of elastic coefficients is most closely related to our task. It appeared that the determined WZ elastic coefficients and related Young's modulus of material in specified direction of crystal support the adequacy of the values that were obtained on the basis of our AFM experiment.

In order to investigate the properties of material inside NWs it is initially needed to consider the geometry of experiment and to separate the features of the structure/shape from the properties of material. Methodical error, inaccurate calibration of measuring instrument, size effects and other reasons can affect the interpretation of the experimental result. However, independently from that, it is possible to model the theoretical properties of the crystal material in NWs with the help of developed Nye-Martin method (See supplementary material to Publication IV and SI).

The Nye method (Nye, 1957) involves utilization of known elastic coefficients for the ZB crystal and for WZ crystal, in order to determine the Young's modulus of material along [111] direction for ZB phase and [0001] axis for WZ material. At first, it is needed to know the coefficients C_{11} , C_{12} and C_{44} for ZB crystal and C_{11} , C_{12} , C_{13} , C_{33} , C_{44} , C_{66} for WZ crystal, while they are typically tabulated.

Equations for the corresponding elastic moduli are the following:

$$E_{ZB}[111] = 1/(S_{11} - 2/3(S_{11} - 2S_{12} - S_{44}/2)) \quad (4.4.1)$$

$$E_{WZ}[0001] = 1/S_{33} \quad (4.4.2)$$

The Nye estimation of the value of the Young's modulus of ZB InP in the direction [111] can be acquired from the matrix of elastic constants C_{ij}^{zb} and the compliance matrix S_{ij}^{zb} :

$$C_{ij}^{zb} = \begin{pmatrix} 102 & 58 & 58 & 0 & 0 & 0 \\ 58 & 102 & 58 & 0 & 0 & 0 \\ 58 & 58 & 102 & 0 & 0 & 0 \\ 0 & 0 & 0 & 46 & 0 & 0 \\ 0 & 0 & 0 & 0 & 46 & 0 \\ 0 & 0 & 0 & 0 & 0 & 46 \end{pmatrix} \quad (4.4.3)$$

$$S_{ij}^{zb} = \begin{pmatrix} 0.017 & -0.0060 & -0.0060 & 0 & 0 & 0 \\ -0.0060 & 0.017 & -0.0060 & 0 & 0 & 0 \\ -0.0060 & -0.0060 & 0.017 & 0 & 0 & 0 \\ 0 & 0 & 0 & 0.022 & 0 & 0 \\ 0 & 0 & 0 & 0 & 0.022 & 0 \\ 0 & 0 & 0 & 0 & 0 & 0.022 \end{pmatrix} \quad (4.4.4)$$

$$E^{zb}[111] = \frac{1}{s_{11} - 2/3(s_{11} - s_{12} - s_{44}/2)} = \frac{1}{0.017 - 2/3(0.017 + 0.006 - 0.022/2)} = 111 \text{ GPa} \quad (4.4.5)$$

The Martin transformation method (Martin, 1972) consists of matrix transformations applied to the experimentally measured elastic coefficients of the ZB material. Initially, it is needed to know the coefficients C_{11} , C_{12} and C_{44} . The method allows to calculate all elastic coefficients for the WZ crystal structure related with ZB structure. After that, it is simple to calculate the Young's modulus of the material in the desired direction of crystal lattice.

The matrix of elastic coefficients for WZ crystal has is written as:

$$\begin{pmatrix} C_{11}^{WZ} \\ C_{12}^{WZ} \\ C_{13}^{WZ} \\ C_{33}^{WZ} \\ C_{44}^{WZ} \\ C_{66}^{WZ} \end{pmatrix} = \frac{1}{6} \begin{pmatrix} 3 & 3 & 6 \\ 1 & 5 & -2 \\ 2 & 4 & -4 \\ 2 & 4 & 8 \\ 2 & -2 & 2 \\ 1 & -1 & 4 \end{pmatrix} \begin{pmatrix} C_{11}^{Zb} \\ C_{12}^{Zb} \\ C_{44}^{Zb} \end{pmatrix} - \begin{pmatrix} \Delta^2 / \overline{C_{44}^{WZ}} \\ -\Delta^2 / \overline{C_{44}^{WZ}} \\ 0 \\ 0 \\ \Delta^2 / \overline{C_{66}^{WZ}} \\ \Delta^2 / \overline{C_{44}^{WZ}} \end{pmatrix} \quad (4.4.6)$$

$$\text{where } \Delta = \sqrt{2}/6(C_{11}^{Zb} - C_{12}^{Zb} - 2C_{44}^{Zb}). \quad (4.4.7)$$

The $\overline{C_{ij}^{WZ}}$ components present in the formula describe the case of pure rotation.

As an example, it is possible to take ZB parameters of InP in GPa.

1) At first, we need to calculate the auxiliary parameters Δ , C_{44} and C_{66} .

$$\begin{aligned} \Delta &= 0.236(101 - 56 - 92) = -11 \\ \overline{C_{44}^{WZ}} &= \frac{1}{6(2C_{11} - 2C_{12} + 2C_{44})} = 30 \\ \overline{C_{66}^{WZ}} &= \frac{1}{6(C_{11} - C_{12} + 4C_{44})} = 38 \\ \Delta^2 / \overline{C_{44}^{WZ}} &= \frac{121}{30} = 4 \\ \Delta^2 / \overline{C_{66}^{WZ}} &= \frac{121}{38} = 3.2 \end{aligned}$$

2) Later, it is possible to use the equation to find all 6 coefficients for the WZ crystal.

$$\begin{pmatrix} C_{11}^{wz} \\ C_{12}^{wz} \\ C_{13}^{wz} \\ C_{33}^{wz} \\ C_{44}^{wz} \\ C_{66}^{wz} \end{pmatrix} = \frac{1}{6} \begin{pmatrix} 3 & 3 & 6 \\ 1 & 5 & -2 \\ 2 & 4 & -4 \\ 2 & 4 & 8 \\ 2 & -2 & 2 \\ 1 & -1 & 4 \end{pmatrix} \begin{pmatrix} 101 \\ 56 \\ 46 \end{pmatrix} - \begin{pmatrix} 4 \\ -4 \\ 0 \\ 0 \\ 3.2 \\ 4 \end{pmatrix} = \begin{pmatrix} 120.5 \\ 52.5 \\ 41 \\ 132.3 \\ 27.3 \\ 34.2 \end{pmatrix}$$

Namely:

$$C_{11}^{wz} = \frac{3C_{11} + 3C_{12} + 6C_{44}}{6} - 4 = 124 - 4 = 120$$

$$C_{12}^{wz} = \frac{1C_{11} + 5C_{12} - 2C_{44}}{6} + 4 = 48 + 4 = 52$$

$$C_{13}^{wz} = \frac{2C_{11} + 4C_{12} - 4C_{44}}{6} - 0 = 41$$

$$C_{33}^{wz} = \frac{2C_{11} + 4C_{12} + 8C_{44}}{6} - 0 = 132$$

$$C_{44}^{wz} = \frac{2C_{11} - 2C_{12} + 2C_{44}}{6} - 3.2 = 30 - 3.2 = 27$$

$$C_{66}^{wz} = \frac{C_{11} - C_{12} + 4C_{44}}{6} - 4 = 38 - 4 = 34$$

3) When all the WZ coefficients are found, it becomes possible to calculate the inversed matrix S_{ij}^{wz} for the matrix of elastic coefficients C_{ij}^{wz} . This step (but in fact all the previous steps also) can be simply performed in standard numerical packages like Wolfram Mathematica, MS Office, Origin or Maple.

$$C_{ij}^{wz} = \begin{pmatrix} 120 & 52 & 41 & 0 & 0 & 0 \\ 52 & 120 & 41 & 0 & 0 & 0 \\ 41 & 41 & 132 & 0 & 0 & 0 \\ 0 & 0 & 0 & 27 & 0 & 0 \\ 0 & 0 & 0 & 0 & 27 & 0 \\ 0 & 0 & 0 & 0 & 0 & 34 \end{pmatrix} \quad (4.4.8)$$

$$S_{ij}^{wz} = \begin{pmatrix} 0.011 & -0.0039 & -0.0021 & 0 & 0 & 0 \\ -0.0039 & 0.011 & -0.0021 & 0 & 0 & 0 \\ -0.0021 & -0.0021 & 0.0089 & 0 & 0 & 0 \\ 0 & 0 & 0 & 0.037 & 0 & 0 \\ 0 & 0 & 0 & 0 & 0.037 & 0 \\ 0 & 0 & 0 & 0 & 0 & 0.025 \end{pmatrix} \quad (4.4.9)$$

4) Finally, it is needed to take the coefficient S_{33} and to calculate the value of the Young's modulus of WZ InP in [0001] direction:

$$E_{mat}[0001] = 1/S_{33} = 1/0.0089 = 112 \text{ GPa.} \quad (4.4.10)$$

This value is very close to the abovementioned Young's modulus $E^{zb}[111]$ that was found to be 111 GPa.

5) Noteworthy that other authors have published different elastic coefficients on the basis of their calculations of elastic coefficients for WZ material (Wang, 2003).

$$C_{ij}^{wz} = \begin{pmatrix} 131 & 51 & 39 & 0 & 0 & 0 \\ 51 & 131 & 39 & 0 & 0 & 0 \\ 39 & 39 & 144 & 0 & 0 & 0 \\ 0 & 0 & 0 & 32 & 0 & 0 \\ 0 & 0 & 0 & 0 & 32 & 0 \\ 0 & 0 & 0 & 0 & 0 & 40 \end{pmatrix} \quad (4.4.11)$$

$$S_{ij}^{wz} = \begin{pmatrix} 0.0094 & -0.0031 & -0.0017 & 0 & 0 & 0 \\ -0.0031 & 0.0094 & -0.0017 & 0 & 0 & 0 \\ -0.0017 & -0.0017 & 0.0079 & 0 & 0 & 0 \\ 0 & 0 & 0 & 0.031 & 0 & 0 \\ 0 & 0 & 0 & 0 & 0.031 & 0 \\ 0 & 0 & 0 & 0 & 0 & 0.025 \end{pmatrix} \quad (4.4.12)$$

Therefore, the Young's modulus should be evaluated as

$$E_{mat}[0001] = 1/S_{33} = 1/0.0079 = 127 \text{ GPa.} \quad (4.4.13)$$

It is possible to conclude that numerical evaluation of the Young's modulus of WZ InP in direction [0001] has the value $\sim 120 \pm 10$ GPa. It is in good agreement with the experimental data for material in NWs, which was ~ 130 GPa.

Later we performed the numerical modeling of the mechanical properties of major III-V semiconductors [Publication SII]. Comparison of their Young's moduli indicates that strength GaP has the highest modulus ~ 167 GPa [Publication SII], which can have technological and economical inspiration on the designed and fabricated NW-based devices.

Establishment of a detailed method to evaluate the elastic modulus of material in tiny structure seems significant because certain materials can be grown in stable phase only in nanoscale structures, e.g. in the form of NWs. Therefore, it seems well-gathered that a nano-local method was developed and used for application where solely a nano-local method can be applied for the measurement. Data from AFM-based experiment seems more direct than deflected cloud in experiments with SEM/TEM oscillation based on the induced resonant vibration of NWs. Moreover, our AFM-based method is valid for tapered structures, since it is independent from resonant frequency, while this can cause

additional error for oscillating conical NWs. Few possible limiting factors of AFM-based experiment were described in our previous works and Sections of this thesis, e.g. contact resistance, bending force and speed of data recording in relation to charge trapping effects. Remarkably, if NWs would be strong enough for bending without breakage, then their deformation can be used as a source of electrical power via piezoelectric effect in WZ phase III-V structures as the next Section follows.

4.5 Analysis of piezo-phototronic effect with evaluation of inputs from direct piezoelectric effect coupled with photovoltaic effect

Analysis of experimental piezo-induced electrical current data based on methodology presented in Section 3.3 was presented in Publication VII and SII. Evaluation of inputs of piezo effect and photovoltaic effect was done for WZ GaAs NWs. The I-V curves of almost non-deformed NWs were measured followed by decreasing of the Z height resulting into observation of piezo-current. Further switching on of the laser increased the current due to the photoconductive effect. Photocurrent in the order of 50 pA was registered from the I-V curves (Figure 4.16).

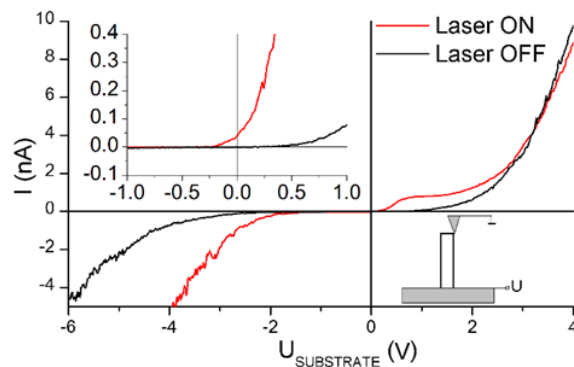


Figure 4.16 I-V curves of GaAs NWs standing vertically on a substrate, recorded during bending by a negligible deforming force with and without laser illumination. Right lower inset shows the experimental setup.

Since two phenomena took place simultaneously, it was logical to try to separate them in order to quantify their individual influence. The Figure 4.17a presents the graph with the experimentally measured electric current for different Z heights as two dotted lines as input of the piezo-induced current. At the same time, comparison of the red line and violet line represents the influence of the photocurrent when the laser became switched on. Further, it was possible to build up a 3D model of the NW in COMSOL package (COMSOL Inc., 2014) and calculate the piezo-potential for the compressed segments of the studied GaAs NWs. The results of this modeling are shown in Figure 4.17b. The

calculated values of potential are significantly lower (~three order of magnitude) than the data previously conveyed for ZnO and III-N NWs.

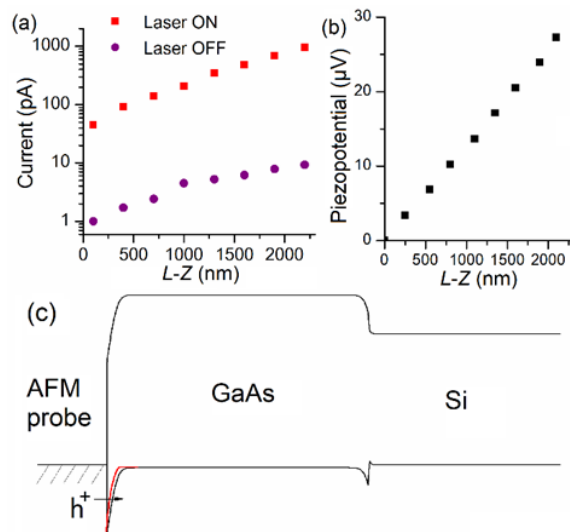


Figure 4.17 (a) Experimental current–distance dependencies presenting how short-circuit current arises during bending of a NW with decreasing of the tip–substrate distance Z both in the dark (blue) and under illumination (red). (b) Numerically calculated piezo-potential at the compressed end of the NW with increasing of bending. (c) Band diagram of a GaAs NW on a Si substrate without bending (black) and with bending (red).

Interestingly, the sign of the electric pulses was negative (Figure 3.18cd), while the similar negative pulses were reported for ZnO with the opposite type of doping. Thus, we explained the observed phenomena with consideration that the Schottky barrier height of GaAs is independent from the work function of the material comprising the AFM tip. We suppose that the local elevation of the valence band could emerge during the contact between the probe and the NW (scheme presented in Figure 4.17c). This elevation decreased the width of the potential barrier and resulted in intensified tunneling of the holes to the NW.

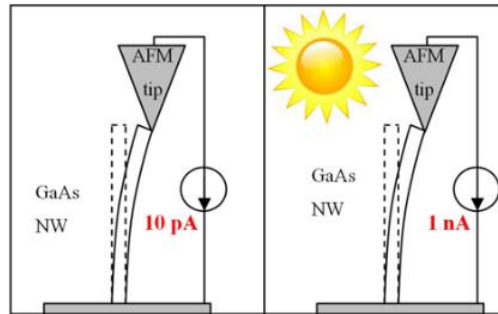


Figure 4.18 Concept of power generation in WZ GaAs NW on the basis of combined piezo-phototronic effect. Illumination increases the piezo-induced current from ~ 10 pA to 1 nA.

Therefore, piezo-phototronically generated current in WZ GaAs NWs was registered. Level of current appeared lower than reported from similar ZnO NWs, but still can be proposed for NW-based device applications where GaAs is involved. Since GaAs is desirable material for photovoltaics due to its bandgap, it is highly beneficial that piezo-phototronic effect was registered for GaAs. The technology of NW fabrication develops every year, so that regular nanostructures with controlled shapes and positions can be grown already on various substrates. In addition, WZ phase GaAs allows utilization of piezoelectric effect for generation of current (see Figure 4.18). Combining the material with its structure and adequate method of study it is possible to control the quality of GaAs NW-based piezo-phototronic devices by AFM.

5. Conclusions

Standard commercial AFM device was successfully used for investigation of mechanical, electrical and piezo properties of the as grown NWs without supportive SEM/AFM-coupled visualizing station. The developed measuring protocols and analysis of experimental and simulated results verifies relevance of the AFM-based method for versatile investigations of the NWs.

1) High locality of positioning of AFM probe was achieved after developing a simple methodology involving separate NWs on flat substrate and video-optical camera. This approach helps to allocate NWs with diameters as small as 10 nm.

2) PeakForce regime of AFM allowed direct contact measurements of thin NWs without breaking them and without the need in in-situ visualization of contact area. This method lead to successful recording of low-noise current-voltage characteristics of vertical GaAs NWs with diameters <80 nm.

3) AFM-based methods of current-voltage measurements for individual as-grown vertical zincblende GaAs NWs allowed understanding of specific influence of the major technological parameters. Impact of length of the NWs, NW diameters, SOG cover, doping level and type, additional illumination, sweeping rate of I-V curves and material/thickness of the surface passivation of NWs was revealed for the studied structures. The methodology of interpretation of the AFM-based results for I-V curves of NWs was developed.

4) Passivation type affects the height of the Schottky barrier between the semiconductor part of the NW and its metal cap. GaP passivation for GaAs NWs resulted in Ohmic contacts to the highly doped NWs. This was visible from the linear I-V curves. Analysis of I-V curves repeated the features of resistive behavior previously reported for lithography-fixed NWs. The recent AFM experiments have shown that such studies can be done for as-grown nanostructures without post-growth lithography step.

5) The AFM-based method to analyze the charge accumulation in vertical as-grown GaAs NWs was developed. The charge accumulated on the surface of GaAs NWs near the Schottky barrier lead to changes of the barrier height and resulted in emergence of hystereses of I-V curves. GaAs NWs with different doping were experimentally studied and compared with computer simulation. Major charge carriers were accumulated near the Schottky barrier in the native oxide. This increased the current for highly doped NWs and blocked the current flow for moderately doped NWs due to blocking of the conductive channel.

6) PeakForce regime of AFM was applied to perform repeatable bending of as-grown inclined InP NWs with cap diameters around 10 nm. The methodology developed for this AFM-based experiment involved HR-SEM only to recognize the diameters of the structures and without the need to use AFM/SEM coupled station.

- 7) The general analytical expression relating the flexibility profile of tapered NW and elastic modulus of the comprising material was deduced. This equation was applied to experimental flexibility profiles, which allowed to determine the Young's modulus of wurtzite InP in NWs.
- 8) The value of Young's modulus for the wurtzite phase InP in direction [1000] was 120 ± 10 GPa, similar to the value of Young's modulus of zincblende InP in direction [111]. Both of these values were verified with the help of the R.M.Martin's matrix transformation approach on the basis of tabulated experimental elastic constants for InP material. The R.M.Martin's method has shown similar value of Young's modulus in the range around 112 GPa - 127 GPa, depending on the elastic coefficients used for the model. The direction of the stress experienced by the InP NWs was verified by computer modeling in Silvaco software.
- 9) The mixed phase InP showed the Young's modulus ~40% lower than the pure wurtzite phase InP. This was in agreement with the results reported for InAs and ZnS NWs by other authors.
- 10) Generation of piezoelectric current in wurtzite GaAs NWs was registered with the help of conductive AFM in constant height mode. The electrical properties of NWs covered and not covered by nanothin AlGaAs passivation demonstrated beneficial role of the AlGaAs passivation realized in observable values of current generated by the NWs during their bending by AFM probe. Control of the laser illumination for the AFM-based experiment with WZ GaAs NWs was tested. Laser illumination raised the level of current by 2 orders of magnitude from 9 pA to 1 nA. The piezo-phototronic effect was registered for GaAs NWs for the first time.

6. Summary

The trajectory of experimental study research was changing with time because our group tried hard to perform accurate and non-trivial experiments on a station, which was not designed for that purpose. We tried to establish the new direction of versatile force controlled studies of electrical, advanced mechanical and electro-mechanical properties of standing NWs by AFM. The level of accomplished results is reported in this thesis.

Accurate and repeatable measurements of I-V curves, mechanical bending profiles and registration of piezoelectric current was demonstrated for semiconductor NWs. This was achieved with the help of modern *PeakForce* measuring mode of AFM, without breakage of the NWs during the scanning. Additional optical microscope and/or SEM were used only as supportive stations, but without the need in laborious and expensive SEM/AFM coupled device. The protocols for all these measurements were developed for standard commercial AFM and were presented in this thesis. Present work has proven that AFM is an adequate and extremely useful device to study NWs. We consider that common presumption about inapplicability of AFM for studies of NWs has been refuted based on the experimentally obtained results. Furthermore, it seems possible to broaden the application of the abovementioned procedures for studies of other 1D and low-dimensional structures listed previously in Section 2.2.

It is possible to *highlight* few major findings related with the studied materials.

- Surface passivation material and the layer thickness have big influence on electrical conductivity of NWs, which was examined by direct AFM-NW contact for single as-grown nanostructures. It is possible to recommend AlGaAs passivation due to low lattice mismatch with GaAs. In addition, GaP shell passivation was proven to lead to Ohmic resistivity of the GaAs NWs.
- Bending of inclined NWs brings the opportunities to measure materials' properties in many low-dimensional objects. It can be proposed that specific structures can be fabricated in order to establish the metrological standard for AFM-based experiment. Routine measurements for the samples with equal shapes would simplify the experimental process and easily reveal the modulus of the constituting materials.
- Piezoelectric current generated in GaAs NWs represents a pathway to combine (i) the material appropriate for photovoltaic application with (ii) AlGaAs passivation reducing the surface state density for development of optoelectronic applications with (iii) wurtzite crystal structure for utilization of piezo effect with (iv) regular small structures grown by fast and repeatable nanofabrication method. This can bring new opportunities for assembly of piezo-phototronic nano-generators, for example, useful in wearable devices or mobile electronics. Consideration of frequency of NW oscillation and timing of charge transport indicates inapplicability of generation of current based on frequencies caused by natural wind or acoustic noise generated by talking. However, specific waste sounds and other ambient vibrations can enhance the piezo-potential formed at the side surfaces of the NWs.

Simple optical microscope allowed finding of the desirable nanometer-scale objects in the exterior of larger “markers”. This procedure of locating a single individual 20 nm wide NW on a substrate from comparison of optical and SEM pictures resembled an intriguing *Find Wally game* that was successfully won. It is possible to conclude that the developed AFM-based methodology, in general, is one of the main results of this work. Methodical part of this thesis was written in details so that other research groups have opportunity to justify our methods and verify the results. Should be mentioned as a technical point here that no calibration of the piezoscanner was carried out except annual maintenance calibration. According to the calibration updates, the scanner's calibration was not significantly worsened, although the available area of scanning decreased from $\sim 175 \mu\text{m}$ to $\sim 160 \mu\text{m}$ after 4 years. This means that AFM is a low-maintenance device, which is very beneficial for studies of nanostructures including NWs. Utilization of various AFM devices can appear very prolific in the light of additional modules available from various manufacturers. For example, Bruker device was considered user-friendly and provided the control of delicate force, while NT-MDT device seemed more customized for laborious research, e.g. allowed control of the illuminating laser.

Apart from methodological developments, material properties for III-V semiconductors were examined. Most part of the discussed results are in the qualitative plane, except quantitative results on elastic modulus of WZ InP directly measured to be $120 \pm 10 \text{ GPa}$ in direction [0001].

A new *AFM center* has been established in Lappeenranta University of Technology during the timeframe of this research. It appeared possible to further develop the instrument by creation of new custom-built setups, e.g. gas cell with control of environmental humidity, which can be a direction of forthcoming research with AFM and NWs. The major philosophy of our approach is in using of available equipment rather than instruments that can be considered ideal for research.

The NW-oriented protocols developed in this work were included in University course of Nanophysics lectured for Technical physics students. Working with AFM helps students to recognize the scaling. Moreover, nano-manipulation of NWs by AFM probe provides a vivid analogy with a skillful human arm. Describing the novel experimental research approaches seems worthy as part of *insightful teaching of science and technology*.

Few enhancements can be proposed to develop the results in the completed papers.

- Paper I. One of the possible improvements realized after the work with the first series of samples was that it could be optimal to distinguish between the NW height and existence of passivation layer, which have interplay in the series.
- Paper II. Possible improvements could be in universalization of heights and passivations, studying the sulfur layers and to testify the liquid-phase mechanism. Moreover, passivation shell 300 nm was poorly controlled. It can be good to testify other thicknesses of passivation layers for all possible compounds.
- Papers III and IV. Possible improvements could be in optimization of taper/conical shape, length of NWs, examination of material in significantly

thicker NWs and much thinner NWs. However, fabrication of stable WZ-phase NWs can require significant developments in fabrication stage.

- Paper V. Additional attention to piezo-response measurements can be supported by results of numerical simulations. In addition to the stated properties, magnetic properties, which are partly related with electro-mechanical parameters could be clarified for NWs. Further efforts can be dedicated to studies of pyro- and thermoelectric effects in NWs by AFM-based methods developed in this thesis.
- Paper VI. Possible improvements could be in recognizing the influence of vacuum toward electrical properties observed by KPFM and from I-V curves.
- Paper VII. Additional control of bending force and trying the NWs with other diameters and lengths can be proposed. Influence of vacuum to the observed current can be studied. It was not accessed, if it is possible to visualize the increase of current during a faster bending of the NW, while rate of bending can have impact toward the current.

One of the possible *outlooks* can be (1) instrumental, so that impedance spectroscopy can be combined with the C-AFM via AFM controller module. If the spectroscopy device would be involved, then the external signal will be generated and analyzed. This might reveal additional details of transport phenomena for NWs. (2) It also seems adequate to further *develop the simulation* part of the NWs with different shapes, compositions and crystal structures. The work SI in Supplementary material displays an intention to develop the general model of III-V semiconductors elasticity. General model is based on AFM-based experimental data for rather rare phases of WZ crystals, e.g. GaP, GaAs, InP etc. (3) As a further development of mechanical experiment, we proposed the double-apex tips shown in the end of Section 3.2. (4) It can be beneficial to apply the difficult Timoshenko beam theory to compare it with results of Euler-Bernoulli beam theory in order to validate the latter one for the studied NWs. (5) Various fixations (one-point, two-point, lying on substrate, with one unfixed contact and with two unfixed contacts) can be tested for the purposes of validation of the one-point model, which is of course good for as-grown structures.

The major challenges still complicating the electrical AFM-based experiments are related with wearing of the conductive coating from the C-AFM tips and struggle to suggest any relevant calibrated conductive probe with identified shape and resistance. It was not possible to choose the most optimal probe for C- AFM experiment, while we would propose the full metal, e.g. platinum, probes for regular electrical studies. It can also be very interesting to compare the NW parameters obtained on AFM with data obtained on modern SEM-based setups. Must be mentioned though that the AFM experiments could be restricted by necessity in development of technological nanofabrication, both in preparation of high quality AFM probes and perfect NW arrays.

New modes of AFM are built annually. Therefore, the AFM-based opportunities for studies of NWs and other structures are continuously developing. They might support the recent developments in NWs technology for real and forthcoming biomimetic, medical and neuro-brain activity proposes, which suggest a vision of NWs as building blocks for technologies of the underway XXI century.

References

- Alekseev, P. A., Dunaevskii, M. S., Stovpyaga, A. V. *et al.* (2012) Measurement of Young's modulus of GaAs nanowires growing obliquely on a substrate, *Semiconductors*, 46(5), pp. 641–646.
- Alekseev, P. A. (2013) *Investigation of charge and electric field distribution in nanostructures by Scanning Probe Microscopy (in Russian)*. PhD thesis. SPbGTU LETI (Russia).
- Alvarez, J., Ngo, I., Gueunier-Farret, M.-E. *et al.* (2011) Conductive-probe Atomic Force Microscopy characterization of silicon nanowire, *Nanoscale Research Letters*, 6(1), p. 110.
- Banerjee, S., Muehle, U., Löffler, M. *et al.* (2015) Preparation and characterization of silicon nanowires using SEM/FIB and TEM, *International Journal of Materials Research*, 106(7), pp. 697–702.
- Barth, S., Harnagea, C., Mathur, S. *et al.* (2009) The elastic moduli of oriented tin oxide nanowires, *Nanotechnology*, 20(11), p. 115705.
- Beinik, I. (2011) *Electrical characterization of semiconductor nanostructures by conductive probe based Atomic Force Microscopy techniques*. PhD thesis. Montanuniversität Leoben (Austria).
- Bernardes-Filho, R. and Assis, O. B. G. de (2005) Development of an algorithm for tip-related artifacts identification in AFM biological film imaging, *Brazilian Archives of Biology and Technology*, 48(4), pp. 667–674.
- Bespalova, K. (2018) *Experimental measurement of Young's modulus of gallium phosphide nanowires by Atomic Force Microscopy*. MSc thesis. Lappeenranta University of Technology (Finland).
- Binnig, G., Rohrer, H., Gerber, C. *et al.* (1982) Surface studies by Scanning Tunneling Microscopy, *Physical Review Letters*, 49(1), pp. 57–61.
- Binnig, G., Quate, C. F. and Gerber, C. (1986) Atomic Force Microscope, *Physical Review Letters*, 56(9), pp. 930–933.
- Björk, M. T., Ohlsson, B. J., Sass, T. *et al.* (2002) One-dimensional steeplechase for electrons realized, *Nano Letters*, 2(2), pp. 87–89.
- Bolinsson, J. (2010) *The crystal structure of III-V semiconductor nanowires: Growth and characterization*. PhD thesis. Lund University (Sweden).
- BRUKER Inc. (2018) *SCANASYST-AIR AFM probes product description*.
- Calahorra, Y., Shtempluck, O., Kotchetkov, V. *et al.* (2015) Young's modulus, residual stress, and crystal orientation of doubly clamped silicon nanowire beams, *Nano Letters*, 15(5), pp. 2945–2950.

- Calahorra, Y., Guan, X., Halder, N. N. *et al.* (2017) Exploring piezoelectric properties of III–V nanowires using piezo-response force microscopy, *Semiconductor Science and Technology*, 32(7), p. 074006.
- Calarco, R., Marso, M., Richter, T. *et al.* (2005) Size-dependent photoconductivity in MBE-grown GaN–nanowires, *Nano Letters*, 5(5), pp. 981–984.
- Chen, C. Q., Shi, Y., Zhang, Y. S. *et al.* (2006) Size dependence of Young’s modulus in ZnO nanowires, *Physical Review Letters*, 96(7), p. 075505.
- Chen, L., Lu, W. and Lieber, C. M. (2015) *Semiconductor nanowire growth and integration*. 1st ed, in Lu, W. and Xiang, J. (eds.) *Semiconductor Nanowires: From Next-Generation Electronics to Sustainable Energy*. 1st ed. London, UK: Royal Society of Chemistry, pp. 1–53.
- Chen, Y., An, X. and Liao, X. (2017) Mechanical behaviors of nanowires, *Applied Physics Reviews*, 4(3), p. 031104.
- Chia, A. C. E., Tirado, M., Thouin, F. *et al.* (2013) Surface depletion and electrical transport model of AlInP-passivated GaAs nanowires, *Semiconductor Science and Technology*, 28(10), p. 105026.
- Chia, A. C. E. (2015) *Electrical characterization and optimization of GaAs nanowire ensemble devices*. PhD thesis. McMaster University (Canada).
- COMSOL Inc. (2014) *COMSOL Multiphysics User’s Guide, version 5.0*. Stockholm, Sweden: COMSOL Inc.
- Dagyte, V. (2018) *Growth and optical properties of III-V semiconductor nanowires, studies relevant for solar cells*. PhD thesis. Lund University (Sweden).
- van Dam, D., van Hoof, N. J. J., Cui, Y. *et al.* (2016) High-efficiency nanowire solar cells with omnidirectionally enhanced absorption due to self-aligned Indium–Tin–Oxide Mie scatterers, *ACS Nano*, 10(12), pp. 11414–11419.
- Dunaevskiy, M., Dementyev, P., Egorov, V. *et al.* (2009) Measurements of current–voltage characteristics of separate single GaAs nanowhiskers, *Physica Status Solidi (c)*, 6(12), pp. 2701–2703.
- Ellis, J. A. and Barnes, P. A. (2000) Current–voltage characteristics of a GaAs Schottky diode accounting for leakage paths, *Applied Physics Letters*, 76(1), pp. 124–125.
- Erofeev, V. I., Kazhaev, V. V., Lisenkova, E. E. *et al.* (2011) Dynamic behavior of the beams of Bernoulli-Euler, Rayleigh, and Timoshenko models lying on an elastic foundation (In Russian), *Bulletin of the Nizhny Novgorod University of N.I. Lobachevsky*. Russia, 5(3), pp. 274–278.
- Filippov, S. (2016) *Micro-photoluminescence and micro-Raman spectroscopy of novel semiconductor nanostructures*. PhD thesis. Linköping University (Sweden).

-
- Gere, J. M. and Goodno, B. J. (2012) *Mechanics of Materials*. 8th ed. SI. Boston, USA: Cengage Learning Global Engineering.
- Giessibl, F. J. (2000) *Progress in Atomic Force Microscopy*. PhD thesis. Augsburg University (Germany).
- Gulla, S. (2013) *Advanced micro photoluminescence spectroscopy of single GaAs/AlGaAs core-shell nanowires*. MSc thesis. NTNU-Trondheim (Norway).
- Guo, D., Xie, G. and Luo, J. (2014) Mechanical properties of nanoparticles: Basics and applications, *Journal of Physics D: Applied Physics*, 47(1), p. 013001.
- Haggrén, T. (2016) *Nanowire technology for optoelectronic applications*. PhD thesis. Aalto University (Finland).
- Halpern, E., Elias, G., Kretinin, A. V. *et al.* (2012) Direct measurement of surface states density and energy distribution in individual InAs nanowires, *Applied Physics Letters*, 100(26), p. 262105.
- Halpern, E., Henning, A., Shtrikman, H. *et al.* (2015) Room temperature observation of quantum confinement in single InAs nanowires, *Nano Letters*, 15(1), pp. 481–485.
- Huang, M. H., Mao, S., Feick, H. *et al.* (2001) Room-temperature ultraviolet nanowire nanolasers, *Science*, 292(5523), pp. 1897–1899.
- Jacobsson, D. (2015) *Crystal structures in GaAs nanowires: Growth and characterization*. PhD thesis. Lund University (Sweden).
- Kaemmer, S. B. (2011) *Application Note #133 Introduction to Bruker's ScanAsyst and PeakForce Tapping AFM Technology*. BRUKER Inc.
- Kakko, J.-P. (2017) *Fabrication of semiconductor nanowires for optical studies*. PhD thesis. Aalto University (Finland).
- Karlsson, L. S. (2007) *Transmission Electron Microscopy of III-V Nanowires and Nanotrees*. PhD thesis. Lund University (Sweden).
- Krogstrup, P., Jørgensen, H. I., Heiss, M. *et al.* (2013) Single-nanowire solar cells beyond the Shockley–Queisser limit, *Nature Photonics*, 7(4), pp. 306–310.
- Labuschagne, A., van Rensburg, N. F. J. and van der Merwe, A. J. (2009) Comparison of linear beam theories, *Mathematical and Computer Modelling*. Elsevier Ltd, 49(1–2), pp. 20–30.
- Lähnemann, J. (2013) *Luminescence of group-III-V nanowires containing heterostructures. The role of polytypism, polarization fields and carrier localization*. Humboldt-Universität zu Berlin.
- Leahu, G., Petronijevic, E., Belardini, A. *et al.* (2017) Photo-acoustic spectroscopy revealing resonant absorption of self-assembled GaAs-based nanowires, *Scientific Reports*, 7(1), p. 2833.

- Lexholm, M., Karlsson, I., Boxberg, F. *et al.* (2009) Optical determination of Young's modulus of InAs nanowires, *Applied Physics Letters*, 95(11), p. 113103.
- Li, C., Minne, S., Pittenger, B. *et al.* (2011) *Application Note #132 Simultaneous Electrical and Mechanical Property Mapping at the Nanoscale with PeakForce TUNA*. BRUKER Inc.
- Lieber, C. M. (1998) One-dimensional nanostructures: Chemistry, physics & applications, *Solid State Communications*, 107(11), pp. 607–616.
- Lin, X., He, X., Lu, J. *et al.* (2006) Manipulation and four-probe analysis of nanowires in UHV by application of four tunneling microscope tips: A new method for the investigation of electrical transport through nanowires, *Surface and Interface Analysis*, 38(6), pp. 1096–1102.
- Lord, A. M., Walton, A. S., Maffei, T. G. *et al.* (2014) ZnO nanowires with Au contacts characterised in the as-grown real device configuration using a local multi-probe method, *Nanotechnology*, 25(42), p. 425706.
- Lord, A. M., Maffei, T. G., Kryuchenkova, O. *et al.* (2015) Controlling the electrical transport properties of nanocontacts to nanowires, *Nano Letters*, 15(7), pp. 4248–4254.
- Lu, M.-P., Song, J., Lu, M.-Y. *et al.* (2009) Piezoelectric nanogenerator using p-type ZnO nanowire arrays, *Nano Letters*, 9(3), pp. 1223–1227.
- Lubk, A., Wolf, D., Prete, P. *et al.* (2014) Nanometer-scale tomographic reconstruction of three-dimensional electrostatic potentials in GaAs/AlGaAs core-shell nanowires, *Physical Review B*, 90(12), p. 125404.
- Lysak, V., Soshnikov, I. P., Lahderanta, E. *et al.* (2016) Piezoelectric effect in GaAs nanowires: experiment and theory, *Physica Status Solidi (RRL) - Rapid Research Letters*, 10(2), pp. 172–175.
- Martin, R. M. (1972) Relation between elastic tensors of Wurtzite and Zinc-Blende structure materials, *Physical Review B*, 6(12), pp. 4546–4553.
- Mironov, V. L. (2004) *Fundamentals of Scanning Probe Microscopy*. 1st ed. Nizhniy Novgorod, Russia: NT-MDT.
- Moon, J., Cho, M. and Zhou, M. (2015) Size- and structure-dependence of thermal and mechanical behaviors of single-crystalline and polytypic superlattice ZnS nanowires, *Journal of Applied Physics*, 117(21), p. 214307.
- Morales, A. M. and Lieber, C. M. (1998) A laser ablation method for the synthesis of crystalline semiconductor nanowires, *Science*, 279(5348), pp. 208–211.
- Nye, J. F. (1957) *The matrix method*. 1st ed, in *Physical Properties of Crystals. Their Representation by Tensors and Matrices*. 1st ed. Oxford, UK: Clarendon Press, pp. 150–169.

- Pittenger, B., Erina, N. and Su, C. (2012) *Application Note #128 Quantitative Mechanical Property Mapping at the Nanoscale with PeakForce QNM*. BRUKER Inc.
- Rigutti, L. and Tchernycheva, M. (2013) *Electrical and electro-optical characterization of semiconductor nanowires*. 2nd ed, in Lamberti, C. and Agostini, G. (eds.) *Characterization of Semiconductor Heterostructures and Nanostructures*. 2nd ed. Elsevier, pp. 641–684.
- Röhlig, C.-C., Niebelschütz, M., Brueckner, K. *et al.* (2010) Elastic properties of nanowires, *Physica Status Solidi (b)*, 247(10), pp. 2557–2570.
- Rojo, M. M., Calero, O. C., Lopeandia, A. F. *et al.* (2013) Review on measurement techniques of transport properties of nanowires, *Nanoscale*, 5(23), p. 11526.
- Sader, J. E., Chon, J. W. M. and Mulvaney, P. (1999) Calibration of rectangular Atomic Force Microscope cantilevers, *Review of Scientific Instruments*, 70(10), pp. 3967–3969.
- Sahin, O. (2005) *Harmonic Force Microscope: A new tool for biomolecular identification and material characterization based on nanomechanical measurements*. PhD thesis. Stanford University (USA).
- Shahid, N. (2015) *Technology and properties of InP-based photonic crystal structures and devices*. PhD thesis. KTH Royal Institute of Technology (Sweden).
- SILVACO Inc. (2015) *ATLAS User's Manual*. Santa Clara, USA: Silvaco Inc.
- Stan, G., Ciobanu, C. V., Parthangal, P. M. *et al.* (2007) Diameter-dependent radial and tangential elastic moduli of ZnO nanowires, *Nano Letters*, 7(12), pp. 3691–3697.
- Stan, G., Krylyuk, S., Davydov, A. V. *et al.* (2012) Ultimate bending strength of Si nanowires, *Nano Letters*, 12(5), pp. 2599–2604.
- Sze, S. M. (1981) *Physics of Semiconductor Devices*. 2nd ed. New York, USA: John Wiley & Sons, Ltd.
- Talin, A. A., Léonard, F., Katzenmeyer, A. M. *et al.* (2010) Transport characterization in nanowires using an electrical nanoprobe, *Semiconductor Science and Technology*, 25(2), p. 024015.
- Timm, R., Persson, O., Engberg, D. L. J. *et al.* (2013) Current–Voltage characterization of individual as-grown nanowires using a Scanning Tunneling Microscope, *Nano Letters*, 13(11), pp. 5182–5189.
- Wagner, R. S. and Ellis, W. C. (1964) Vapor-liquid-solid mechanism of single crystal growth, *Applied Physics Letters*, 4(5), pp. 89–90.
- Wallentin, J., Anttu, N., Asoli, D. *et al.* (2013) InP nanowire array solar cells achieving 13.8% efficiency by exceeding the ray optics limit, *Science*, 339(6123), pp. 1057–1060.
- Wang, S. Q. and Ye, H. Q. (2003) First-principles study on elastic properties and phase stability of III–V compounds, *Physica Status Solidi (b)*, 240(1), pp. 45–54.

- Wang, S., Shan, Z. and Huang, H. (2017) The mechanical properties of nanowires, *Advanced Science*, 4(4), p. 1600332.
- Wang, Z. L., Gao, R. P., Pan, Z. W. *et al.* (2001) Nano-scale mechanics of nanotubes, nanowires, and nanobelts, *Advanced Engineering Materials*, 3(9), p. 657.
- Wang, Z. L. and Song, J. (2006) Piezoelectric nanogenerators based on zinc oxide nanowire arrays, *Science*, 312(5771), pp. 242–246.
- Werner, F., Limbach, F., Carsten, M. *et al.* (2009) Electrical conductivity of InN nanowires and the influence of the native indium oxide formed at their surface, *Nano Letters*, 9(4), pp. 1567–1571.
- Wong, E. W., Sheehan, P. E. and Lieber, C. M. (1997) Nanobeam mechanics: Elasticity, strength, and toughness of nanorods and nanotubes, *Science*, 277(5334), pp. 1971–1975.
- Xia, Y., Yang, P., Sun, Y. *et al.* (2003) One-dimensional nanostructures: Synthesis, characterization, and applications, *Advanced Materials*, 15(5), pp. 353–389.
- Xu, F., Qin, Q., Mishra, A. *et al.* (2010) Mechanical properties of ZnO nanowires under different loading modes, *Nano Research*, 3(4), pp. 271–280.
- Xu, T. and Grandidier, B. (2015) *Electrical characterization of semiconductor nanowires by Scanning-Probe Microscopy*. 1st ed, in Arbiol, J. and Xiong, Q. (eds.) *Semiconductor Nanowires. Materials, Synthesis, Characterization and Applications*. 1st ed. Elsevier, pp. 277–304.
- Xu, W., Chin, A., Ye, L. *et al.* (2012) Charge transport and trap characterization in individual GaSb nanowires, *Journal of Applied Physics*, 111(10), p. 104515.
- Yazawa, M., Koguchi, M., Muto, A. *et al.* (1992) Effect of one monolayer of surface gold atoms on the epitaxial growth of InAs nanowhiskers, *Applied Physics Letters*, 61(17), pp. 2051–2053.
- Yu, L., Rigutti, L., Tchernycheva, M. *et al.* (2013) Assessing individual radial junction solar cells over millions on VLS-grown silicon nanowires, *Nanotechnology*, 24(27), p. 275401.
- Zhai, T. and Yao, J. (2013) *One-Dimensional Nanostructures: Principles and Applications*. 1st ed. Edited by T. Zhai and J. Yao. Hoboken, NJ, USA: John Wiley & Sons, Inc.
- Zhang, Z., Yao, K., Liu, Y. *et al.* (2007) Quantitative analysis of Current–Voltage characteristics of semiconducting nanowires: Decoupling of contact effects, *Advanced Functional Materials*, 17(14), pp. 2478–2489.
- Zhou, Y. S., Wang, K., Han, W. *et al.* (2012) Vertically aligned CdSe nanowire arrays for energy harvesting and piezotronic devices, *ACS Nano*, 6(7), pp. 6478–6482.

Publication I

Geydt, P., Alekseev, P.A., Dunaevskiy, M.S., Lähderanta, E., Haggrén, T.,
Kakko, J.-P., and Lipsanen, H.

**Observation of linear I-V curves on vertical GaAs nanowires with
Atomic Force Microscope**

Reprinted with permission from

Journal of Physics: Conference Series

Vol. 661(1), pp. 012031-1-6, 2015

© 2015, IOP Publishing Ltd

Publication II

Geydt, P., Alekseev, P.A., Dunaevskiy, M.S., Haggrén, T., Kakko, J.-P., Lähderanta, E., and Lipsanen, H.

Influence of surface passivation on electric properties of individual GaAs nanowires studied by current–voltage AFM measurements

Reprinted with permission from

Lithuanian Journal of Physics

Vol. 56(2), pp. 92-101, 2016

© 2016, Lietuvos mokslu akademija

Publication III

Geydt, P., Dunaevskiy, M., Alekseev, P., Kakko, J.-P., Haggrén, T., Lähderanta, E., and Lipsanen, H.

**Direct measurement of elastic modulus of InP nanowires with Scanning Probe
Microscopy in PeakForce QNM mode**

Reprinted with permission from

Journal of Physics: Conference Series

Vol. 769(1), pp. 012029-1-8, 2016

© 2016, IOP Publishing Ltd

Publication IV

Dunaevskiy, M., Geydt, P., Lähderanta, E., Alekseev, P., Haggrén, T., Kakko, J.-P.,
Jiang, H., and Lipsanen, H.

Young's modulus of wurtzite and zinc blende InP nanowires

Reprinted with permission from

Nano Letters

Vol. 17(6), pp. 3441-3446, 2017

© 2017, American Chemical Society

Publication V

Geydt, P., Dunaevskiy, M.S., and Lähderanta, E.

Opportunities of Scanning Probe Microscopy for electrical, mechanical and electromechanical research of semiconductor nanowires

Reprinted with permission from

Nanowires - New Insights

Book chapter 8, pp. 155-188. ISBN 978-953-51-3284-4, 2017

© 2017, IntechOpen

Publication VI

Alekseev, P.A., Geydt, P., Dunaevskiy, M.S., Lähderanta, E., Haggrén, T., Kakko, J.-P., and Lipsanen, H.

I-V curve hysteresis induced by gate-free charging of GaAs nanowires' surface oxide

Reprinted with permission from

Applied Physics Letters

Vol. 111(13), pp. 132104-1-6, 2017

© 2017, AIP Publishing

Publication VII

Alekseev, P.A., Sharov, V.A., Geydt, P., Dunaevskiy, M.S., Lysak, V.V., Cirlin, G.E.,
Reznik, R.R., Khrebtov, A.I., Soshnikov, I.P., and Lähderanta, E.
Piezoelectric current generation in wurtzite GaAs nanowires

Reprinted with permission from

Physica Status Solidi - Rapid Research Letters

Vol. 12(1), pp. 1700358-1-5, 2018

© 2018, WILEY-VCH Verlag GmbH & Co.

ACTA UNIVERSITATIS LAPPEENRANTAENSIS

794. BANAEIANJAHROMI, NEGIN. On the role of enterprise architecture in enterprise integration. 2018. Diss.
795. HASHEELA-MUFETI, VICTORIA TULIVAYE. Empirical studies on the adoption and implementation of ERP in SMEs in developing countries. 2018. Diss.
796. JANHUNEN, SARI. Determinants of the local acceptability of wind power in Finland. 2018. Diss.
797. TEPLOV, ROMAN. A holistic approach to measuring open innovation: contribution to theory development. 2018. Diss.
798. ALBATS, EKATERINA. Facilitating university-industry collaboration with a multi-level stakeholder perspective. 2018. Diss.
799. TURA, NINA. Value creation for sustainability-oriented innovations: challenges and supporting methods. 2018. Diss.
800. TALIKKA, MARJA. Recognizing required changes to higher education engineering programs' information literacy education as a consequence of research problems becoming more complex. 2018. Diss.
801. MATTSSON, ALEKSI. Design of customer-end converter systems for low voltage DC distribution from a life cycle cost perspective. 2018. Diss.
802. JÄRVI, HENNA. Customer engagement, a friend or a foe? Investigating the relationship between customer engagement and value co-destruction. 2018. Diss.
803. DABROWSKA, JUSTYNA. Organizing for open innovation: adding the human element. 2018. Diss.
804. TIAINEN, JONNA. Losses in low-Reynolds-number centrifugal compressors. 2018. Diss.
805. GYASI, EMMANUEL AFRANE. On adaptive intelligent welding: Technique feasibility in weld quality assurance for advanced steels. 2018. Diss.
806. PROSKURINA, SVETLANA. International trade in biomass for energy production: The local and global context. 2018. Diss.
807. DABIRI, MOHAMMAD. The low-cycle fatigue of S960 MC direct-quenched high-strength steel. 2018. Diss.
808. KOSKELA, VIRPI. Tapping experiences of presence to connect people and organizational creativity. 2018. Diss.
809. HERALA, ANTTI. Benefits from Open Data: barriers to supply and demand of Open Data in private organizations. 2018. Diss.
810. KÄYHKÖ, JORMA. Erityisen tuen toimintaprosessien nykytila ja kehittäminen suomalaisessa oppisopimuskoulutuksessa. 2018. Diss.
811. HAJIKHANI, ARASH. Understanding and leveraging the social network services in innovation ecosystems. 2018. Diss.
812. SKRIKO, TUOMAS. Dependence of manufacturing parameters on the performance quality of welded joints made of direct quenched ultra-high-strength steel. 2018. Diss.

813. KARTTUNEN, ELINA. Management of technological resource dependencies in interorganizational networks. 2018. Diss.
814. CHILD, MICHAEL. Transition towards long-term sustainability of the Finnish energy system. 2018. Diss.
815. NUTAKOR, CHARLES. An experimental and theoretical investigation of power losses in planetary gearboxes. 2018. Diss.
816. KONSTI-LAAKSO, SUVI. Co-creation, brokering and innovation networks: A model for innovating with users. 2018. Diss.
817. HURSKAINEN, VESA-VILLE. Dynamic analysis of flexible multibody systems using finite elements based on the absolute nodal coordinate formulation. 2018. Diss.
818. VASILYEV, FEDOR. Model-based design and optimisation of hydrometallurgical liquid-liquid extraction processes. 2018. Diss.
819. DEMESA, ABAYNEH. Towards sustainable production of value-added chemicals and materials from lignocellulosic biomass: carboxylic acids and cellulose nanocrystals. 2018. Diss.
820. SIKANEN, EERIK. Dynamic analysis of rotating systems including contact and thermal-induced effects. 2018. Diss.
821. LIND, LOTTA. Identifying working capital models in value chains: Towards a generic framework. 2018. Diss.
822. IMMONEN, KIRSI. Ligno-cellulose fibre poly(lactic acid) interfaces in biocomposites. 2018. Diss.
823. YLÄ-KUJALA, ANTTI. Inter-organizational mediums: current state and underlying potential. 2018. Diss.
824. ZAFARI, SAHAR. Segmentation of partially overlapping convex objects in silhouette images. 2018. Diss.
825. MÄLKKI, HELENA. Identifying needs and ways to integrate sustainability into energy degree programmes. 2018. Diss.
826. JUNTUNEN, RAIMO. LCL filter designs for parallel-connected grid inverters. 2018. Diss.
827. RANAEI, SAMIRA. Quantitative approaches for detecting emerging technologies. 2018. Diss.
828. METSO, LASSE. Information-based industrial maintenance - an ecosystem perspective. 2018. Diss.
829. SAREN, ANDREY. Twin boundary dynamics in magnetic shape memory alloy Ni-Mn-Ga five-layered modulated martensite. 2018. Diss.
830. BELONOGOVA, NADEZDA. Active residential customer in a flexible energy system - a methodology to determine the customer behaviour in a multi-objective environment. 2018. Diss.
831. KALLIOLA, SIMO. Modified chitosan nanoparticles at liquid-liquid interface for applications in oil-spill treatment. 2018. Diss.

Acta Universitatis
Lappeenrantaensis
832



ISBN 978-952-335-310-7
ISBN 978-952-335-311-4 (PDF)
ISSN-L 1456-4491
ISSN 1456-4491
Lappeenranta 2018
